Master's Thesis

Solution-processed stretchable Ag_2S semiconductor thin films for wearable self-powered nonvolatile memory

Soyoung Cho

Department of Materials Science and Engineering

Ulsan National Institute of Science and Technology

2021

Solution-processed stretchable Ag_2S semiconductor thin films for wearable self-powered nonvolatile memory

Soyoung Cho

Department of Materials Science and Engineering

Ulsan National Institute of Science and Technology

Solution-processed stretchable Ag_2S semiconductor thin films for wearable self-powered nonvolatile memory

A thesis submitted to
Ulsan National Institute of Science and Technology
in partial fulfillment of the
requirements for the degree of
Master of Science

Soyoung Cho

06.18.2021 of submission
Approved by

_____
Advisor

Prof. Jae Sung Son

Solution-processed stretchable Ag_2S semiconductor thin films for wearable self-powered nonvolatile memory

Soyoung Cho

This certifies that the thesis of Soyoung Cho is approved.

06.18.2021 of submission

Signature

_____

Advisor: Prof. Jae Sung Son

Signature

_____

Prof. Moon Kee Choi

Signature

_____

Prof. Ju-Young Kim

Abstract

Stretchable thin films have facilitated the developments in the field of flexible and stretchable electronics such as deformable sensors, displays, memories and energy devices which have received significant attention due to their potential use in smart wearable devices. Potential candidates for stretchable materials include polymer-based elastomers and their composites with functional fillers but they intrinsically suffer from low electrical properties. Compared to large plastic deformations observed in elastomeric organic materials, inorganic semiconductors have low plasticity (< 0.2%) due to their unique bonding properties which restrict applications in stretchable electronics. α-Ag2S bulk crystals, a member of the metal chalcogenide, is considered as a promising candidate to produce deformable semiconductor layers in flexible and stretchable electronics due to its outstanding mechanical and electrical properties. An extremely low slippage energy and high cleavage energy between the crystal planes of α-Ag2S bulk crystals exhibit both semiconducting behavior and ductility similar to metals. Such unusual characteristics have abundant potential for energy and electronic applications. Although several studies reported the use of Ag_2S bulk ingots in energy devices, the fabrication of Ag_2S thin films based stretchable electronics have never been realized due to highly complicated synthetic procedures. Typical procedures for producing α-Ag_2S crystals require energy intensive process, such as SPS sintering method and complicated deposition equipment set-up, limiting both the available substrates and processing temperatures for the fabrication of flexible and stretchable electronics.

The solution process of metal chalcogenides thin films has been of great interest since it provides the ability to fabricate high quality and scalable thin films in a low-cost manner. Recent discoveries of alkahest solvent, a mixture of amine and thiol solutions allowed soluble inorganic to be utilized as ink processing for thin films. Furthermore, the metal chalcogenide inks can achieve highly crystalline and uniform thin films using a simple solution process and a subsequent heat treatment.

I herein report solution-process synthesis of ductile α-Ag_2S thin films and the manufacturing process of all inorganic, self-powered and stretchable memory devices. The molecular Ag_2S complex solution was synthesized by chemical reduction of bulk Ag_2S powder to produce a wafer-scale, highly crystalline Ag_2S thin film. Thin films exhibit elasticity through inherent ductility and maintain structural integrity with 14.9 % tensile strain. In addition, Ag_2S-based resistive memory manufactured has excellent bipolar switching characteristics (I_{on}/I_{off} ratio of ~10^5, operational endurance of 100 cycles, and retention time > 10^6 s) and excellent mechanical elasticity (no degradation to elasticity). On the other hand, the device is very durable in a variety of chemical environments and temperatures between -196 and 300 °C, especially at 85% relative humidity and 85 °C for 168 hours. Finally, I demonstrate self-powered memory device combined with motion sensors for a wearable health monitoring system, which potentially offers to design high-performance wearable electronics for everyday use in real-world environments.

Contents

List of Figures

List of Tables

Chapter 1. Introduction

1.1 Solution-processed metal chalcogenide semiconductor

1.1.1 Hydrazine chemistry based on dimensional reduction

Inorganic compounds offer the possibility for excellent electrical properties compared to the organic systems. The properties of inorganic materials make them excellent electronic devices, but they have strong covalent bonds decrease the solubility. In 2009, Mitzi et al. proposed “Dimensional reduction” to improve the solubility of the metal chalcogenide semiconductors. Soluble precursor is a solution-processed and thermally decomposed to form a high-quality of thin film formation desired semiconductor.

Dimension reduction trading is a system where the binary solid MX_x, called a parent compound is reacted with an n-equivalent dimensional reduction agent to form A_aX a ternary child of $A_{na}MX_{x+n}$. Anion X may be the bridge or terminal ligand role for the metal center M. The metal equivalents added are incorporated into the M-X framework. ($MX_x + nA_aX \rightarrow A_{na}MX_{x+n}$) A Charge-balanced counterion A do not form a much more electropositive and powerful covalent bond than M. As shown in **Figure 1.1**a, this figure shows the gradual decomposition of the MX_3 framework, including the MX_6 octahedron linked in three dimensions through a shared corner. The first is the anion equivalent of A_aX built to connect the cutting directly into the M-X-M bridge. The resulting compound A_aMX_4 denotes a two-dimensional octahedron sheet having a common angle, as shown in **Figure 1.1**b, where the counterion A represents between layers. Additional equivalents of A_aX have left a one-dimensional chain of octahedra shared corners, as shown in **Figure 1.1**c. cuts the bridge along the other direction. The third is the equivalent discrete octahedra $[MX_6]^{z-}$ do not have ions M−X−M bridge as shown in **Figure 1.1**d. It is called saturated compounds of this last type. "Dimensional reduction" terms come to the consideration that includes a single A_aX equivalent to reducing the number of dimensions in system theory is applied by one. It has a highly integrated electropositive cations known that before reducing the size of the metal chalcogenides, the one predicted to reduce the dimensions of such system.[1]

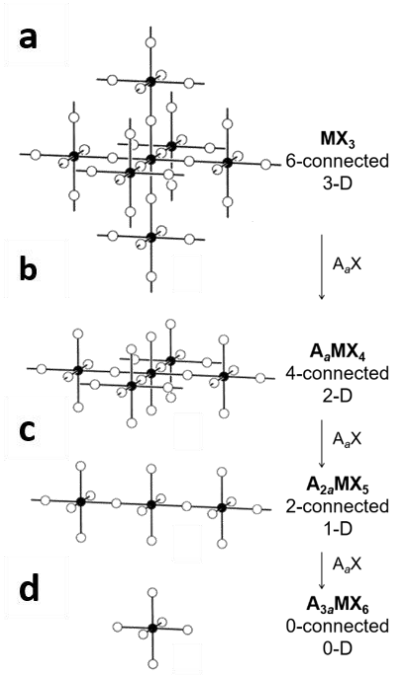

Figure 1.1. Schematic illustration of dimensional reduction of tridimensional corner-sharing MX_6 octahedron. Reproduced from Ref. 1.

The thin-film production process using "dimensional reduction" requires several steps, as shown in **Figure 1.2**. First, the expanded metal chalcogenide framework in the solution decomposes into individual metal chalcogenide anions. A metal chalcogenide precursor can be isolated. Next step includes deposition of the solution precursor on the substrate to form a solid precursor film. Generally, the spin-coating process widely uses for film deposition. The last step is heated and decomposed the precursor film to leave the targeted metal chalcogenide film.[2]

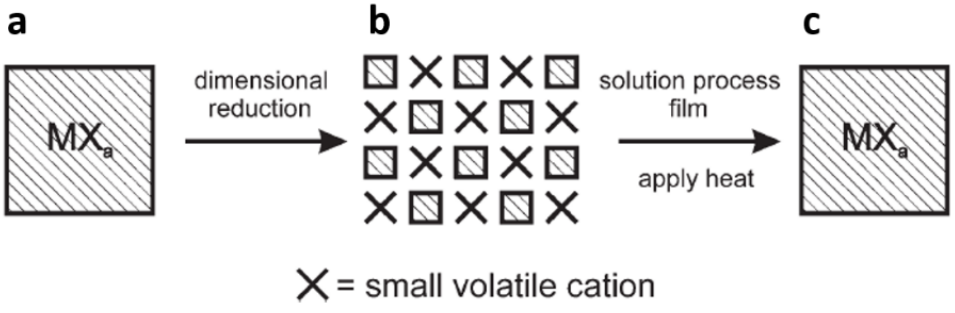

Figure 1.2. Schematic illustration of film formation using a dimensional reduction. Reproduced from Ref. 2.

The simple approach to directly improve the solubility of various metal chalcogenide such as $CuInSe_2$, $SnSe_{2-x}S_x$, $GeSe_2$, Sb_2Se_3, GeS_2, Cu_2S, Sb_2Te_3, In_2Se_3, $Cu(In,Ga)Se_{2-x}S_x$, and Ga_2Se_3.[3-10] Additional chalcogen added to hydrazine promotes the breakdown the M–X–M bond, as in the example of the reduced dimensions promote the destruction of the metal chalcogenide frame. Therefore, hydrazine separates easily from the precursor at low temperatures. The hydrazine is a powerful reducing agent, and it has a similar melting temperature and boiling temperature like water (1.4 ℃ and 113.5 ℃ respectively). Moreover, the absence of carbon and oxygen in precursors in solvents means that the clean membrane deposited after the heat treatment is possible. However, hydrazine is to be used together suitable protective measures to avoid contact with the toxic, explosive, and carcinogenic property of hydrazine have limited their extensive use.

1.1.2 Alkahest solvent systems

In the previous section, I briefly introduced hydrazine-based chemistry. Unfortunately, hydrazine is an impractical way to extend the application because of its high toxicity and highly explosive. To solve this issue, Brutchey et al. propose how simple dissolution in bulk metal chalcogenide can be advantageous for solution-processed thin films. These alkahest solvent mixtures were dissolved in a wide range of bulk materials, and the risk is low, which can have sufficient volatility for the solution treatment. [11] Vineyard et al. reported the bulk sulfur dissolution mechanism with thiol/amine mixtures. With an amine-catalyzed reaction, as shown in **Figure 1.3**. has been proposed to produce alkyl di, tri, and tetra-sulfide. In this reaction, the amine is deprotonated thiol generated nucleophilic thiolate forms. A mixture of the bulk sulfur reacts with the alkyl hydrogen polyester to form a sulfide chain following thiolate smaller polysulfide product to react with molecules and repeated.[12]

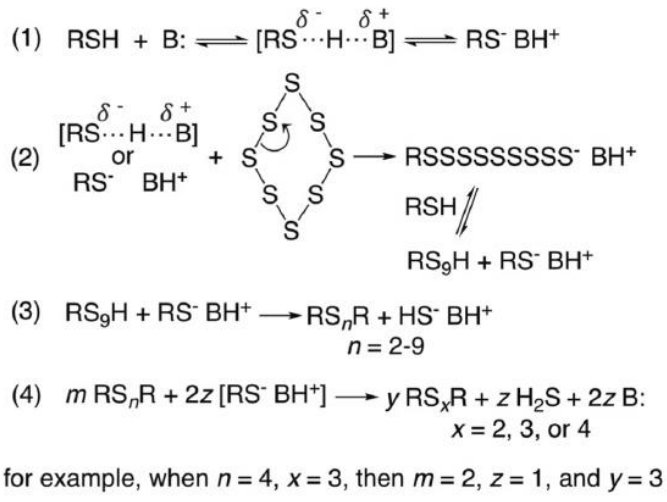

Figure 1.3. The scheme of proposed dissolution mechanism of bulk sulfur by base-catalyzed thiol-sulfur reaction. Reproduced from Ref. 13.

In 2013, Brutchey et al. first reported a binary solvent mixture of ethanedithiol (EDT) and ethylenediamine (en) nine bulk V_2VI_3 chalcogenide materials (V=As, Sb, Bi and VI = S, Se, Te), elemental chalcogens (Se, Te), and ten metal oxides (Cu_2O, ZnO, GeO_2, As_2O_3, Ag_2O, CdO, SnO, Sb_2O_3, PbO, and Bi_2O_3) dissolved at room temperature. As shown in **Figure 1.4.**, all the inks are optically transparent. This alkahest solvents provide stable inks and regenerate crystalline chalcogenide thin films through solution deposition processes such as spin coating and heat treatment process.[15]

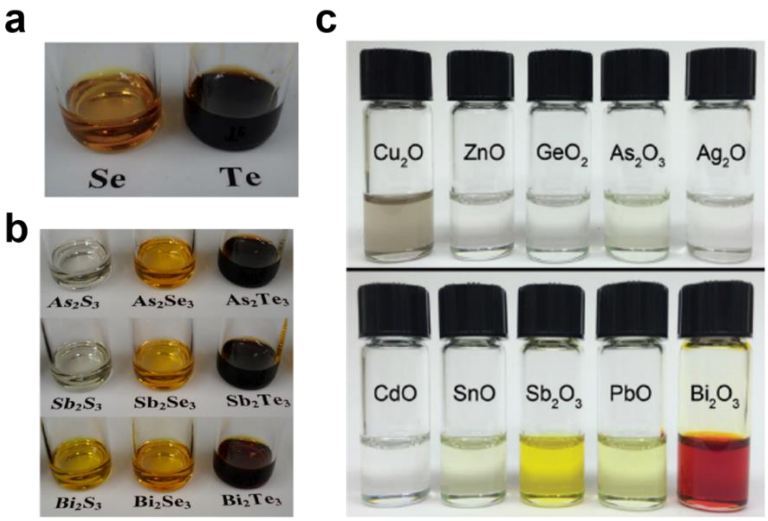

Figure 1.4. The photographs of the solutions of a) chalcogens [14], b) metal chalcogenides [11] and c) metal oxide materials [15].

Using Thermogravimetric analysis (TGA) was determined the temperature for solid inorganic phase recovery. All V_2VI_3 chalcogenide solutions indicated the thermal decomposition at 300 °C to 350 °C as shown in **Figure 1.5**a. For example, at 300 °C corresponding Bi_2S_3 solution to decompose the dry solid organic species show a multi-step weight loss of 31% at 325 °C. To support this hypothesis, the Bi_2S_3 and Sb_2Se_3 solution was drop-cast on IR-transparent substrate, dried at 100 °C. The FT-IR spectra corresponding to the other bands ν(C-H) and ν(N-H) stretches at 3300-2800 cm^{-1}. If removing the organic species, as the temperature of 350 °C proven to complete loss of stretches ν(C-H) and ν(N-H) (**Figure 1.5**b and c). Both Bi_2S_3 and Sb_2Se_3 thin films showed a uniform and high-quality crystalline realized by scanning electron microscope (SEM) in **Figure 1.5**d and e.

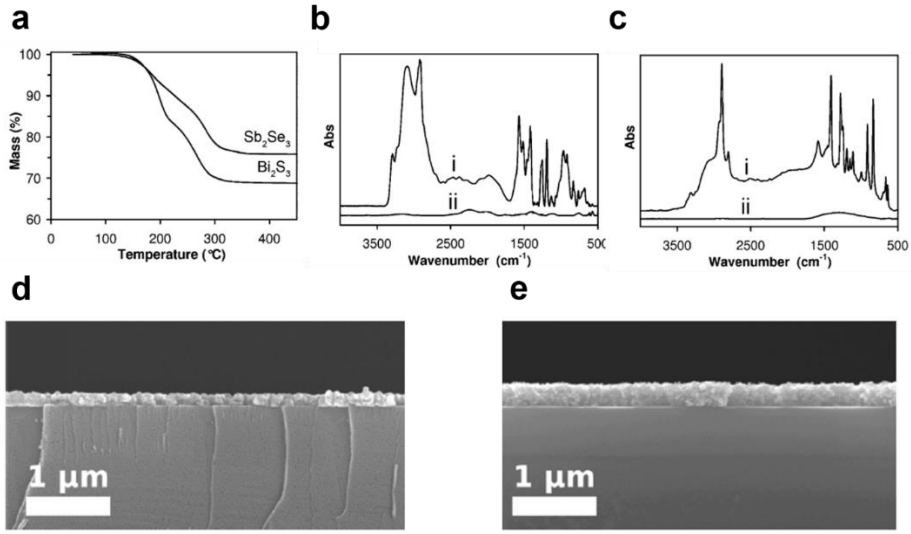

Figure 1.5. a) TGA analysis of the solid precursors Sb_2Se_3 and Bi_2S_3 in alkahest solvent. The FT-IR spectra of the dried b) Sb_2Se_3 and c) Bi_2S_3 films were subsequently heat-treated at i) 100 °C and ii) 350 °C. Cross-sectional SEM images of d) Sb_2Se_3 and e) Bi_2S_3 thin films fabricated by spin-cast. Reproduced from Ref. 11

Thus, the alkahest solvent system, the metal chalcogenides synthesized by the alkahest solvent system, is a highly crystalline thin film using a simple solution process and subsequent heat treatment. Demonstrated the usefulness of the alkahest solvent as a powerful tool for application such as Photovoltaic devices[16], electrocatalysts[17], flexible photodetectors[18], and thermoelectrics[19].

1.2 Non-volatile memory

1.2.1 Introduction

In the high-tech age, electronic memory is essential to enable new applications. In the memory hierarchy, it is divided into volatile and nonvolatile memory. A volatile memory system for storing the state requires a power source, and a non-volatile memory system can memorize the state without power. Non-volatile memory technology of Si-based electronic devices dating return to the 1990s. Field-Effect Transistor (FET) was one of the most promising devices to replace the then existing flash memory in the face of physical scaling limit. Three major functional components of today's memory components are density, non-volatile, and speed. This is because, in the Internet of Things (IoT) era, appliances are such as ultra-low power consumption, low-cost design, high-density, high reliability, long data storage capabilities, and data data-driven applications with new requirements. Unfortunately, DRAM and NAND Flash do not meet all the three major elements. DRAM has fast but non-volatile. After three attributes to develop new memory with all memory/storage systems while greatly increasing its

efficiency, it can significantly reduce energy consumption. The goal is to develop new memory for universal memory with all of these characteristics. For decades to develop new memory such as magnetic random-access memory (MRAM), spin-transfer torque magnetic random-access memory (STT-MRAM), ferroelectric random-access memory (FeRAM), phase-change memory (PCM), and resistive random-access memory (RRAM). These are non-volatile data memories is a new technology that stores more data at a lower cost than silicon chips, leading to a potential future alternative to traditional memory of future computing systems. This chapter also looks at the RRAM (resistive random-access memory) device using materials, the switching mode, and the switching mechanism.

1.2.2 Magnetic Random Access Memory (MRAM)

STT-MRAM is a form of non-volatile memory that stores data in magnetic domains. The basic cell structure of STT-MRAM is shown in **Figure 1.6**. The STT-MRAM is a magnetic memory to take advantage of the fundamental platform built by MRAM's memory to enable scalable non-volatile memory solutions for advanced process nodes.[20] MRAM stores data in accordance with the magnetization direction of each bit, and nano magnetic fields are set a bit of the existing MRAM. Although the write speed is known to be very fast compared to PRAM and RRAM, it has not reached full-scale commercialization due to low resistance, small sensing signals, still large switching currents, and lack of reliability of non-volatile characteristics.[21] Current memory technologies such as NAND Flash and DRAM have practical advantages, and MRAM has played a niche role in the market.

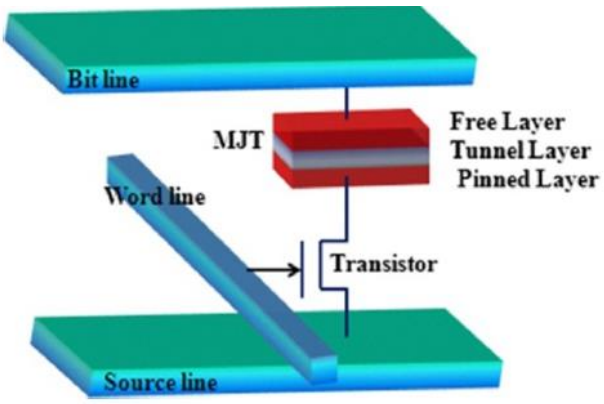

Figure 1.6. The basic structure of STT-MRAM cell.

1.2.3 Ferroelectric Random Access Memory (FeRAM)

FeRAM is a non-volatile RAM that combines fast read and writes access to the DRAM cells consists of a capacitor and a transistor structure, as shown in **Figure 1.7**. The transistor will have access to the cell to sense the state of the ferroelectric capacitor dielectric. The polarization properties of the ferroelectric material is used as a memory devices. Today's FeRAM is a consideration for using

materials such as lead zirconate titanate (PZT). FeRAM can replace the growth that provides the same functionality as flash memory. FeRAM has low power consumption, fast write/erase speed, and high endurance (10^{10} – 10^{14} cycles). The one drawback of the FeRAM read process is destructive and needs to post-read write architecture. The read method includes writing a bit in each cell.[22] When the cell's state changes, it detects a small current pulse by indicating that the cell in the OFF state. However, FeRAM has the following requirements because fast memory that can withstand high endurance cycles.

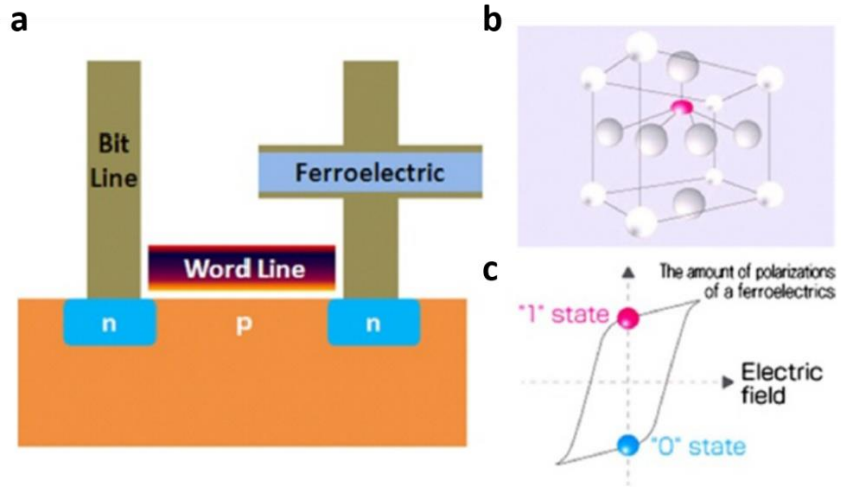

Figure 1.7. a) The basic structure of FeRAM cell. b) The crystal structure of ferroelectric materials. c) Electric polarization-electric field hysteresis curves.

1.2.4 Phase-change Random Access Memory (PRAM)

The materials of this memory are as chalcogenide glass is heated in a low-resistance crystal phases change to high resistance amorphous phases. PRAM, also known as chalcogenide RAM, can exist in two different phase states (crystal and amorphous phase), a type of non-volatile RAM.[23,24] The basic PRAM cell structure is shown in **Figure 1.8**. Most of the phase-change material includes one or more elements of a chalcogenide material in periodic table group 6 to create a memory device. PRAM can be turned on or off a current that represents the digital high and low states. This process takes tens of nanoseconds.[25] Write speed is 10 to 20 times slower than the problem one hundred times faster than DRAM Flash approximately 1μs. Thanks to the short time, write, and delete PCM is a several times faster than conventional flash memory and uses low power consumption. PCM has the potential to provide high-speed, high-density, non-volatile storage with unprecedented economies of scale. PRAM is also known as a complete RAM because it can be overwritten without erasing the data first.

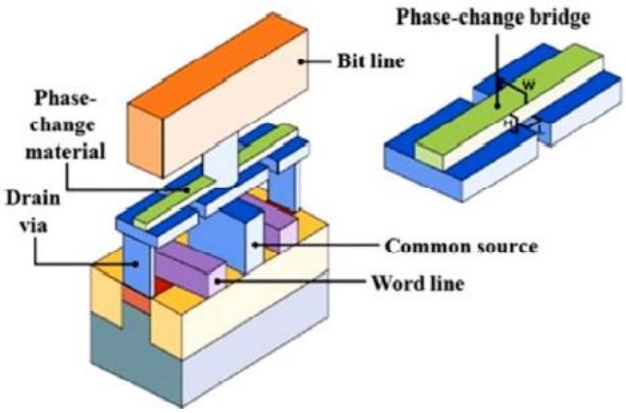

Figure 1.8. The basic structure of PRAM cell.

1.3 Resistive Random Access Memory (RRAM)

1.3.1 The structure of RRAM

Resistive switching memory of RRAM is usually composed of an insulating or resistive material 'I' sandwiched between an M-I-M structure, electron conductor 'M'. The material of 'I' is typically a metal oxide or chalcogenides represents the first ionic conductivity[1] as shown in **Figure 1.9**.

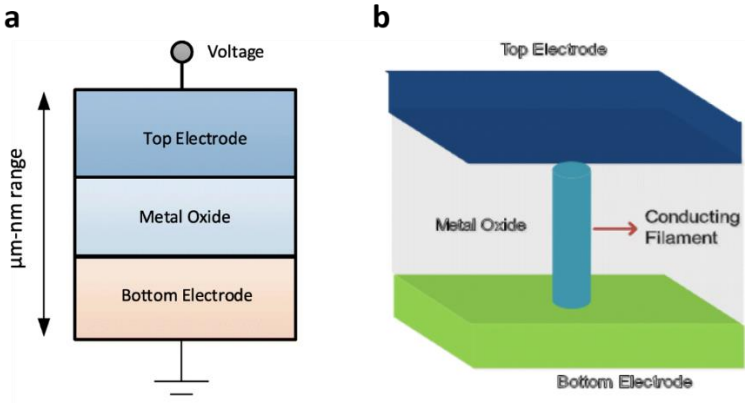

Figure 1.9. a) The structure of metal-insulator-metal RRAM. b) Cross-section view of RRAM. Reproduced from Ref. 26

1.3.2 Resistance Switching Modes

According to the polarity of the applied voltage, RRAM can be classified into two switching modes, 1) unipolar switching and 2) bipolar switching. [26] Unipolar switching is polarity independent. As shown in **Figure 1.10**a. Polarity is the same but can occur if different switching voltage magnitude. Unipolar switching to interpret the joule heating by the physical mechanism is conductive filament breaks during the reset operation. On the other hand, in bipolar switching in the switching process (set and reset) will

return in the RRAM cell to the opposite polarity to HRS as shown in **Figure 1.10**b. Applying a compliance current to the RRAM device ensures that the dielectric is not permanently destroyed during the RRAM formation/hardening process.

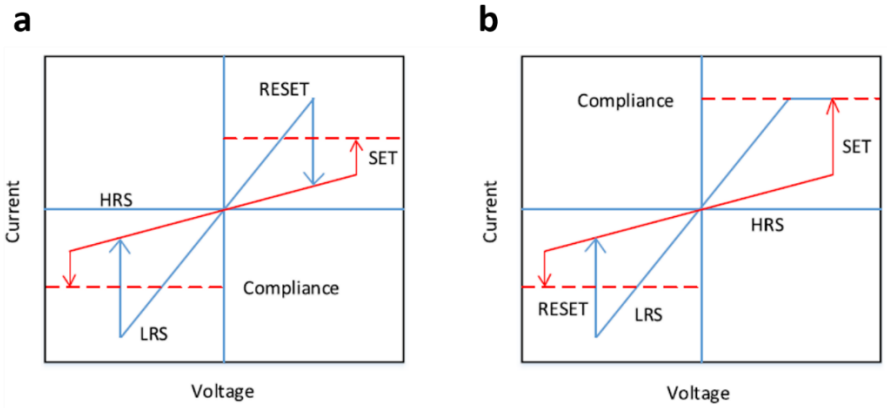

Figure 1.10. The I-V curve for RRAM. a) unipolar and b) bipolar switching. Compliance current is adopted during the SET process to prevent breakdown. Reproduced from Ref. 26.

1.3.3 Materials of RRAM

RRAM devices are typically configured as a storage layer and sandwiched between two electrodes. Therefore, materials related to the RRAM are described separately below, for this can be classified as storage (Insulator) and electrode materials (Metal).

The RRAM properties have been observed in some insulators and semiconductors, such as metal oxide and chalcogenide materials. The resistance change occurs under the electric field. Some insulator was observed applying an electric field is applied to the resistance change occurs. This change in resistance characteristics has been investigated recently for the development of future non-volatile memories.[27] It has been observed in various oxides, such as HfO_x[28], TiO_x[29], TaO_x[30], NiO[31], ZnO[32], Zn_2TiO_4[33], MnO_x[34], MgO[35], and AlO_x[36] has been studied. These metal oxides are generally deposited by pulsed laser deposition (PLD), atomic layer deposition (ALD), and reactive sputtering. However, ALD is a widely preferred method because it can accurately control the thickness and uniformity of thin films.

The electrode material is important because it serves as a carrier transmission path. In RRAM, electrode material has a significant effect on the switching behavior of the device. The commonly used electrodes are Ag[32], Al[36], Ti[37], Cu[38], graphene[39], carbon nanotubes[40], W[41], and Pt[42]. Filament formation of the memory cells is occurred by subsequent deposition or reduction, a cation (Cu^+ or Ag^+) movement, and the subsequent deposition of the inert or reducing the bottom metal electrodes (most commonly Ag or Cu).[43] Therefore, RRAM is controlled by the formation and annihilation of resistive switching metal filaments.

1.3.4 Switching mechanism

The switching mechanism of RRAM cells is based on the growth of the dielectric or semiconducting inside conductive filaments (CFs). The conductive filaments have a very small diameter in the order of nanometers scale for connecting the upper and lower electrodes of the memory. The filaments with the high resistance state (HRS) were generated when separated by a gap between the electrodes connected to the conductive filament is applied to the low resistance state (LRS). [44] The RRAM can be classified into two categories. First, also known as Conductive bridge random access memory (CBRAM), is an electrochemical metallization memory (ECM). CBRAM is based on movement and subsequent redox(reduction and oxidation) reactions of metal ions,[45,46] A general mechanism of ECM is shown in **Figure 1.11**. The other is Balance Change Memory (VCM), also known as oxygen defect filament-based RRAM (OxRRAM). VCM is based on a rearrangement of the oxygen ions and subsequent movement of the oxygen vacancies defects, enabling the forming of a conductive filament between the upper electrode and the lower electrode.[47]

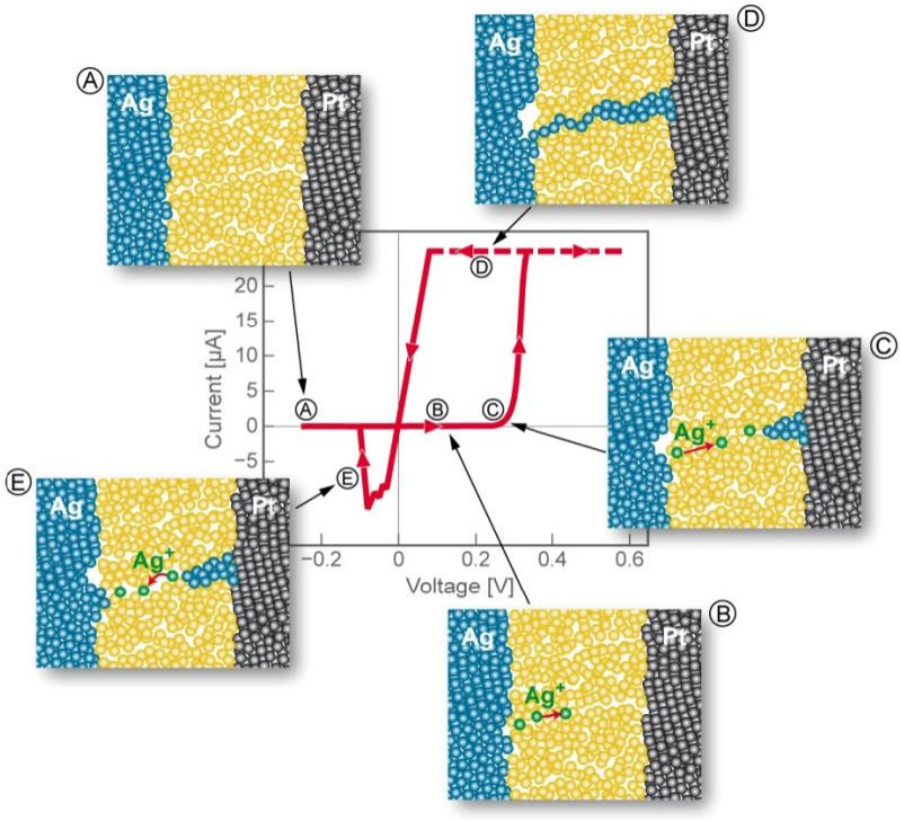

Figure 1.11. The electrochemical metallization memory (ECM) SET and RESET operations step of the cell. Reproduced from Ref. 46.

A) Initial high-resistance state (HRS)

B) Anodic dissolution of metallic material (M) to the reaction, where M^{z-} represents the metal cations in the solid electrolyte thin film.

$M \rightarrow M^{z+} + ze^-$

C) Movement of the metal cations (M^{z+}) to inert electrode driven by the electric field.

D) Reduction of metal cations (M^{z+}), the cell retains the low-resistance state (LRS).

$M^{z+} + ze^- \rightarrow M$

E) Dissolution of the metal filament to initial high-resistance state (HRS).

Reference

[1] Tulsky, E. G.; Long, J. R., Dimensional Reduction: A Practical Formalism for Manipul ating Solid Structures. *Chem. Mater.* **2001,** *13* (4), 1149-1166.

[2] Mitzi, D. B., Solution Processing of Chalcogenide Semiconductors via Dimensional Red uction. *Adv.Mater.* **2009,** *21* (31), 3141-3158.

[3] Mitzi, D. B., N4H9Cu7S4: a hydrazinium-based salt with a layered Cu_7S_4- framework. *I norg. Chem.* **2007,** *46* (3), 926-31.

[4] Mitzi, D. B.; Raoux, S.; Schrott, A. G.; Copel, M.; Kellock, A.; Jordan-Sweet, J., Solution-Based Processing of the Phase-Change Material KSb_5S_8. *Chem. Mater.* **2006,** *18* (26), 6278-6282.

[5] Milliron, D. J.; Mitzi, D. B.; Copel, M.; Murray, C. E., Solution-Processed Metal Ch alcogenide Films for p-Type Transistors. *Chem. Mater.* **2006,** *18* (3), 587-590.

[6] Mitzi, D. B., Polymorphic one-dimensional $(N_2H_4)_2ZnTe$: soluble precursors for the form ation of hexagonal or cubic zinc telluride. *Inorg. Chem.* **2005,** *44* (20), 7078-86.

[7] Mitzi, D. B., Synthesis, structure, and thermal properties of soluble hydrazinium germani um(IV) and tin(IV) selenide salts. *Inorg. Chem.* **2005,** *44* (10), 3755-61.

[8] Mitzi, D. B.; Copel, M.; Chey, S. J., Low-Voltage Transistor Employing a High-Mobil ity Spin-Coated Chalcogenide Semiconductor. *Adv. Mater.* **200,** *17* (10), 1285-1289.

[9] Mitzi, D. B.; Kosbar, L. L.; Murray, C. E.; Copel, M.; Afzali, A., High-mobility ult rathin semiconducting films prepared by spin coating. *Nature* **2004,** *428* (6980), 299-30 3.

[10] Mitzi, D. B.; Copel, M.; Murray, C. E., High-Mobility p-Type Transistor Based on a Spin-Coated Metal Telluride Semiconductor. *Adv.Mater.* **2006,** *18* (18), 2448-2452.

[11] Webber, D. H.; Brutchey, R. L., Alkahest for V_2VI_3 chalcogenides: dissolution of nine bulk semiconductors in a diamine-dithiol solvent mixture. *J. Am. Chem. Soc.* **2013,** *135* (42), 15722-5.

[12] Vineyard, B. D., Versatility and the mechanism of the n-butyl-amine-catalyzed reaction of thiols with sulfur. J. Org. Chem. ***1967***, *32* (12), 3833–3836.

[13] McCarthy, C. L.; Brutchey, R. L., Solution processing of chalcogenide materials using t hiol-amine "alkahest" solvent systems. *Chem. Commun.* **2017,** *53* (36), 4888-4902.

[14] Webber, D. H.; Buckley, J. J.; Antunez, P. D.; Brutchey, R. L., Facile dissolution of selenium and tellurium in a thiol–amine solvent mixture under ambient conditions. *Che m.* **2014,** *5* (6).

[15] McCarthy, C. L.; Webber, D. H.; Schueller, E. C.; Brutchey, R. L., Solution-Phase C onversion of Bulk Metal Oxides to Metal Chalcogenides Using a Simple Thiol-Amine S

olvent Mixture. *Angew. Chem. Int. Ed. Engl.* **2015,** *54* (29), 8378-81.

[16] Yang, Y.; Wang, G.; Zhao, W.; Tian, Q.; Huang, L.; Pan, D., Solution-processed highly efficient $Cu_2ZnSnSe_4$ thin film solar cells by dissolution of elemental Cu, Zn, Sn, and Se powders. *ACS Appl. Mater. Interfaces.* **2015,** *7* (1), 460-4.

[17] McCarthy, C. L.; Brutchey, R. L., Preparation of electrocatalysts using a thiol-amine solution processing method. *Dalton. Trans.* **2018,** *47* (15), 5137-5143.

[18] Hasan, M. R.; Arinze, E. S.; Singh, A. K.; Oleshko, V. P.; Guo, S.; Rani, A.; Cheng, Y.; Kalish, I.; Zaghloul, M. E.; Rao, M. V.; Nguyen, N. V.; Motayed, A.; Davydov, A. V.; Thon, S. M.; Debnath, R., An Antimony Selenide Molecular Ink for Flexible Broadband Photodetectors. *Adv. Electron. Mater.* **2016,** *2* (9).

[19] Ma, Y.; Vartak, P. B.; Nagaraj, P.; Wang, R. Y., Thermoelectric properties of copper chalcogenide alloys deposited via the solution-phase using a thiol–amine solvent mixture. *RSC Advances* **2016,** *6* (102), 99905-99913.

[20] Khvalkovskiy, A. V.; Apalkov, D.; Watts, S.; Chepulskii, R.; Beach, R. S.; Ong, A.; Tang, X.; Driskill-Smith, A.; Butler, W. H.; Visscher, P. B.; Lottis, D.; Chen, E.; Nikitin, V.; Krounbi, M., Erratum: Basic principles of STT-MRAM cell operation in memory arrays. *J. Phys. D Appl. Phys.* **2013,** *46* (13).

[21] Bhatti, S.; Sbiaa, R.; Hirohata, A.; Ohno, H.; Fukami, S.; Piramanayagam, S. N., Spintronics based random access memory: a review. *Mater. Today* **2017,** *20* (9), 530-548.

[22] Meena, J. S.; Sze, S. M.; Chand, U.; Tseng, T. Y., Overview of emerging nonvolatile memory technologies. *Nanoscale Res. Lett.* **2014,** *9* (1), 526.

[23] Hudgens, S.; Johnson B., Overview of phase-change chalcogenide nonvolatile memory technology. *MRS Bull **2004**, 29* (11), 829–832.

[24] Pirovano, A.; Lacaita, AL.; Benvenuti, A.; Pellizzer, F.; Hudgens, S.; Bez, R,; Scaling analysis of phase-change memory technology. In Int Elec Dev Meet (IEDM) Tech Dig: December 8-10 2003; Washington, DC. Piscataway: IEEE; 2003:29.6.1–29.6.4.

[25] Atwood, G.; Bez, R., Current status of chalcogenide phase change memory. In 63rd Device Research Conf Dig (DRC '05): June 22 1005; Santa Barbara,Volume 1. Piscataway: IEEE; 2005:29–33.

[26] Zahoor, F.; Azni Zulkifli, T. Z.; Khanday, F. A., Resistive Random Access Memory (RRAM): an Overview of Materials, Switching Mechanism, Performance, Multilevel Cell (mlc) Storage, Modeling, and Applications. *Nanoscale Res. Lett.* **2020,** *15* (1), 90.

[27] Chang, T.-C.; Chang, K.-C.; Tsai, T.-M.; Chu, T.-J.; Sze, S. M., Resistance random access memory. *Mater. Today* **2016,** *19* (5), 254-264.

[28] Su, Y.-T.; Wang, M.-C.; Zhang, S.; Wang, H.; Sze, S. M.; Liu, H.-W.; Chen, P.

-H.; Chang, T.-C.; Tsai, T.-M.; Chu, T.-J.; Pan, C.-H.; Wu, C.-H.; Yang, C.-C., A Method to Reduce Forming Voltage Without Degrading Device Performance in Hafnium Oxide-Based 1T1R Resistive Random Access Memory. *IEEE J. Electron Devices Soc.* **2018,** *6*, 341-345.

[29] Huang, Y.-J.; Shen, T.-H.; Lee, L.-H.; Wen, C.-Y.; Lee, S.-C., Low-power resistive random access memory by confining the formation of conducting filaments. *AIP Advances* **2016,** *6* (6).

[30] Prakash, A.; Deleruyelle, D.; Song, J.; Bocquet, M.; Hwang, H., Resistance controllability and variability improvement in a TaO_x-based resistive memory for multilevel storage application. *Appl. Phys. Lett.* **2015,** *106* (23).

[31] Ma, G.; Tang, X.; Zhang, H.; Zhong, Z.; Li, J.; Su, H., Effects of stress on resistive switching property of the NiO RRAM device. *Microelectronic Eng.* **2015,** *139*, 43-47.

[32] Huang, Y.; Shen, Z.; Wu, Y.; Wang, X.; Zhang, S.; Shi, X.; Zeng, H., Amorphous ZnO based resistive random access memory. *RSC Adv.* **2016,** *6* (22), 17867-17872.

[33] Chen, S.-X.; Chang, S.-P.; Hsieh, W.-K.; Chang, S.-J.; Lin, C.-C., Highly stable ITO /Zn_2TiO_4/Pt resistive random access memory and its application in two-bit-per-cell. *RSC Adv.* **2018,** *8* (32), 17622-17628.

[34] Zhang, S.; Long, S.; Guan, W.; Liu, Q.; Wang, Q.; Liu, M., Resistive switching characteristics of MnO_x-based ReRAM. *J. Phys. D Appl. Phys.* **2009,** *42* (5).

[35] Chiu, F.-C.; Shih, W.-C.; Feng, J.-J., Conduction mechanism of resistive switching films in MgO memory devices. *J. Appl. Phys.* **2012,** *111* (9).

[36] Wu, Y.; Lee, B.; Wong, H. S. P., Al_2O_3-Based RRAM using atomic layer deposition (ALD) with 1-μA RESET current. *IEEE Electron Device Lett.* **2010,** *31* (12), 1449-1451.

[37] Yang, M. K.; Park, J.-W.; Ko, T. K.; Lee, J.-K., Bipolar resistive switching behavior in Ti/MnO_2/Pt structure for nonvolatile memory devices. *Appl. Phys. Lett.* **2009,** *95* (4).

[38] Yang, L.; Kuegeler, C.; Szot, K.; Ruediger, A.; Waser, R., The influence of copper top electrodes on the resistive switching effect in TiO_2 thin films studied by conductive atomic force microscopy. *Appl. Phys. Lett.* **2009,** *95* (1).

[39] Son, J. Y.; Shin, Y. H.; Kim, H.; Jang, H. M., NiO resistive random access memory nanocapacitor array on graphene. *ACS Nano* **2010,** *4* (5), 2655-8.

[40] Tsai, C. L.; Xiong, F.; Pop, E.; Shim, M., Resistive random access memory enabled by carbon nanotube crossbar electrodes. *ACS Nano* **2013,** *7* (6), 5360-6.

[41] Prakash, A.; Park, J.; Song, J.; Woo, J.; Cha, E.-J.; Hwang, H., Demonstration of

Low Power 3-bit Multilevel Cell Characteristics in a TaO_x-Based RRAM by Stack Engineering. *IEEE Electron Device Lett.* **2015,** *36* (1), 32-34.

[42] Chiu, F. C.; Li, P. W.; Chang, W. Y., Reliability characteristics and conduction mechanisms in resistive switching memory devices using ZnO thin films. *Nanoscale Res. Lett.* **2012,** *7* (1), 178.

[43] Goux, L.; Valov, I., Electrochemical processes and device improvement in conductive bridge RAM cells. *physica status solidi (a)* **2016,** *213* (2), 274-288.

[44] Kumar, D.; Aluguri, R.; Chand, U.; Tseng, T. Y., Metal oxide resistive switching memory: Materials, properties and switching mechanisms. *Ceramics International* **2017,** *43*, S547-S556.

[45] Kozicki, M. N.; Barnaby, H. J., Conductive bridging random access memory—materials, devices and applications. *Semicond. Sci. Technol.* **2016,** *31* (11).

[46] Valov, I.; Waser, R.; Jameson, J. R.; Kozicki, M. N., Electrochemical metallization memories—fundamentals, applications, prospects. *Nanotechnology* **2011,** *22* (28).

[47] Wong, H. S. P.; Lee, H.-Y.; Yu, S.; Chen, Y.-S.; Wu, Y.; Chen, P.-S.; Lee, B.; Chen, F. T.; Tsai, M.-J., Metal–Oxide RRAM. *Proceedings of the IEEE* **2012,** *100* (6), 1951-1970.

Chapter 2. Solution-processed stretchable Ag_2S semiconductor thin films for wearable self-powered nonvolatile memory

(Parts of this chapter was published in the article, "Solution-processed stretchable Ag_2S semiconductor thin films for wearable self-powered nonvolatile memory" and reproduced with permission from *Adv. Mater.* **2021**, 2100066.)

2.1 Introduction

Flexible and stretchable electronics, including deformable sensors, displays, memories, and energy devices, have gained significant attention because they can be used for smart wearable devices that collect and store personal, physiological information for medical and healthcare monitoring.[1-7] The development of these advanced electronics is mostly dependent on the development and discovery of materials with desirable electrical and mechanical properties. Recently, significant progress has been made in the development of stretchable insulators and conductors, including polymeric dielectrics, metal nanowire, and conjugate polymer composites.[8-12] However, finding stretchable semiconductors candidates with appropriate bandgap and related electrical performance as well as mechanical and environmental durability was challenging.[13,14] For instance, conventional inorganic semiconductors held in ionic bonds or covalent bonds are intrinsically brittle and showing only the strain of about 0.1 to 0.2%,[15-17] resulting in accumulated fatigue and mechanical cracks, while organic semiconductors are vulnerable to humidity, chemical and thermal stresses, and their inferior electrical properties.[18-21] Therefore, the criteria for the future deformable semiconductor devices cannot fulfil.

Recently, α-Ag_2S bulk crystals is considered a promising candidate for the production of deformable semiconductor layers in flexible and stretchable electronics due to its owing to their special electrical and mechanical properties.[22-25] α-Ag_2S bulk crystals exhibit both semiconducting behavior and intrinsic ductility, similar to metals, resulting from unique crystallographic characteristics such as very low slippage energy and high cleavage energy between the crystal planes.[22] These unusual properties of α-Ag_2S compounds are strongly related to their chemical bonding, such as the Ag–S octagon frameworks, which inhibits randomly distributed Ag–Ag metallic bonding and suppress crystal cleavage.[26] These are in stark contrast to the brittleness observed in conventional inorganic semiconductors consisting of covalent or ionic bonds, which typically cause repulsion at the cleavage planes.[22] However, despite its great potential, the practical applications of this compound remains very early stages. Although recent several studies reported the use of Ag_2S bulk ingots in energy devices, but due to limited synthesis procedures, Ag_2S thin films-based stretchable electronics have never been realized. The typical synthetic procedures for producing α-Ag_2S crystals require harsh processing conditions, such as

temperatures above 500 °C or complicated deposition equipment set-up,[22,27-29] limiting both the available substrates and processing temperatures for the fabrication of flexible and stretchable electronics.

Resistive random access memory (RRAM) has been considered the next-generation nonvolatile memory device because it demonstrates a high operation speed, low power consumption, improved reliability of program/erase cycle, and scalability.[30-33] In addition, the resistive switching effect of the RRAM cells mainly results from the reversible formation and annihilation of conductive channels in the active semiconductor layer of a metal-semiconductor-metal device structure.[34-37] Metal oxides and chalcogenides compounds, such as TiO_x, MoS_2, WO_x and Cu_2S, were comhave been used as semiconductor layers in RRAM devices.[38-41] However, due to their limited plasticity, only several reports have realized the limited flexibility of resistive switching devices that contain inorganic semiconductors.[42-44] Accordingly, most studies regarding deformable resistive memory devices have focused on organic- and composite-based semiconductors,[45-52] giving rise to unresolved material-related issues of insufficient durability as well as low performance.

Here, I present the intrinsically stretchable, wafer-scale Ag_2S thin films fabricated by a low-cost and scalable solution process. The fabricated thin film has been determined to exhibit the intrinsic mechanical stretchability of the tensile strain of 14.9%. In addition, RRAM device were fabricated with a wrinkled Ag_2S thin film, exhibited bipolar switching characteristics, satisfying the expected properties of a favorable I_{on}/I_{off} ratio, operational endurance, and retention properties. In particular, the device showed 52% mechanical stretchability when the wrinkled Ag_2S layer reached its fully stretched state, without the loss of electrical properties. Furthermore, I demonstrated the extremely high thermal and chemical durability of this inorganic RRAM device by performing uniform operations under thermal stresses at temperatures from –196 to 300 °C and the chemical stresses by exposure to various hydrophilic, hydrophobic, and ionic environments, especially sustaining the switching properties for 168 h in 85 °C/85% relative humidity. Finally, the integration of memory devices and motion sensors enables the self-powered, and a smart and wearable healthcare-monitoring system for long-term data storage.

2.2 Results and discussion

2.2.1 Solution-processed fabrication of Ag_2S thin films

Figure 2.1a-b shows the solution-processed fabrication of the uniformly deposited crystalline Ag_2S thin films. High-quality Ag_2S thin film fabrication was realized by the purification of an Ag_2S ink solution from the as-synthesized mixed phases and heat treatment of the as-deposited thin film under

an S-ambient environment. The initial solution of Ag_2S was synthesized by dissolving Ag_2S powder in a mixture of ethylenediamine and ethanedithiol,[53-55] which was further purified and finally dissolved in ethylenediamine. The UV-Vis absorption spectra of the as-synthesized and purified Ag_2S solutions showed the same absorption peaks at 360 and 520 nm, indicating that the dissolved Ag_2S molecules maintained their basic structures after the purification process (**Figure 2.2**). However, the composition of the purified complex changed the Ag:S ratio from 2:1 to 2:3, suggesting the exclusion of the byproduct of Ag-rich complexes during the purification process.[56,57] These Ag-rich complexes in the as-synthesized solution deteriorated the microstructures in the spin-coated thin film, as shown in the scanning electron microscopy (SEM) image (**Figure 2.3**a), which can be attributed to different decomposition behaviors of mixed complexes. In contrast, the purified solution used a spin coating process to form a very uniform thin film with perfect surface coverage on the substrate (**Figure 2.3**b). The atomic force microscopy (AFM) and interferometric scattering microscopy images of the Ag2S thin films fabricated on further demonstrate the film uniformity with the root-mean-square surface roughness of 6.69 nm and 13.05 nm obtained from the height profiles (**Figure 2.4**).

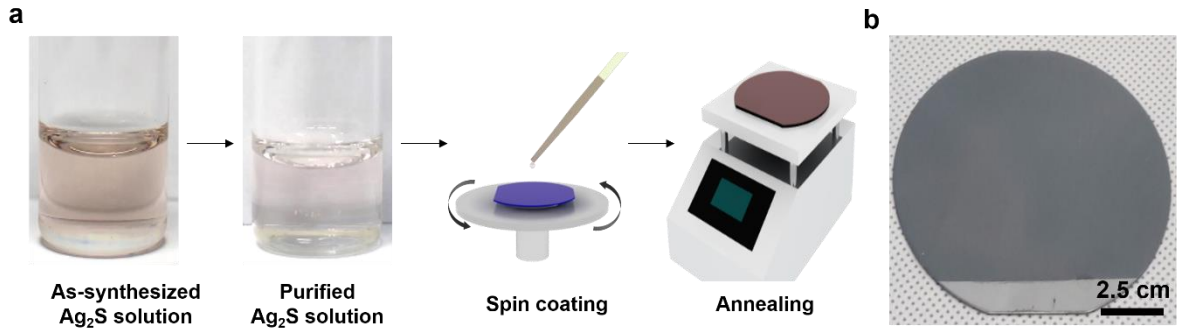

Figure 2.1. a) Schematic illustration of the fabrication of Ag_2S thin film by a solution process. b) Photograph of Ag_2S thin film fabricated on a 4-inch wafer.

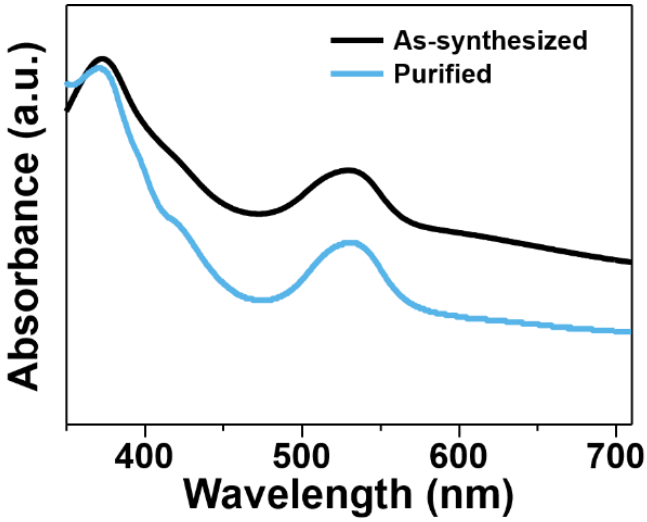

Figure 2.2. UV-Vis absorption spectra of as-synthesized and purified Ag_2S solution.

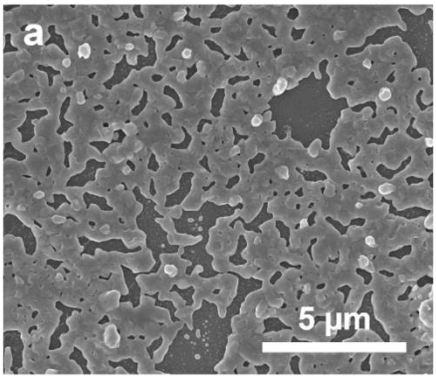

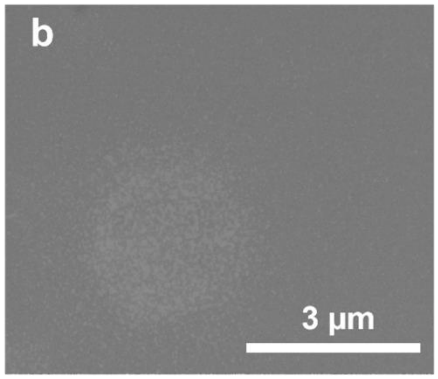

Element	*Wt%*	*At%*
S K	30.73	59.88
Ag L	69.27	40.12

Figure 2.3. SEM images of thin films prepared using a) as-synthesized Ag_2S solution, b) purified Ag_2S solution. The atomic and weight compositions of b) were estimated by EDS analysis.

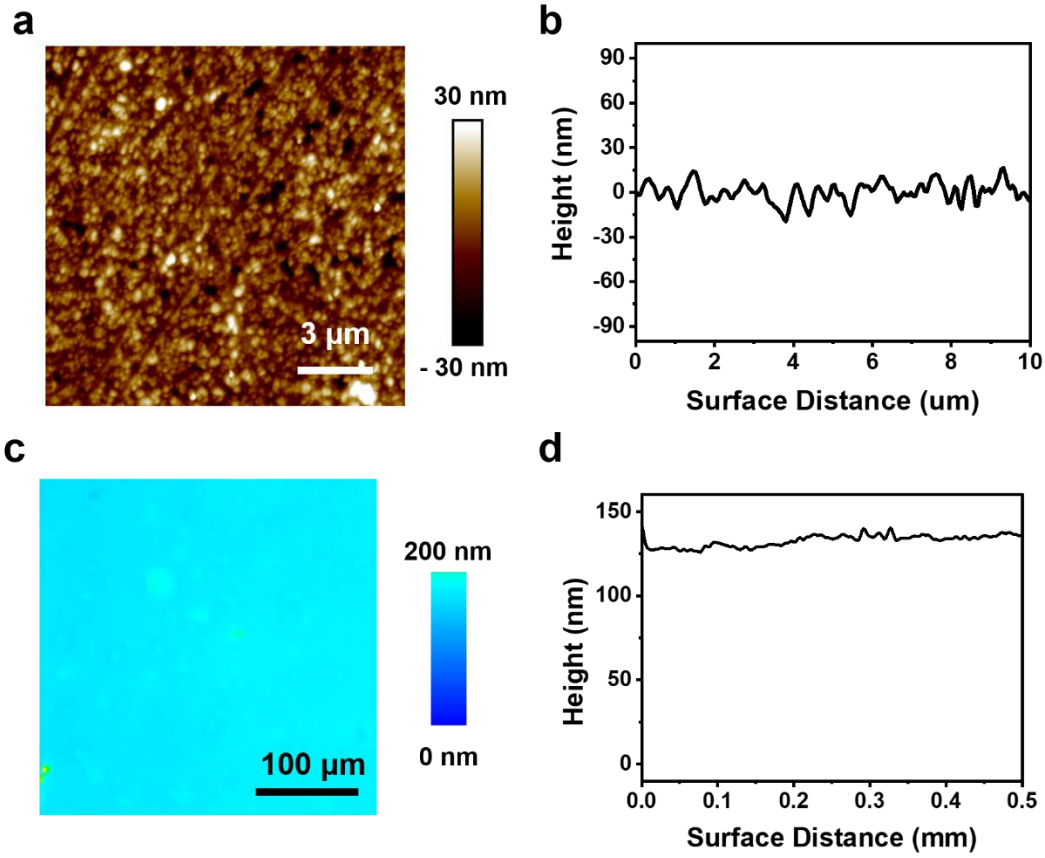

Figure 2.4. a) AFM image of the Ag_2S thin film and b) the corresponding height profile. c) Interferometric scattering microscopy image the Ag_2S thin film and d) the corresponding height profile.

Thermogravimetric analysis (TGA) of the purified Ag_2S solution demonstrated that a sharp decrease in weight began at approximately 180 °C, which was attributed to the thermal decomposition of the molecular Ag_2S complex (**Figure 2.5**). Based on the TGA result, the as-deposited thin films were further heat-treated at 300 °C to completely decompose the Ag_2S complex and form a crystalline Ag_2S phase. The heat treatment was performed under an S-ambient environment, which was beneficial for formation of stoichiometric Ag_2S thin film by preventing undesirable excessive S evaporation. Heat treatment under an N_2 environment led to structures embedded with nanoparticles **(Figure 2.6**a) due to excessive S evaporation. Selective energy dispersive X-ray spectroscopy (EDS) analysis demonstrated that the nanoparticles were the Ag-rich phase **(Figure 2.6**b), which was further supported by the X-ray diffraction (XRD) pattern showing mixed phases corresponding to Ag and Ag_2S (JCPDS 00-004-0783 and 00-014-0072) (**Figure 2.7**). In contrast, under the S-ambient environment, annealed thin films showed a continuous microstructure with complete fusion of nanoscale grains across the entire area (**Figure 2.8**). The photograph of the thin film displayed mirror-like specular reflection, which showed the highly uniform thin film surface (**Figure 2.1**b). The XRD pattern of the thin film was indexed to

the Ag_2S bulk crystal, and no impurity-related phases were not observed (**Figure 2.9**). Moreover, the peaks indexed to the (012), (013), and (014) planes were more pronounced than others, indicating that the Ag_2S thin film preferentially grew along the (01*l*) plane. These results demonstrate the realization of a high-quality Ag_2S thin film through solution-processed deposition and subsequent heat treatment at the optimized conditions.

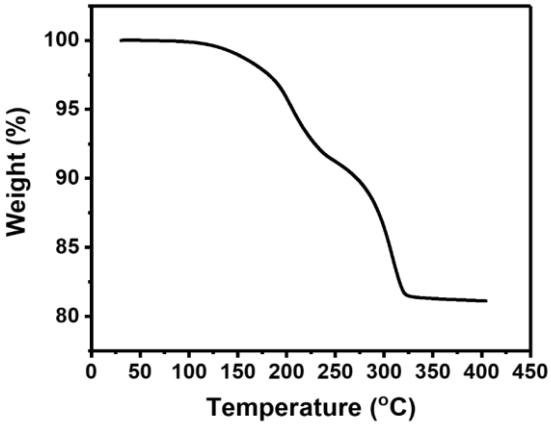

Figure 2.5. TGA analysis of the purified Ag_2S precursor.

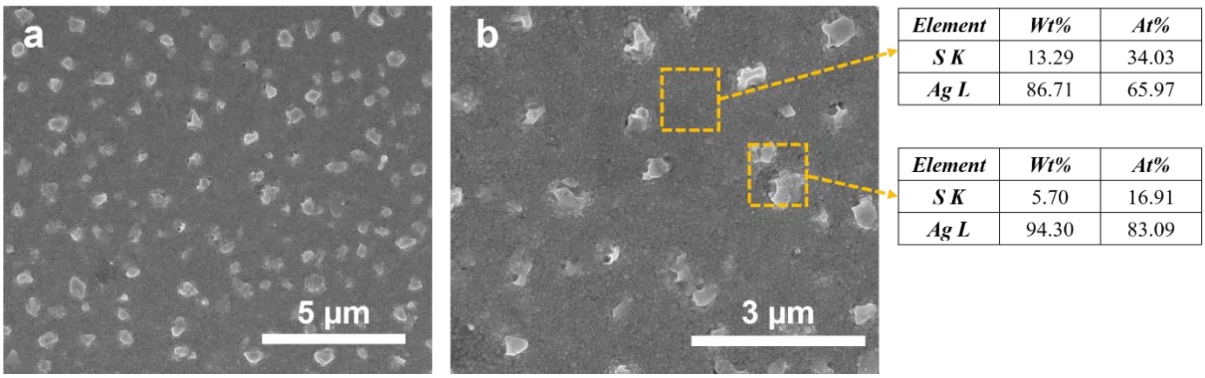

Figure 2.6. SEM images of prepared using purified thin films after annealing at 300 °C. The atomic and weight compositions were estimated at boxed region by EDS analysis.

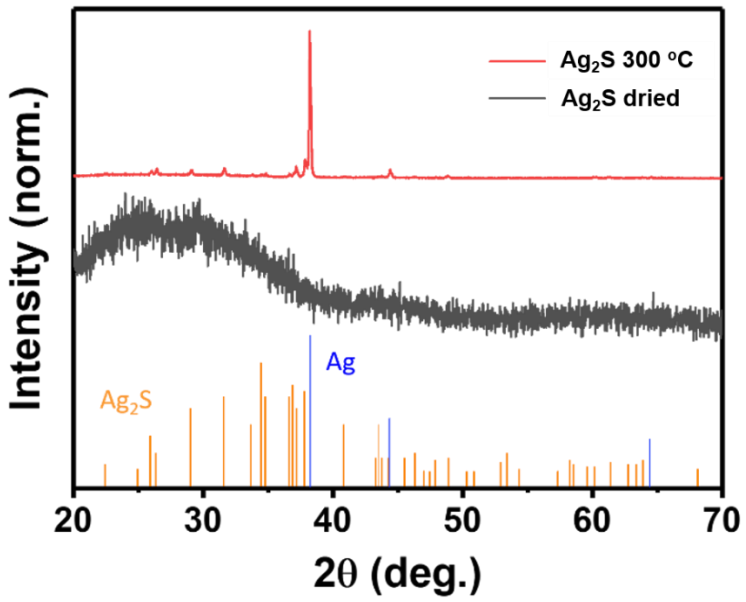

Figure 2.7. XRD patterns of Ag_2S thin films dried and annealed at 300 °C.

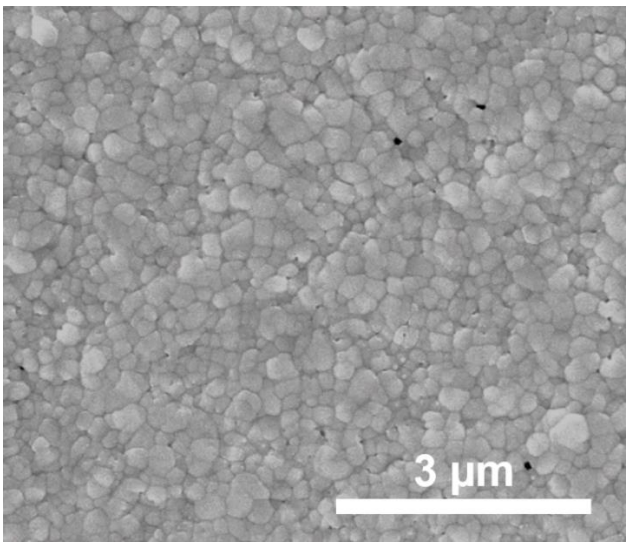

Figure 2.8. SEM image of Ag_2S thin films.

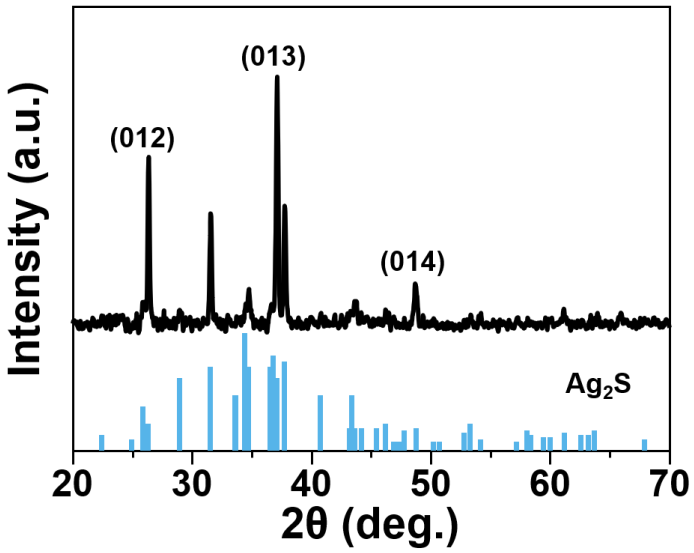

Figure 2.9. XRD pattern of Ag_2S thin film. The vertical lines in the panel indicate the XRD pattern of bulk Ag_2S crystal (JCPDS 00-014-0072).

2.2.2 Mechanical properties of Ag_2S thin films

Figure 2.10a shows the hardness of the Ag_2S films as a function of indentation depth. The hardness was measured at 0.3 (± 0.06) GPa, and elastic modulus of 8.24 (± 0.52) GPa, where which yield strain of 1.2% was estimated by assuming the Tabor's factor of 3 correlating yield stress and hardness. The measured yield strain of Ag_2S thin film was higher than that of about 0.3% for bulk Ag_2S ingot and spark plasma sintering.[22] As the thickness and volume of the material decreases, the number of defects in the material that affect the mechanical properties decreases probabilistically, resulting in higher strength and higher yield strain.[58] This size effect could be a cause for the higher yield strain of the nanoscale Ag_2S thin films.

Uni-axial stretching test were performed to estimate the intrinsic stretchability of Ag_2S thin film. The Ag_2S thin film on thin polyimide substrate was transferred upside down to the stretchable substrate, and upper polyimide was etched with O_2 plasma. It was stretched under observation of optical microscope as shown in **Figure 2.11** and **Figure 2.12**a. Ag_2S thin film on the stretchable substrate showed vertical wrinkles cause by relaxation of the residual stress during transfer process. So, it was stretched up to removing vertical wrinkles first and then stretched again to create cracks on the film. The Ag_2S thin film was stretched up to 14.9 (± 4.7) % without formation of any cracks like typical stretched image (**Figure 2.13**), and primary crack occurred on the side of the film, which is mechanically weak or broken was generated at side of thin film which is mechanically weak or fractured part during transfer process as shown in **Figure 2.12**b. During stretching test, horizontal wrinkles were created on the film as seen in **Figure 2.13**. The compressive stress generated in vertical direction caused horizontal wrinkled structures according to high Poisson's ratio of stretchable substrate. However, stretchability in the stretching direction cannot be mechanically affected and was ignored in this experiment. The stretchability of the Ag_2S thin film on the stretchable substrate was estimated at a tensile strain of 14.9 (± 4.7) % since other parts of the film cannot be stretched with uniform strain after crack propagation. Due to the unique ductile mechanical behavior of bulk Ag_2S with irregularly distributed metal-metal bonding,[22] Ag_2S thin film exhibit high ductility like metals, and transfer process on the stretchable substrate (stretchable tape) can improve fracture strain with high adhesion force between Ag_2S thin film and substrate which could suppress initiation and propagation of cracks in the Ag_2S thin film.

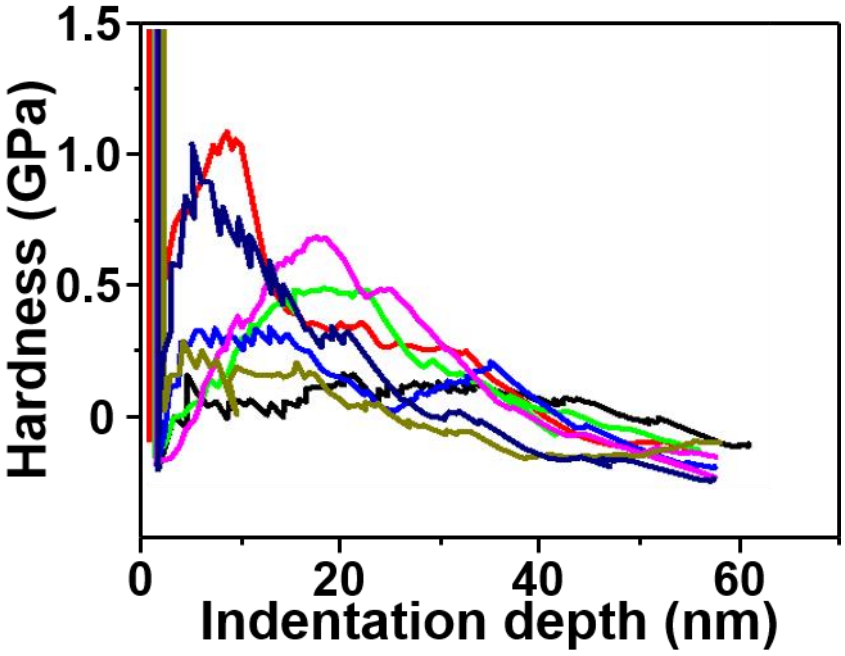

Figure 2.10. Hardness as a function of indentation depth measured by nanoindentation.

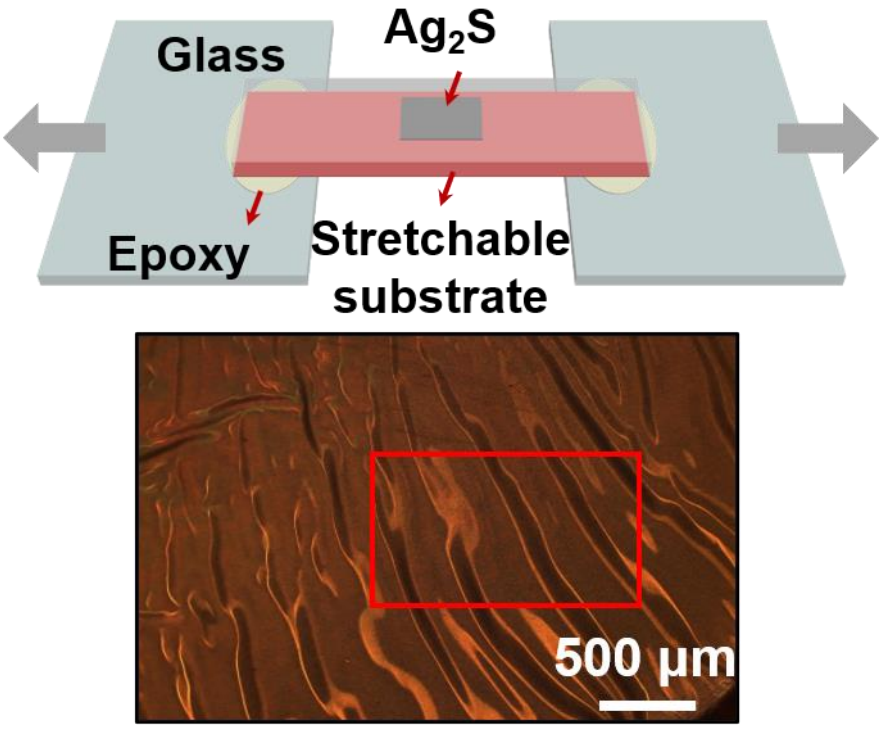

Figure 2.11. Schematic image of stretching test and typical optical microscope image of Ag_2S thin film at initial state (red square was analyzed for stretchability).

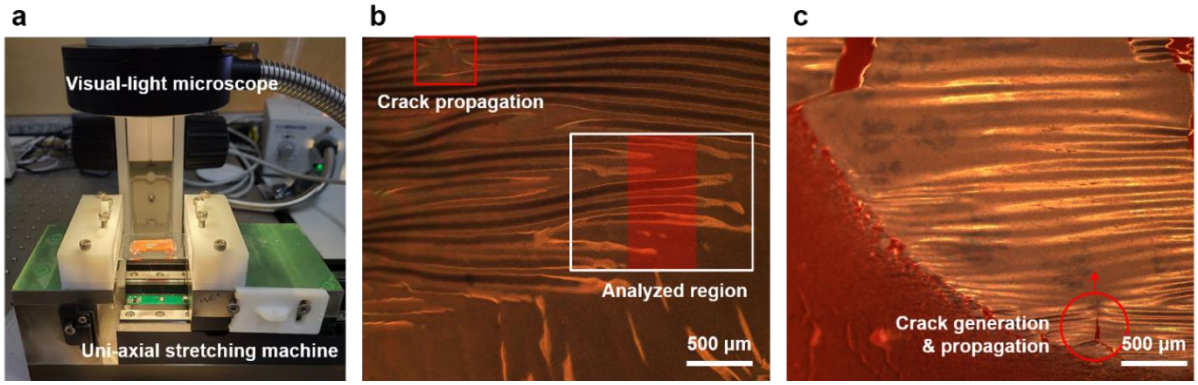

Figure 2.12. a) Photograph of uni-axial stretching machine and optical microscope. Optical microscope images of b) before stretching c) after 14.9% strain.

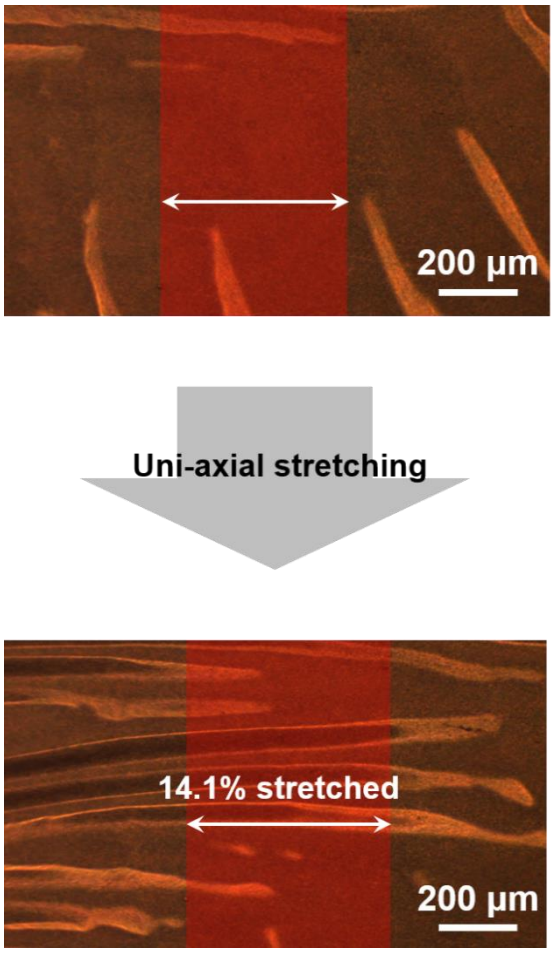

Figure 2.13. Optical microscope image of stretched Ag_2S thin film for tensile strain of 14.1%.

2.2.3 Fabrication of Ag_2S-based RRAMs

The solution process produced the stretchable Ag_2S thin films, allowing the fabrication of Ag_2S thin film-based RRAM arrays on a wafer scale. Initially, Al/Ag_2S/Ag single memory cells were fabricated on polyimide and glass substrates to investigate resistive switching behavior and operational reliability. The Ag_2S active layer was made by spin coating and sandwiched by top (Ag) and bottom (Al) electrodes deposited by thermal evaporation. Each layer showed a uniform thickness of ~100 nm, as shown in the cross-sectional SEM image (**Figure 2.14**). The Al/Ag_2S/Ag RRAM cells on the polyimide substrate showed typical bipolar resistive switching behavior with an I_{on}/I_{off} ratio of ~10^5 (**Figure 2.15**). The initial high resistance state (HRS) was changed to low resistance state (LRS) when sufficient voltage was applied to the device the positive sweep. In contrast, when the negative voltage sweep, the device returned to the HRS below the reset voltage. This resistive changes from the HRS to the LRS and vice versa are utilized for the write and erase operation of the RRAM cell. In addition, the memory cells fabricated on the polyimide, glass, silicon and sapphire substrates showed the identical I–V characteristics with simliar current levels at both the HRS and LRS (**Figure 2.16**).

As shown in **Figure 2.17**. the resistive switching in the Ag_2S-based device resulted from electrochemical metallization and dissolution of Ag ions. During the set process, the Ag_2S layer under the electric field with dissolved Ag^+ cations was passed from the Ag electrode to the opposite Al electrode. The amount of Ag^+ cations reached the Al electrode were decreased, resulting in the Ag filament growing in the direction of Ag electrode. If the Ag filaments were contact between Ag and Al electrodes, the device switched to LRS. Similarly, when sufficiently negative bias was applied, the reset process occurred and annihilated Ag filaments.[22] Ag filament formation in LRS has been further demonstrated by conductive atomic force microscopy (C-AFM) analysis. The C-AFM images shows the appearance of conductive channels in the Ag_2S thin film of LRS (**Figure 2.18**), but no channels were observed in the film of HRS (**Figure 2.19**) and the appearance of these conducting filaments should be generated from the formation of the Ag filaments. The nonuniformity of the Ag filaments can be due to small grain sizes and surface roughness, as local electric field can be strongly affected by the local variability of crystallographic orientations and thickness. I also measured the temperature-dependent resistivity of Ag_2S-based RRAM at a low resistance state (LRS). As the temperature increase from 30 ^oC to 130 ^oC, the resistivity of Ag_2S-based RRAM increased almost linearly (**Figure 2.20**). This positive temperature dependence of the resistivity is the typical metallic behavior due to the increased thermal motion of the atoms on lattice sites. The increase in motion serves as center of scattering of electrons and reducing their mean free path, leading to an increase in resistivity. This result shows that the resistive switching mechanism in the Ag_2S thin film originated from the formation and annihilation of Ag filaments.

To further demonstrate the reliability of the Al/Ag_2S/Ag RRAM cell, retention and endurance tests during the repetitive switching. The Al/Ag_2S/Ag RRAM cell showed excellent retention properties for both the HRS and LRS up to 10^6 s with no significant variation in the I_{on} and I_{off} values (**Figure 2.21**). Moreover, to confirm the long-term retention of our RRAM, I conducted the retention test for 14 days. As shown in **Figure 2.22**, Ag_2S-based RRAM demonstrated excellent retention that maintained the memory states over 14 days without degradation in both LRS and HRS. The memory cell also showed highly reproducible operation for 100 times (**Figure 2.23**). Finally, the distribution of the set and reset voltage is almost uniform, and the average values of ~500 mV, indicating the reproducibility of the memory cells. This is an advantage in terms of power consumption during device operation (**Figure 2.24**).

Solution-processed fabrication of thin films is beneficial for achieving the large-scale, cost-effective fabrication of thin film devices. The process introduced here resulted in the manufacture of the wafer-scale fabrication of an Ag_2S-based RRAM (**Figure 2.25**). The solution-processed Ag_2S thin film deposited on a 4-inch wafer showed uniform microstructures throughout the region as shown in SEM images (**Figure 2.26**). In addition, to check the practicality of the Ag_2S thin film as a wafer-scale active layer, I investigated the operational uniformity by measuring the I–V characteristics of the RRAM cells at each point presented in **Figure 2.27**. Each cell demonstrated bipolar switching behavior with a uniform distribution of I_{on}/I_{off} ratios and set/reset voltages (**Figure 2.28**). This reliable resistive switching behavior of the RRAM cells on a wafer-scale suggests that the solution processing of Ag_2S thin films can be used for the fabrication of high-density integration of RRAM arrays.

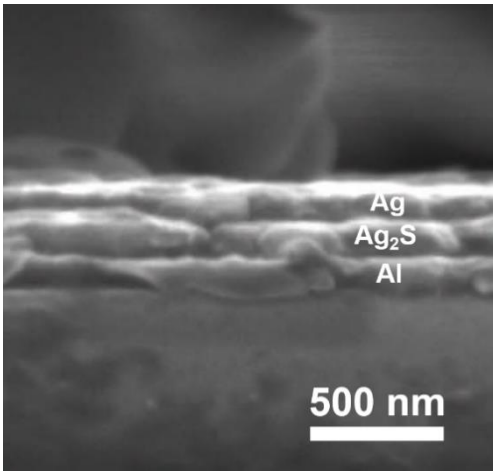

Figure 2.14. Cross-sectional SEM image of Al/Ag_2S/Ag RRAM.

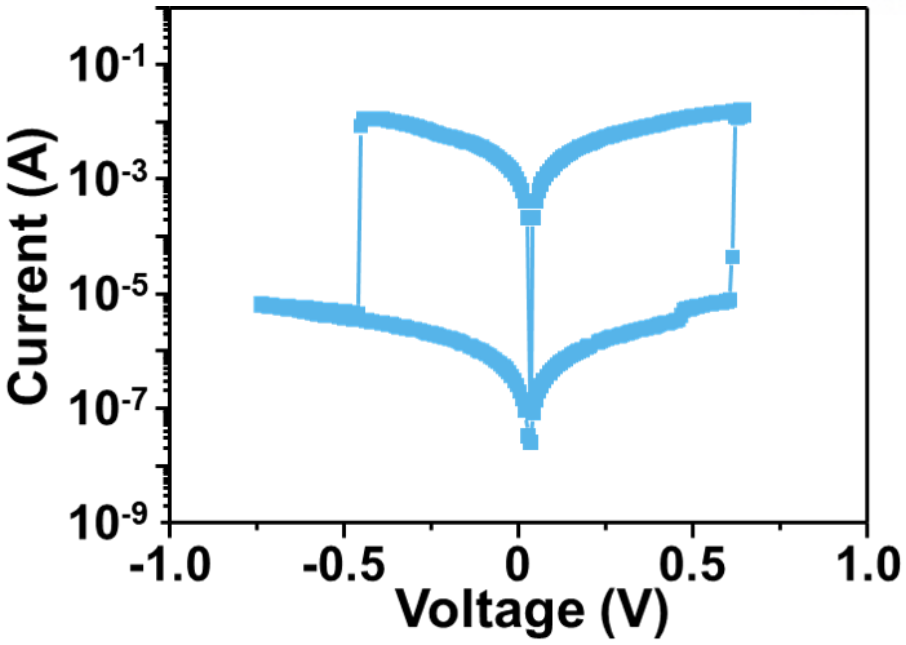

Figure 2.15. *I-V* characteristic for the Al/Ag_2S/Ag memory cell.

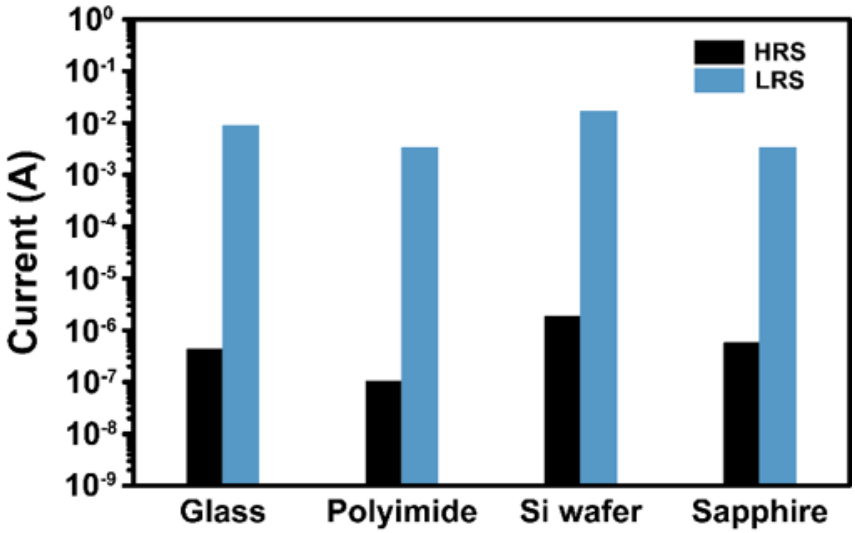

Figure 2.16. I_{on} and I_{off} of Al/Ag_2S/Ag memory cell fabricated on glass polyimide, silicon and sapphire substrates.

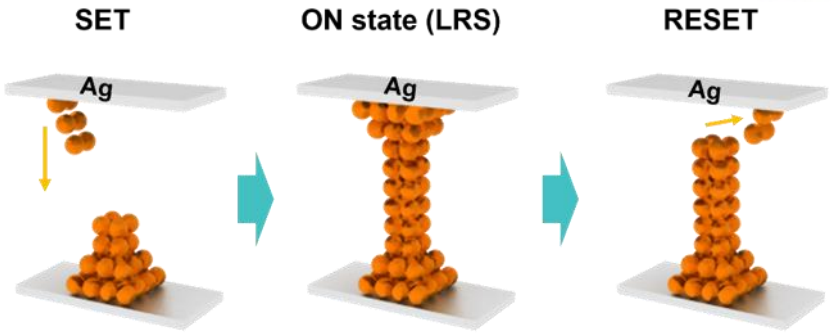

Figure 2.17. Schematic illustration of the switching mechanism for the operation of the Al/Ag_2S/Ag RRAM.

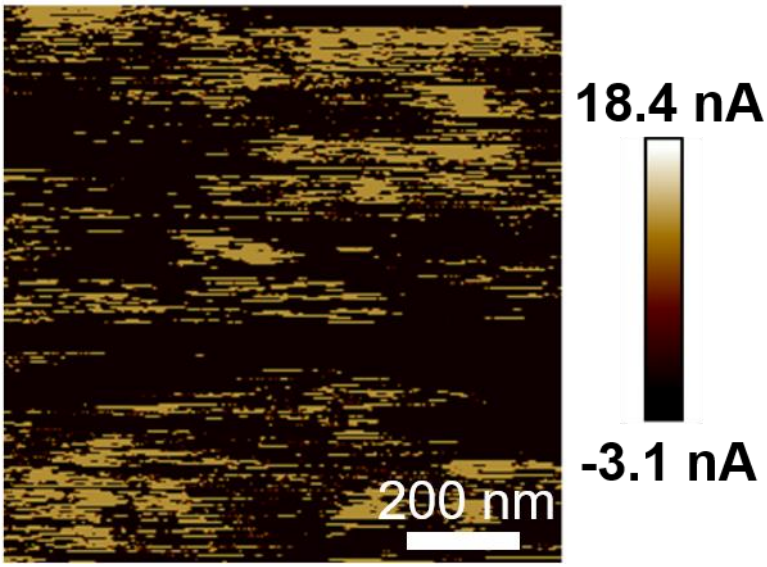

Figure 2.18. C-AFM analyses for the Al/Ag_2S/Ag memory cell at LRS.

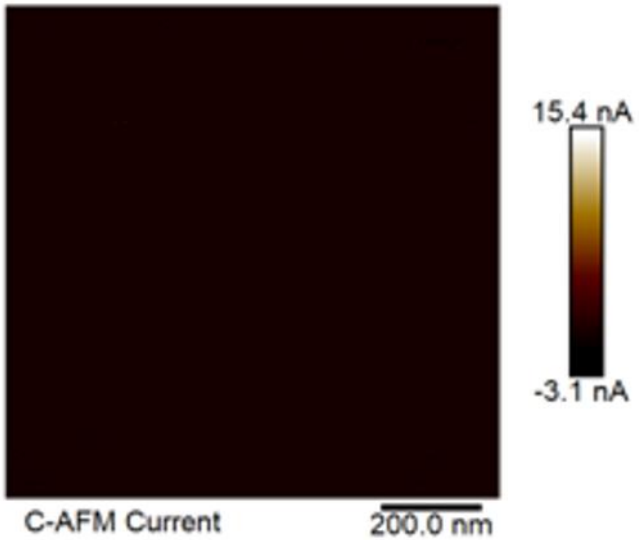

Figure 2.19. C-AFM analyses for the Al/Ag_2S/Ag memory cell at HRS.

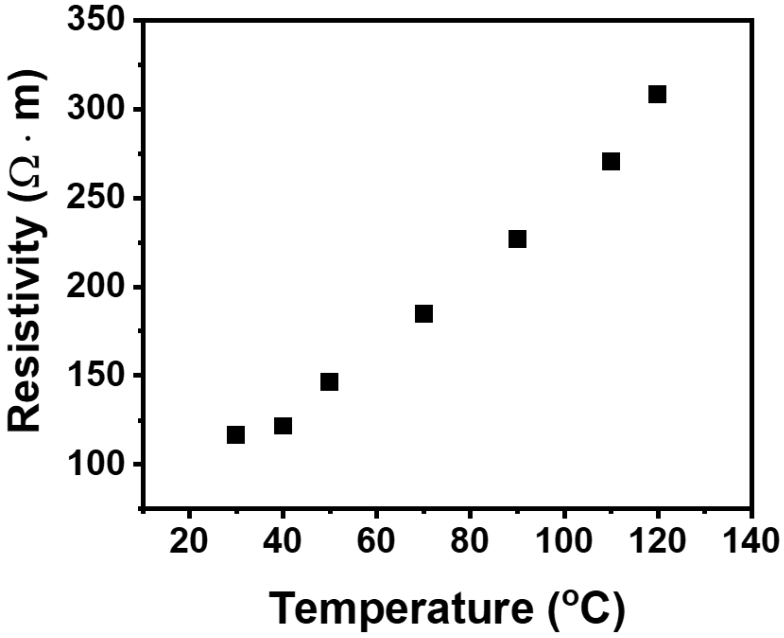

Figure 2.20. Temperature dependence of the electrical resistivity of the Ag_2S-based RRAM at the LRS.

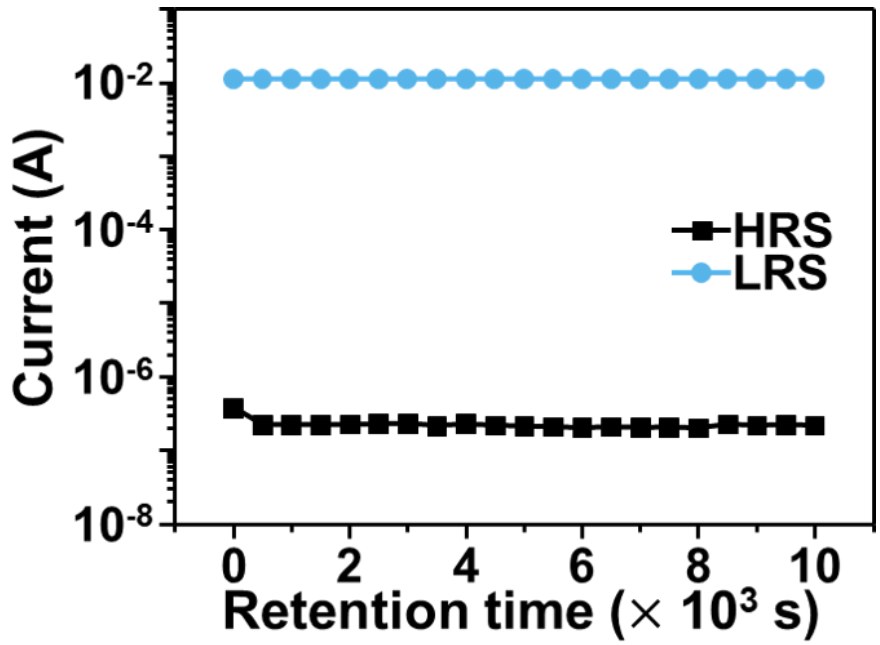

Figure 2.21. Retention time for the Al/Ag_2S/Ag memory cell.

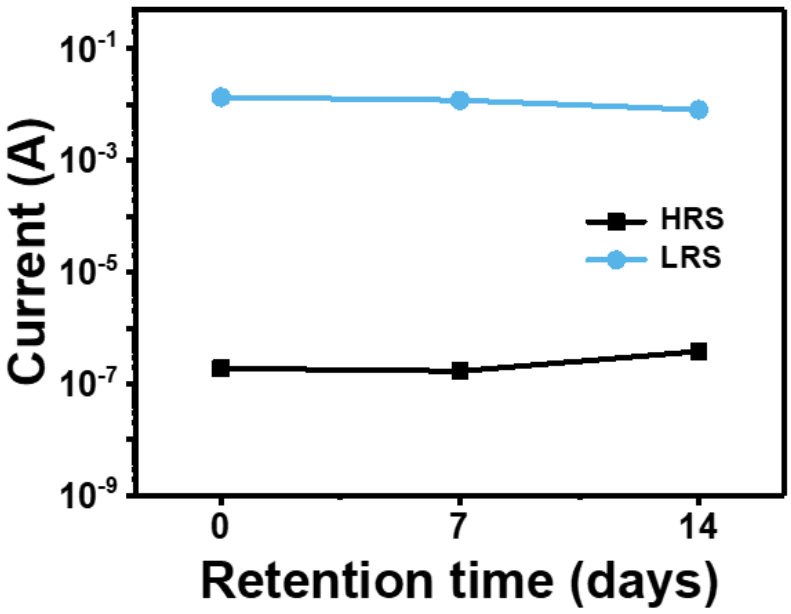

Figure 2.22. Long-term retention property of Ag_2S-based RRAM.

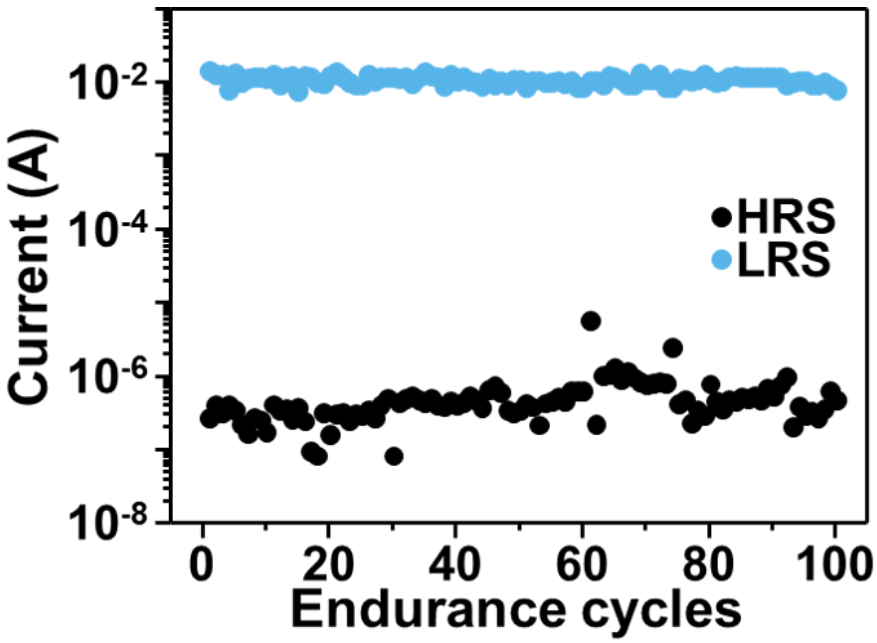

Figure 2.23. Endurance cycles for the Al/Ag_2S/Ag memory cell.

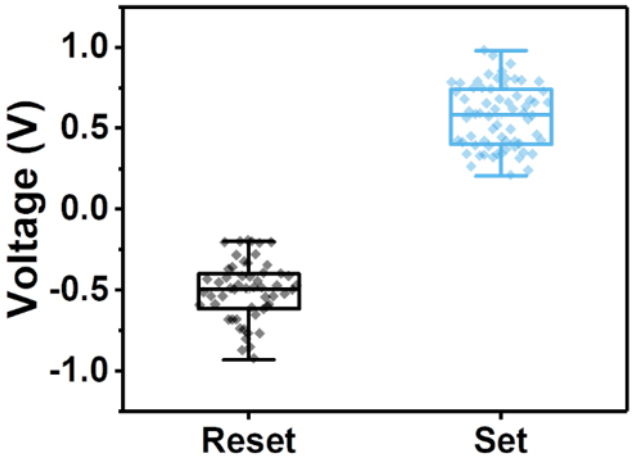

Figure 2.24. Set and reset voltage distributions of Al/Ag_2S/Ag single memory cell.

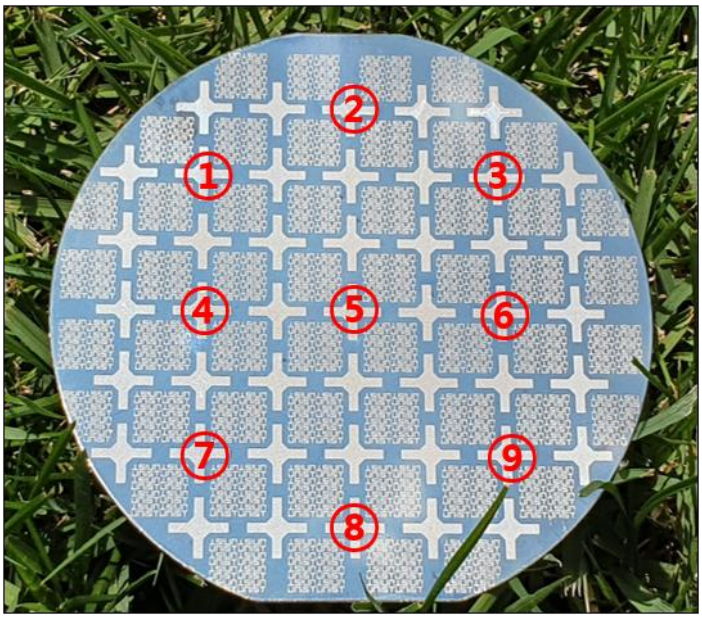

Figure 2.25. Photograph of Ag_2S-based RRAM fabricated on a 4-inch wafer.

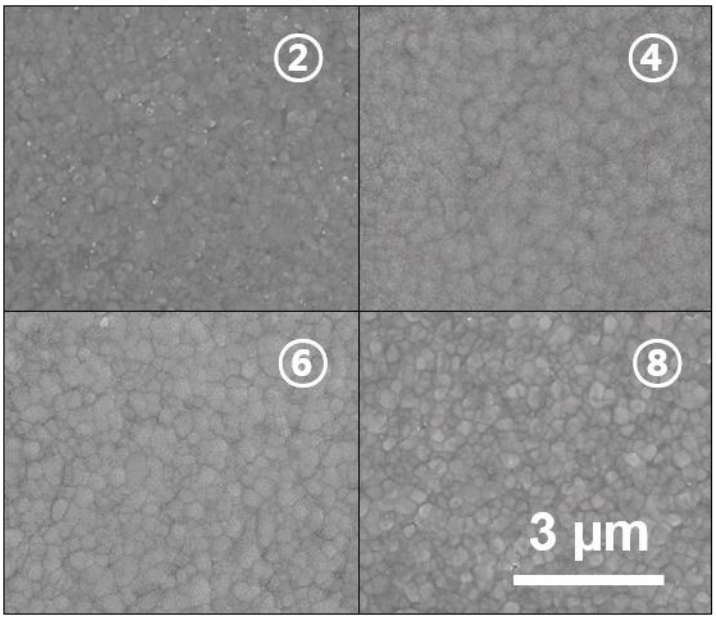

Figure 2.26. SEM images of Ag_2S layer at no. 2, 4, 6, and 8 marked in panel.

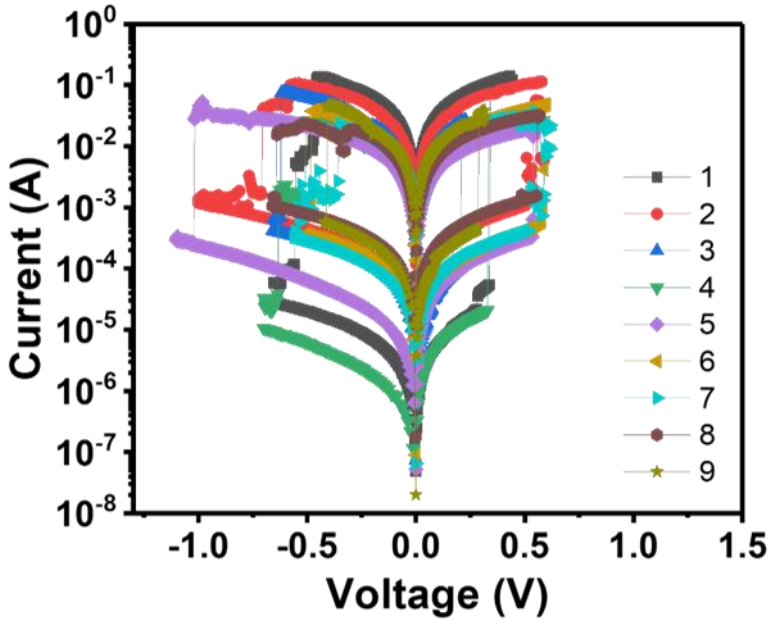

Figure 2.27. *I-V* characteristics at each cell of Ag_2S-based RRAM fabricated on 4-inch wafer.

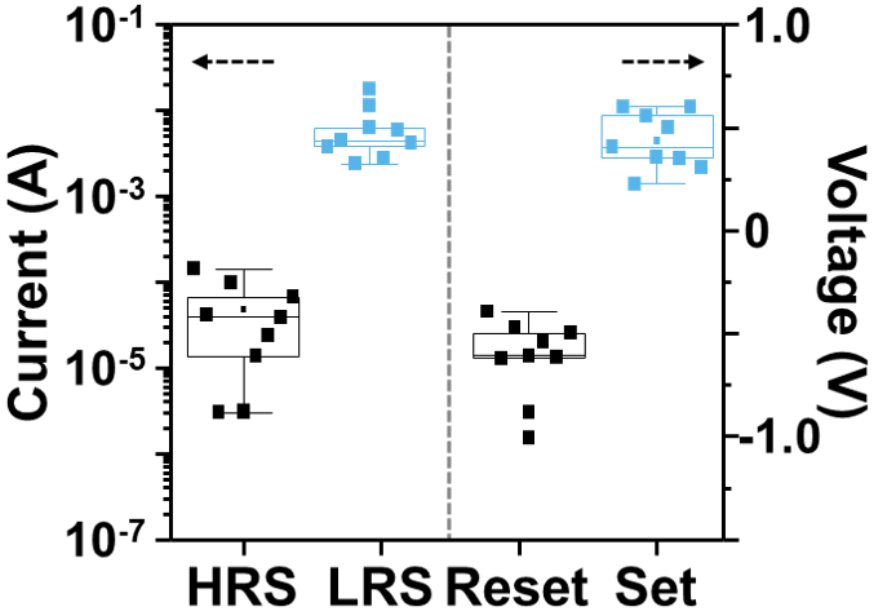

Figure 2.28. I_{on}, I_{off}, and set/reset voltage distributions of Ag_2S-based RRAM fabricated on a 4-inch wafer.

2.2.4 Environmental durability of Ag_2S-based RRAMs

Compared with organic-based devices, inorganic semiconductors are inherently resistant to degradation due to chemical and thermal stress. To evaluate durability, I conducted an accelerated stress tests with 85 °C/85% relative humidity (85/85 test) was performed with Ag_2S RRAMs without any encapsulation. The RRAMs shows no degradation of switching properties for 168 h (**Figure 2.29**). Moreover, the chemical stability of the Al/Ag_2S/Ag RRAM cell was further investigated by immersing the device in a variety of solvents representing hydrophilic, hydrophobic, and salt conditions, such as hydrophilic deionized (DI) water, phosphate buffer saline (PBS) and eight different kinds of organic solvents for 10 min (**Figure 2.30**). To check the thermal stability, the Ag_2S-based RRAM cell was operated under the thermal stresses for 10 min in a wide temperature range from −196 to 300 °C. Surprisingly, in all cases, the RRAM cell exhibited almost the same *I*−*V* characteristics before and after the chemical and thermal stresses (**Figure 2.31 and 2.32**). Given that reported organic-based stretchable electronics are usually encapsulated for sustainable operation,[59-62] these results observed in the Ag_2S-based RRAMs clearly demonstrated extraordinary durability under harsh environments, validating the ubiquitous applicability.

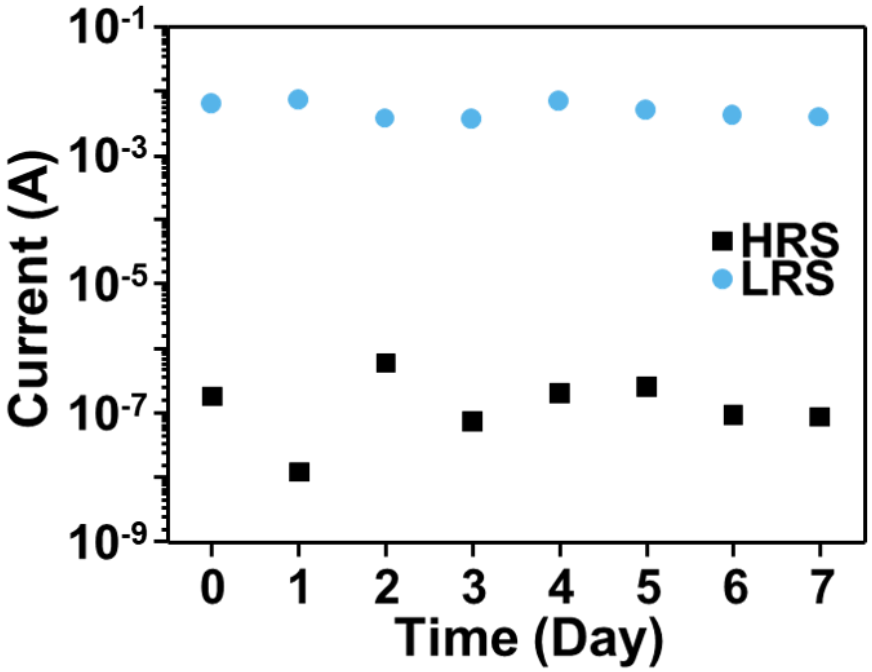

Figure 2.29. Accelerated stress tests under 85°C/85% relative humidity. All read operations were conducted at 0.03 V.

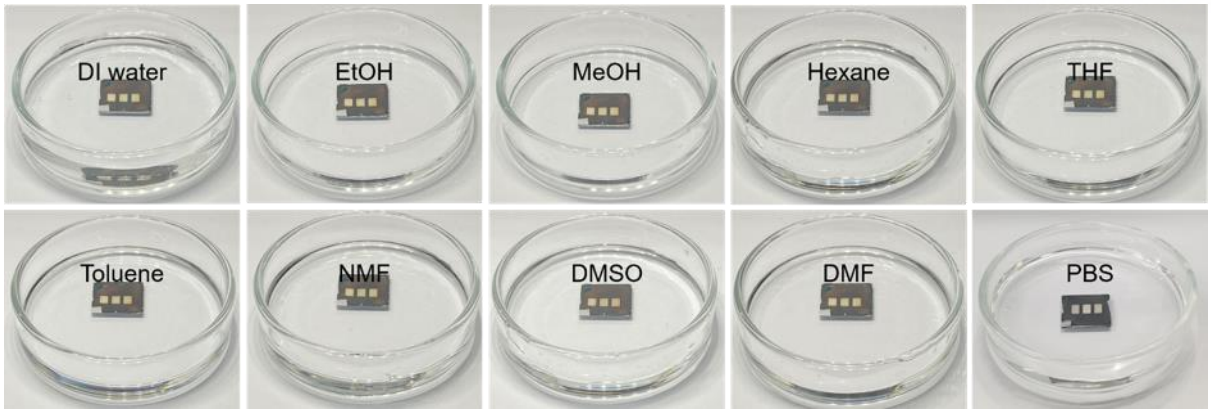

Figure 2.30. The photographs of Al/Ag_2S/Ag RRAM immersed in diverse chemical environments.

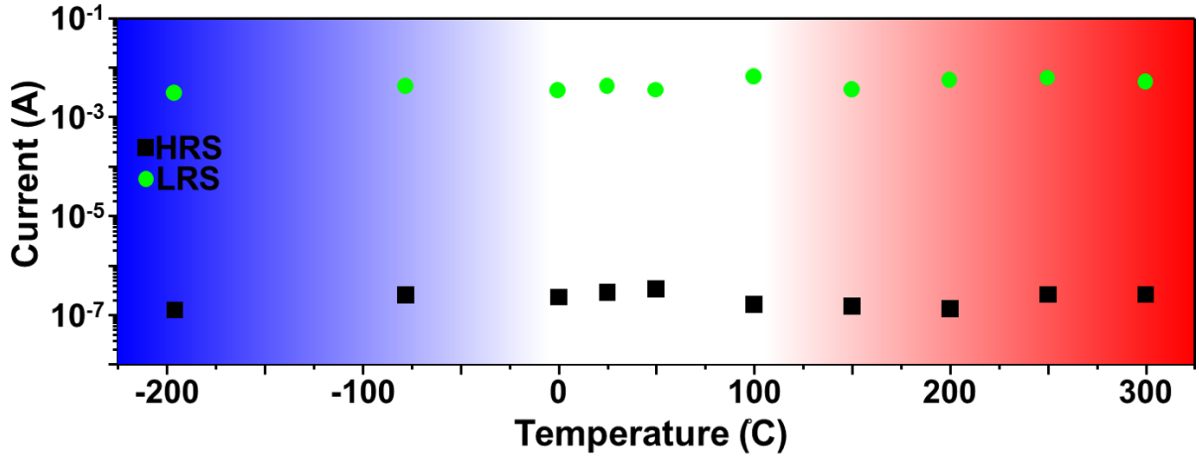

Figure 2.31. Thermal stabilities of Ag_2S-based RRAM. All read operations were conducted at 0.03 V.

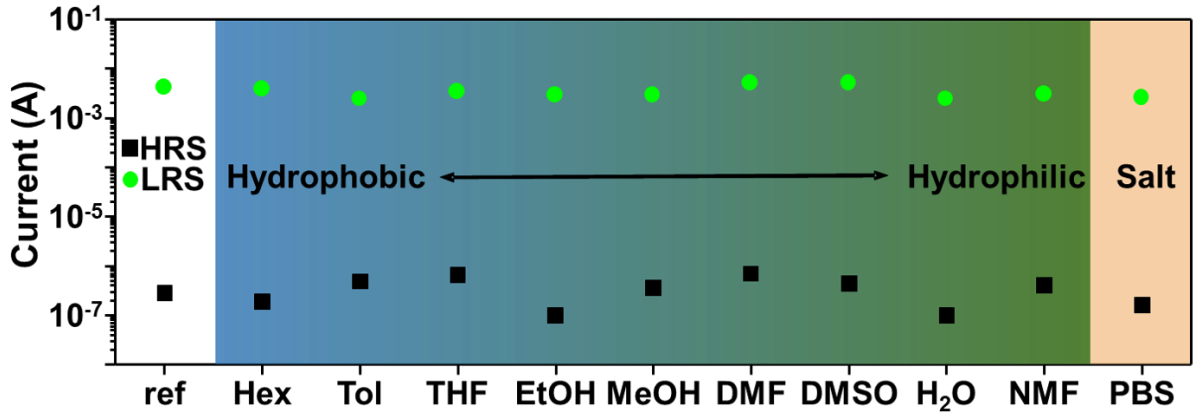

Figure 2.32. Chemical stabilities of Ag_2S-based RRAM. All read operations were conducted at 0.03 V.

2.2.5 Stretchable Ag_2S-based RRAMs

The intrinsic stretchability of the α-Ag_2S thin films made it possible to fabricate highly stretchable wrinkled Ag_2S thin film layers without any mechanical failure. This wrinkled thin film-based stretchable RRAM was fabricated by transferring the Ag_2S-based RRAM on the thin polyimide onto a pre-stretched rubber substrate using water soluble tape (**Figure 2.33**). The ultrathin form of the RRAM (~3 μm total thickness; **Figure 2.33**) allowed high deformability, including bending, stretching, and twisting. The ~300 nm thick RRAM was located near the neutral mechanical plane between the ~1.4 μm thick polyimide encapsulation layer, which effectively minimized the induced strain on the α-Ag_2S active layer. As the tensile strain of the rubber substrate was released, the RRAM wrinkled, allowing for a reversible deformation from 0% to 52% strain (**Figure 2.34**). I further carried out the XRD characterization to check if there are any differences in the crystallographic phase after the lithography and transfer processes. As shown in **Figure 2.35**, the peaks in the XRD patterns of the Ag_2S thin films after lithography and transfer processes are well matched with those of pristine Ag_2S thin films deposited on glass substrate. Meanwhile, I found that there is a slight difference in crystallographic orientation of Ag_2S thin film after the device fabrication process. This could be attributed to the wrinkled surface of Ag_2S thin film on polyimide substrate rather than lithography and transfer process.

To investigate the maximum stretchability of the Ag_2S layer in the stretchable RRAM, I carried out finite element analysis (FEA) simulations based on the measured mechanical properties. According to fabrication process of stretchable RRAM, wrinkle formation process was simulated for analyzing stress and strain distribution on the Ag_2S thin film. Perfect plasticity of the Ag_2S thin film was assumed in the simulations. As shown in **Figure 2.36**, flat Ag_2S thin film was compressed and wavy structure was formed at the surface by elastic recovery of pre-strained substrate. According to the release of pre-strained substrate, the radius of curvature decreases hundreds of micrometers to tens of micrometers as shown in **Figure 2.37**. The stretchable RRAM shows tens of micrometer radius of curvature, so pre-strain should be released to form wavy structure at the stretchable substrate up to 40% by the simulations. The 40% released Ag_2S thin film shows identical feature shape comparing with surface profile presented in **Figure 2.38**. The simulated feature has a wavelength of 500 μm and an amplitude of 150 μm which are very similar dimensions to actual wrinkle structure of the stretchable RRAM. As the radius of curvature decreases, stress and strain also tends to concentrate more at the center of wavelength like actual profile of the device. During stretching RRAM, wrinkled device releases structural stretchability and ductile Ag_2S provides additional stretchability. Based on these results, total stretchability of 52% for the devices can be realized by combination of unfolding the wrinkled structure and intrinsic fracture strain of the Ag_2S thin films.

The flexibility of the Al/Ag_2S/Ag RRAM device fabricated on a polyimide substrate was evaluated by measuring I_{on} and I_{off} every 100 bending cycles at a bending radius of ~1.9 mm (**Figure 2.39**). The

Ag_2S-based RRAM fabricated on flexible substrates clearly exhibits the typical bipolar resistive switching behavior with I_{on}/I_{off} ratio of ~10^5 (**Figure 2.40**), agreeing with those of the RRAM fabricated on rigid substrates such as a glass. The device showed a reproducible I_{on}/I_{off} ratio with negligible variation during 1000 bending cycles. Moreover, by introducing wrinkled structure to the 3-μm-thick Al/Ag_2S/Ag RRAM, effective level of stretchability was provided under 0%–52% strain. From the 3D optical profile images (**Figure 2.38**), the radius of curvature of the wrinkled RRAM ranged from tens of micrometer to several millimeters. When external tension was applied, the wrinkled RRAM was stretched to 52% by relieving the internal stress, and exhibited stable I_{on} and I_{off} characteristics (**Figure 2.41**). Moreover, any cracks were not observed in the SEM images of the transferred Ag_2S, Ag, and Al thin film under the both wrinkled and stretched state (**Figure 2.42**). The stretching cycle test was performed under 30% strain and both I_{on} and I_{off} exhibited negligible variation during 1000 stretching cycles (**Figure 2.43**). These results clearly demonstrate the applicability of ductile Ag_2S semiconductor thin films for stretchable electronics. Considering that the reported metal oxide-based RRAMs demonstrated mechanical endurance tests at a bending radius of 4−30 mm,[63-65] the Al/Ag_2S/Ag RRAM could be evaluated to have an extraordinary mechanical durability. Further, I investigated the benchmark papers of flexible and stretchable inorganic- and organic-based RRAMs in the literature (**Table 2.1**), showing the superior device performance and mechanical stretchability of our device.

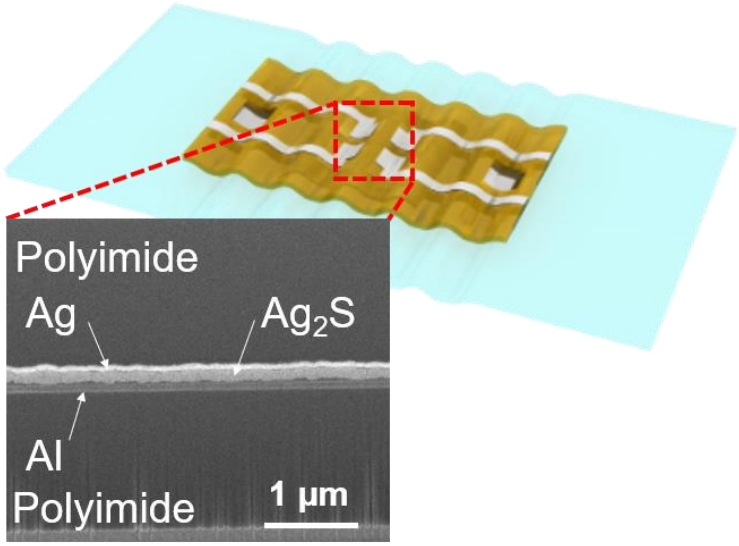

Figure 2.33. Schematic illustration focused ion-beam (FIB) cross-section image of the Ag_2S-based stretchable RRAM.

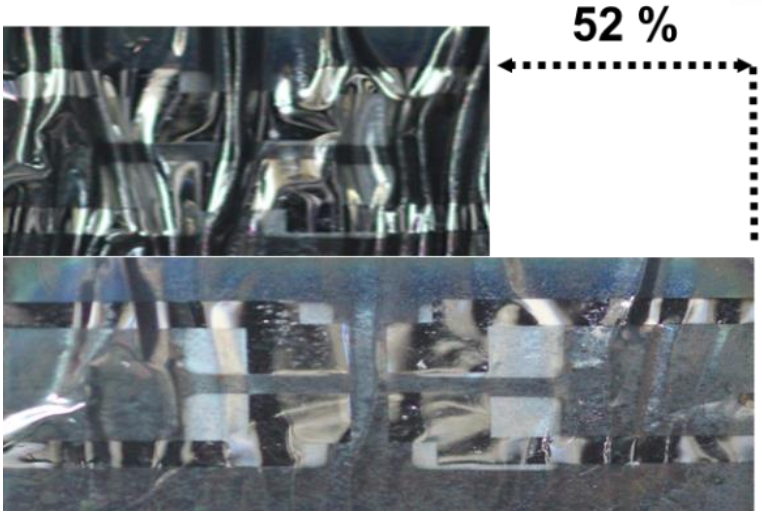

Figure 2.34. Photograph showing the stretchable RRAM at wrinkled (0% strain) and fully stretched states (52% strain).

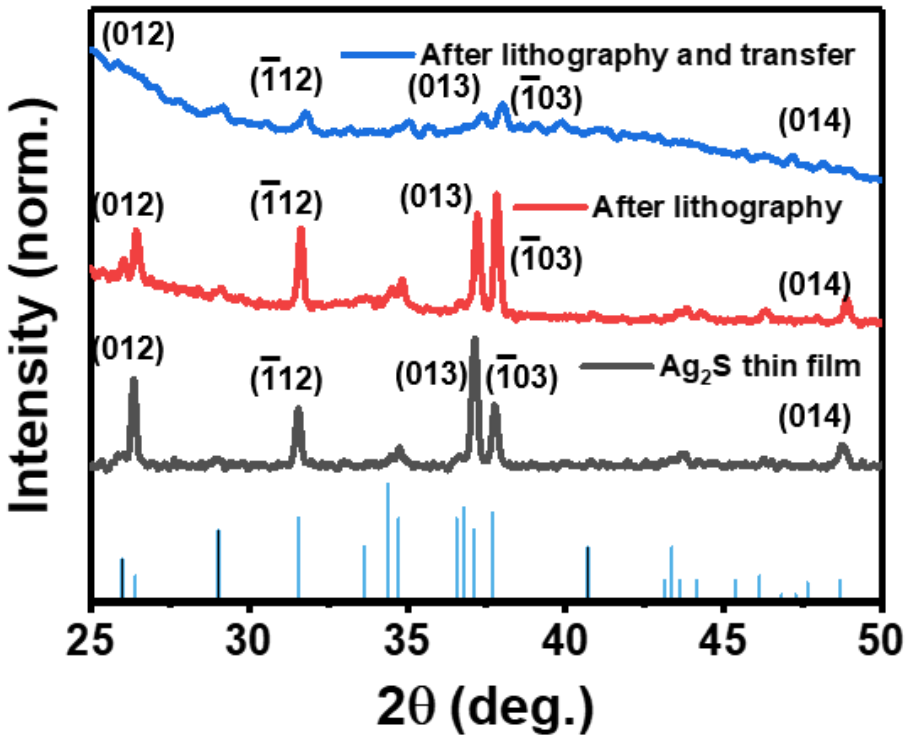

Figure 2.35. XRD patterns of Ag_2S thin films before and after lithography and transfer processes.

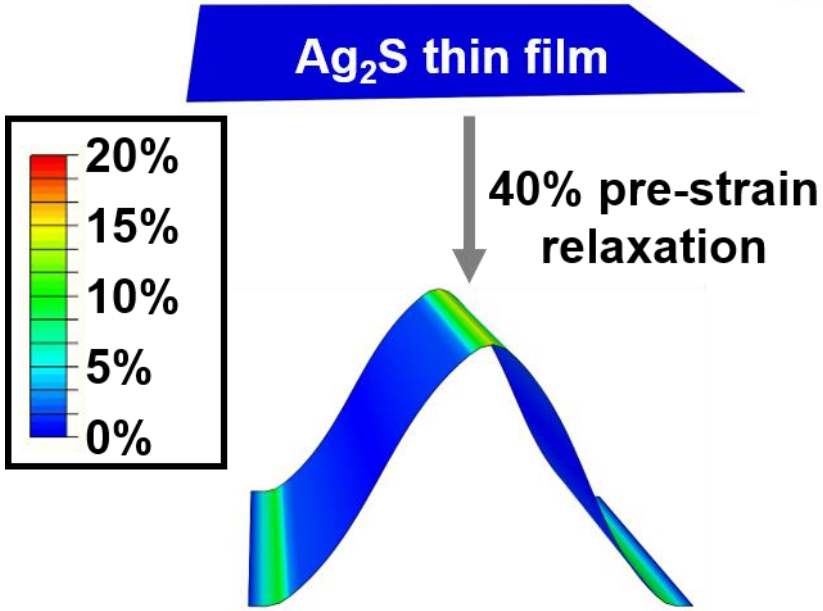

Figure 2.36. 3D FEA simulation result of wrinkle formation at stretchable RRAM.

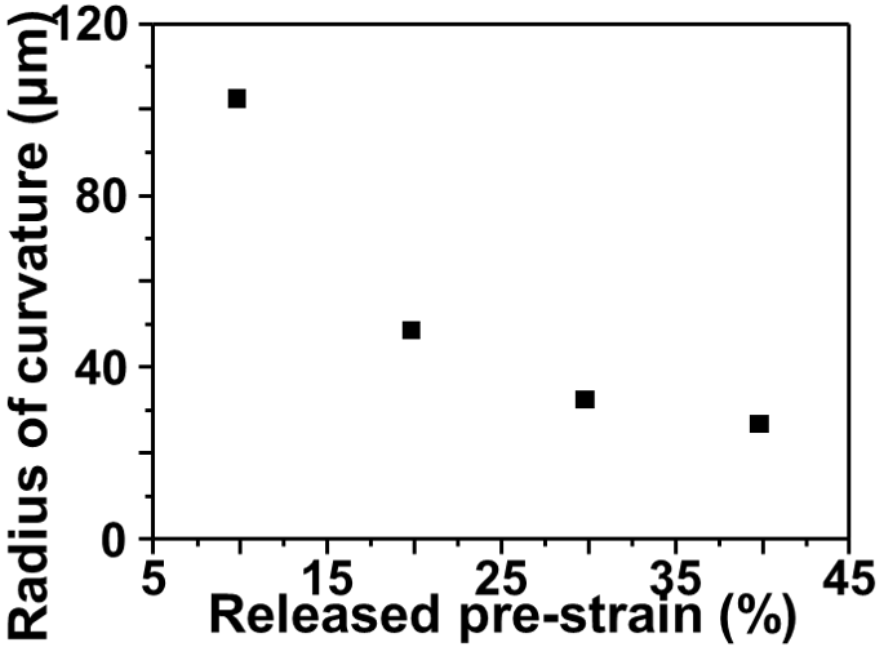

Figure 2.37. Radius of curvature of Ag_2S thin film depending on released pre-strain of substrate.

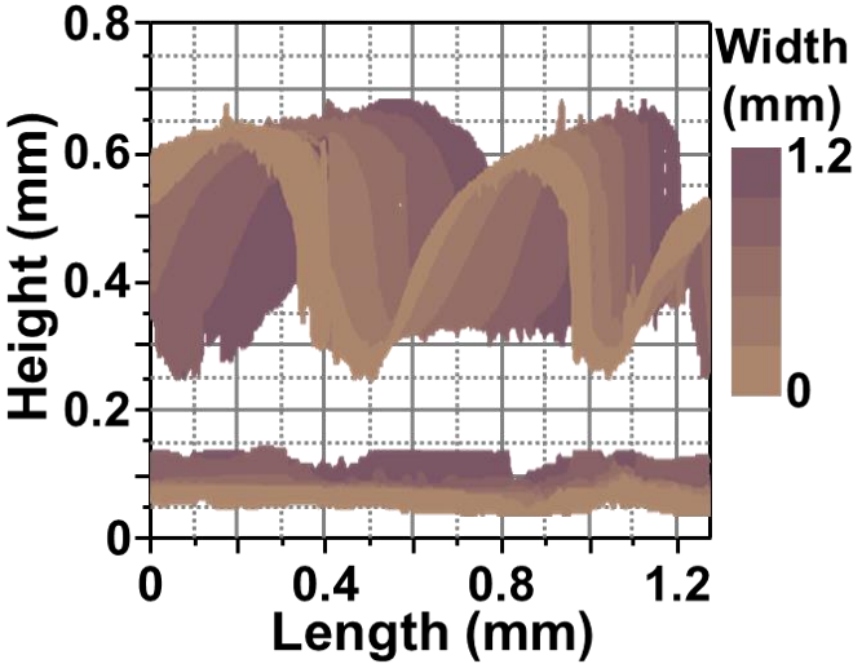

Figure 2.38. 3D surface scanning (1.28 mm × 1.28 mm) of the wrinkled and stretched surfaces of the stretchable RRAM.

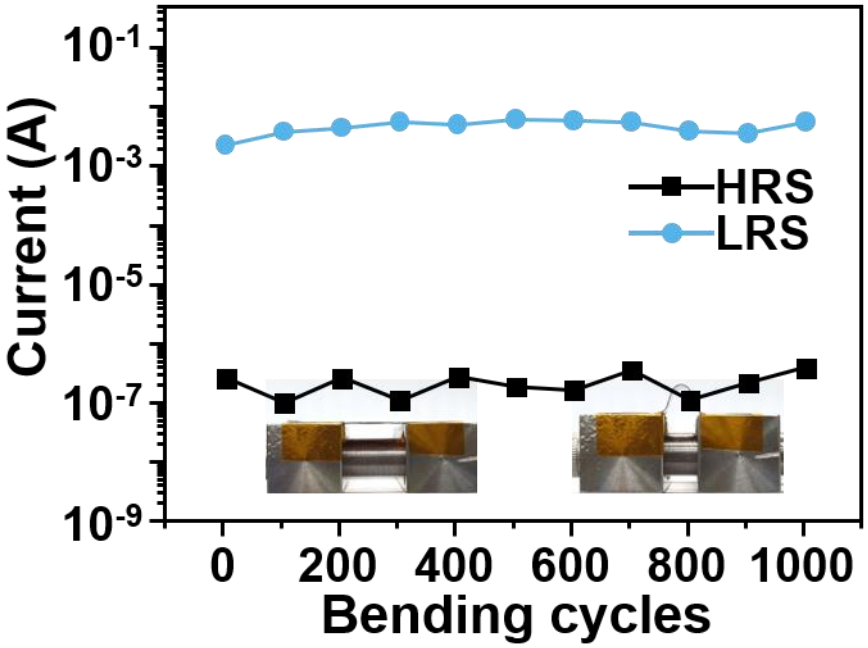

Figure 2.39. I_{on} and I_{off} distribution during 1000 bending cycles at a bending radius of ~1.9 mm.

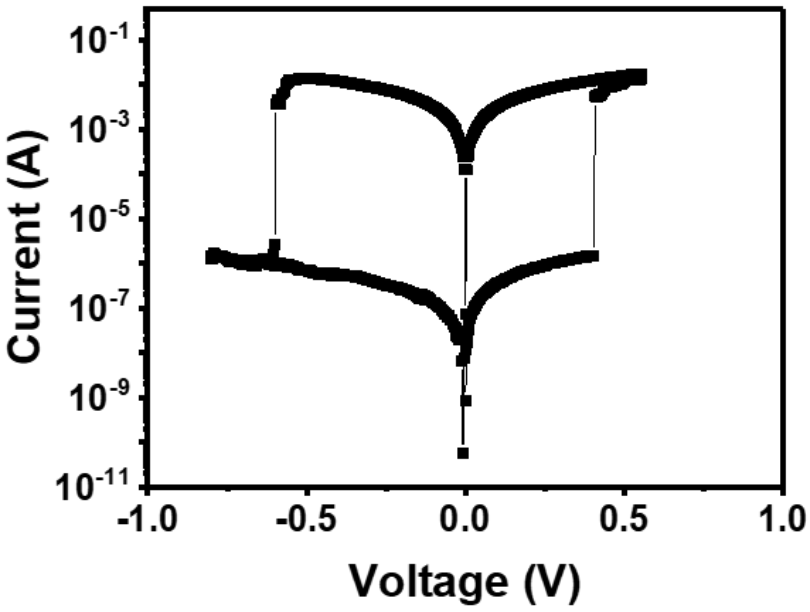

Figure 2.40. *I*−*V* characteristic of the Ag_2S-based RRAM fabricated on a polyimide substrate.

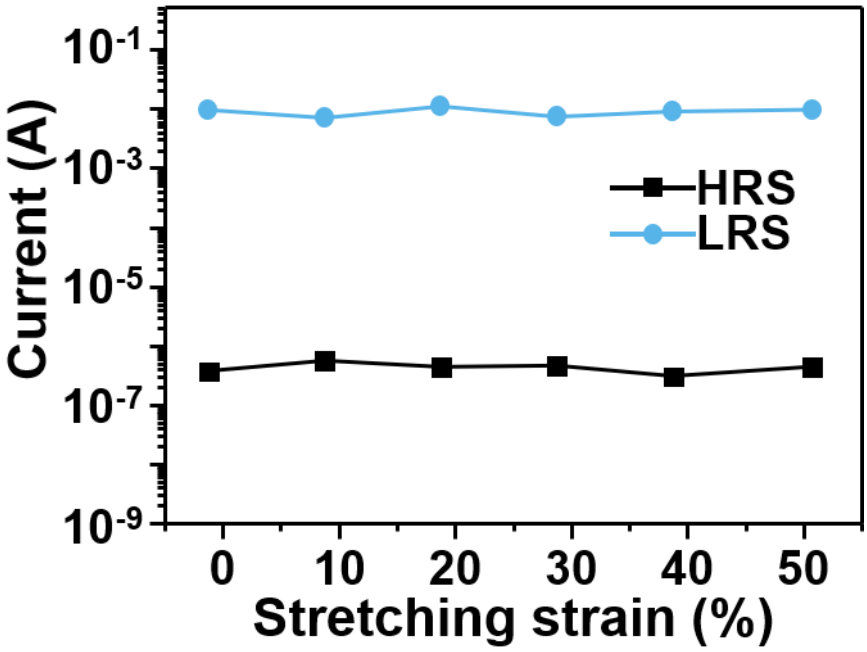

Figure 2.41. I_{on} and I_{off} distribution during stretching strain from 0 to 52%.

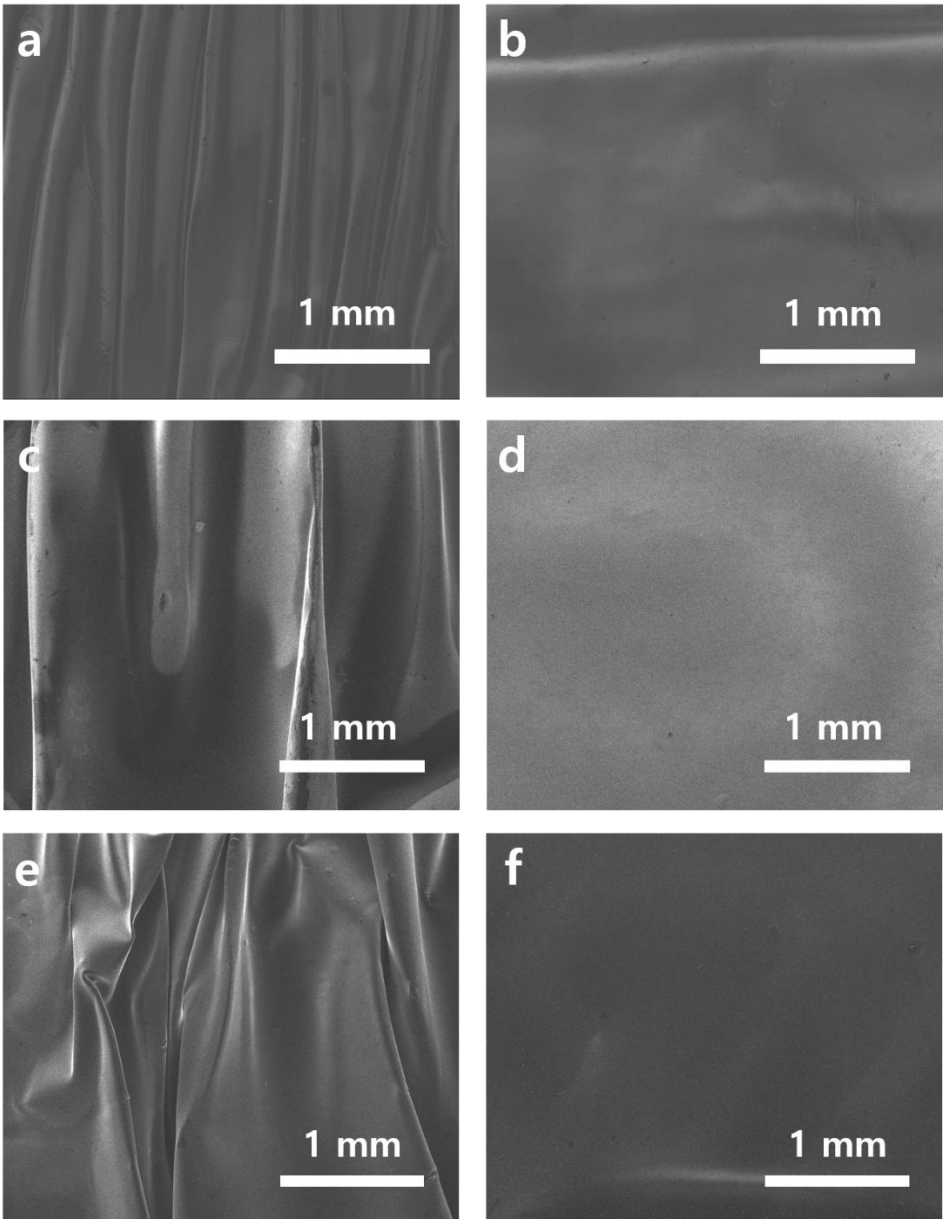

Figure 2.42. SEM images of a,b) Ag_2S, c,d) Ag and e,f) Al thin films under a,c,e) the wrinkled and b,d,f) stretched state.

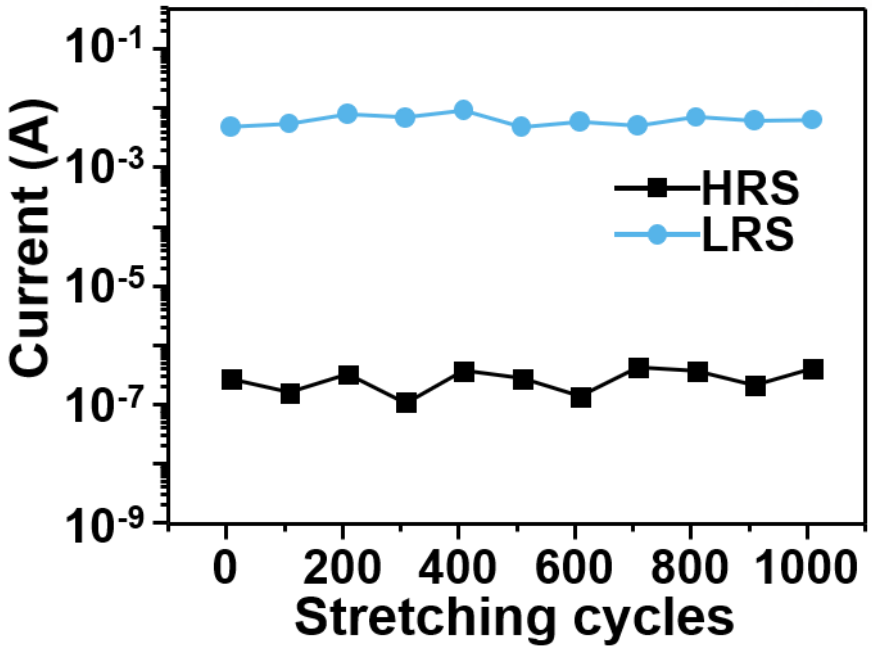

Figure 2.43. I_{on} and I_{off} distribution during 1000 stretching cycles at a stretching strain of 30%.

Table 1. The state-of-the-art flexible RRAMs published recently.

Materials	Fabrication process	Switching mechanism	I_{on}/I_{off} ratio	Retention time [sec]	Endurance cycles	Bending cycles (Bending radius)	Stretching cycles (Strain)	Ref.
TiO_2	Atomic layer deposition	Filament formation	$10–10^2$	10^4	10^2	10^3 (10 mm)	-	66
WO_{3-x}	Sputtering	Filament formation	$\sim10^5$	$5x10^5$	10^3	10^3 (5.53 mm)	-	67
InGaZnO	Sputtering	Filament formation	$10^2–10^3$	-	150	10^4 (8 mm)	-	68
Graphene oxide	Spin casting	Interface-based switching	$\sim10^2$	10^5	10^2	10^3 (9 mm)	-	69
GeO_x/HfON	Sputtering	Hopping conduction	$10^2–10^3$	10^4	10^5	10^4 (15 mm)	-	70
Ag_2Se	Spin coating	Filament formation	30	10^5	10^4	-	-	71
Cu_3(benzene-1,3,5-tricarboxylic acid)$_2$	Liquid phase epitaxy	Filament formation	$10–10^2$	10^4	10^7	160 (4.5 mm)	160 (2.0%)	72
$CH_3NH_3PBI_3$	Thermal evaporation	Interface-based switching	10^3	10^4	10^3	200 (3 mm)	-	73
MIL-53	Solution-immersion	Filament formation	$\sim10^2$	10^4	200	-	50 (10%)	74
HfO_x	Sputtering	Filament formation	$10^2–10^3$	10^5	10^8	1200 (6 mm)	-	75
Zeolitic imidazolate framework-8	Solution-immersion	Hopping conduction	$\sim10^9$	$3x10^3$	25	-	10^3 (50%)	76
Ag_2S	Spin coating	Filament formation	$\sim10^5$	10^4	10^2	10^3 (1.9 mm)	10^3 (30%)	This work

2.2.6 Self-powered Ag_2S-based RRAMs for wearable healthcare monitoring system

Recently, electronic systems that integrate RRAM and pressure sensors are focused on advances in next-generation bio-inspired haptic systems and neuromorphic electronics with low energy consumption, synaptic data processing, and wearable healthcare monitoring systems multifunctionality. External power supplies in ultrathin/stretchable forms are required to store the bio-signal data measured by the wearable sensors into the memory devices. Moreover, the currently developed Ag_2S RRAM with high durability are quite advantageous for designing 24 h-healthcare monitoring system for patients in a real life. Accordingly, I designed an integrated motion sensor/stretchable RRAM for a self-powered healthcare monitoring system for monitoring patients with Parkinson's disease, a degenerative brain disease (**Figure 2.44**). Patients with Parkinson's disease exhibit unintentional and irregular body tremors and muscle stiffness, which can lead to frequent falls and injuries. Therefore, there is a demand for a wearable electronic system capable of distinguishing among conventional motion (e.g. walking), irregular tremors, and collisions by external impacts. The basic operational mechanism in triboelectric pressure sensor under human motion was illustrated in **Figure 2.45.** An alternating AC signal was generated by the pressure sensors under external pressure or deformation and converted to a DC signal via an external circuit consisting of a bridge rectifier **Figure 2.46**. For the energy conversion, different capacitors (10 nF and 1 nF) were placed in the circuit to control the output open circuit voltage (V_{oc}) to the Ag_2S memory device (**Figure 2.47**). In our system, the Ag_2S RRAM cells in the low-resistance region were switched from HRS using a 0.5 V external bias. Different mode of motion (instantaneous external impacts and human motion) was measured by the motion sensors; the open circuit voltage from the motion sensor ($V_{oc}^{\text{Human motion}}$) under an external impact was 40 V and $V_{oc}^{\text{Human motion}}$ under normal behavior (Walking) and tremor was ~2 V and ~3V respectively (**Figure 2.48**). The input voltage to the RRAM cell was controlled by connecting two capacitors (10 and 1 nF) to the motion sensor. As shown in **Figure 2.49**, $V_{\text{capacitor}}^{10\text{nF}}$ increased to 0.6 V when an external impact was applied to the motion sensor connected with the 10 nF capacitor, and the data was stored in the RRAM cell. When normal behavior occurred, the motion sensor connected with the 1 nF capacitor induced a voltage of 0.3 V (~ 3 Hz) and 1.0 V (~ 6 Hz) at tremor state, respectively. Only high frequency signals, i.e. over 6 Hz, were able to switch the RRAM cells to LRS. I summarized the references to define operation frequency of sensor (**Table 2.2**). In this range of the frequency, the RRAM well maintained the I_{on} and I_{off} after the stretching cycle (**Figure 2.50**). By attaching this self-powered wearable electronic system to the wrist, I could readily distinguish three different types of motion (fall, walking, and tremors), and store the data into the wearable memory without complex data processing circuits.

I further demonstrated the large-scale fabrication of the self-powered monitoring system, in which the cell (integration of Ag_2S RRAM and touch sensor) matrix with 4 × 4 pixels in size of 4 mm × 4 mm was fabricated as shown in **Figure 2.51**. Touch sensor array was integrated with RRAM cell array

(**Figure 2.52**). Existing external pressure on touch sensor, it generated electrical power due to triboelectric effect. Production of AC signal was converted to DC signal at external circuit (**Figure 2.53).** Before external pressure on touch sensor, the current read from Ag_2S RRAM was ~10^{-8} A, when touch operation was applied on the cell matrix with specific path (letter "N"), the current read from RRAM laid on the path was ~10^{-3} A (**Figure 2.54 and 2.55**). Since I_{on}/I_{off} ratio of self-powered Ag_2S RRAM matrix reaches ~10^5, I could expect uniform performance of Ag_2S RRAM at even self-powered RRAM device. Recently, various type of the stretchable self-powered sensing systems for health monitoring have been reported. However, most papers related to self-powered sensing systems have mainly focused on the characteristics of self-powered sensors,[83-87] not focused on the data storage devices. In general, wearable memories manufactured on flexible and stretchable substrates have lower performances than those of conventional memories fabricated on rigid substrates because of low crystallinity (amorphous nature), large roughness, and low thermal/chemical stability of flexible/stretchable substrate.[87-89] However, wearable non-volatile memory fabricated on ultrathin polyimide substrate maintained its outstanding bipolar switching characteristics under bending and stretching cycle test conditions, which offer great potential of daily-life usable high-performance wearable electronics in a real-world setting.

Figure 2.44. Schematic illustration and photograph showing the flexible/stretchable Ag_2S-based RRAM system.

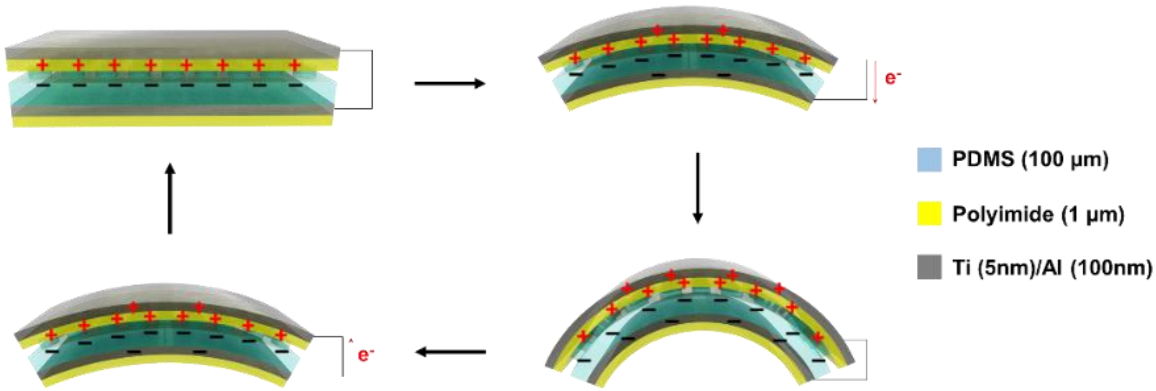

Figure 2.45. Working mechanism of triboelectric sensor. When device was bent by external force, triboelectric charges were generated by difference of triboelectric effect tendency. Negative charges and positive charges were generated on the surface of PDMS and polyimide film, respectively. The generated surface charges induce the electron flows from top electrode to bottom electrode for balance of electric charges. Through this phenomenon, I can scavenge electric power from triboelectric sensor.

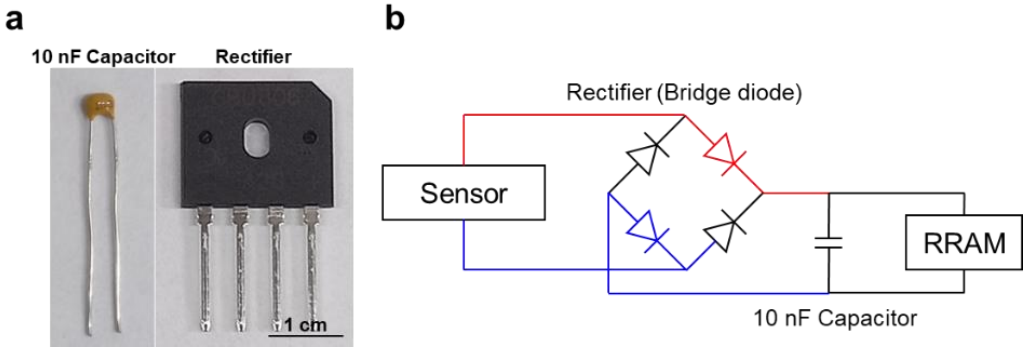

Figure 2.46. a) Photograph of 10 nF capacitor and rectifier. b) Circuit diagram of touch sensor array.

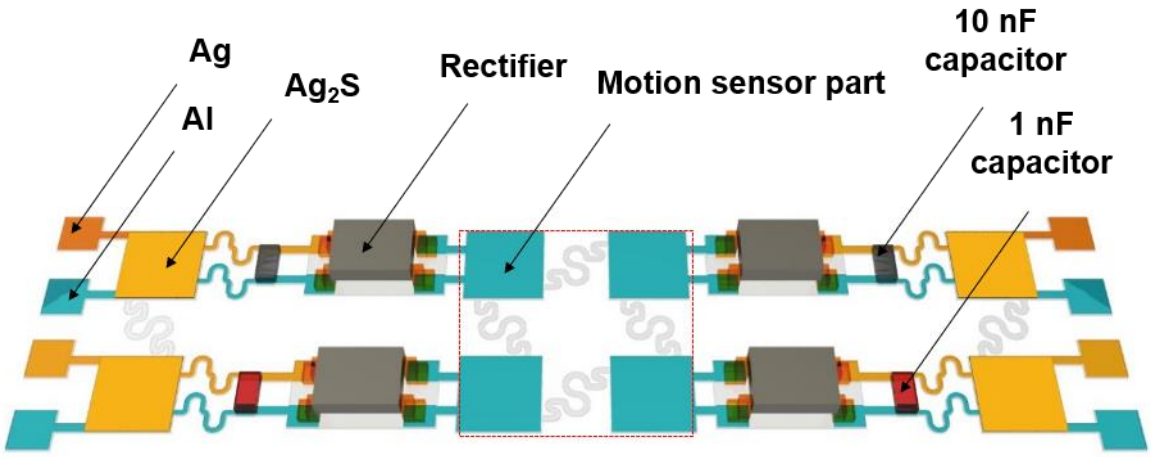

Figure 2.47. Schematic illustration showing the corresponding device composition of the panel.

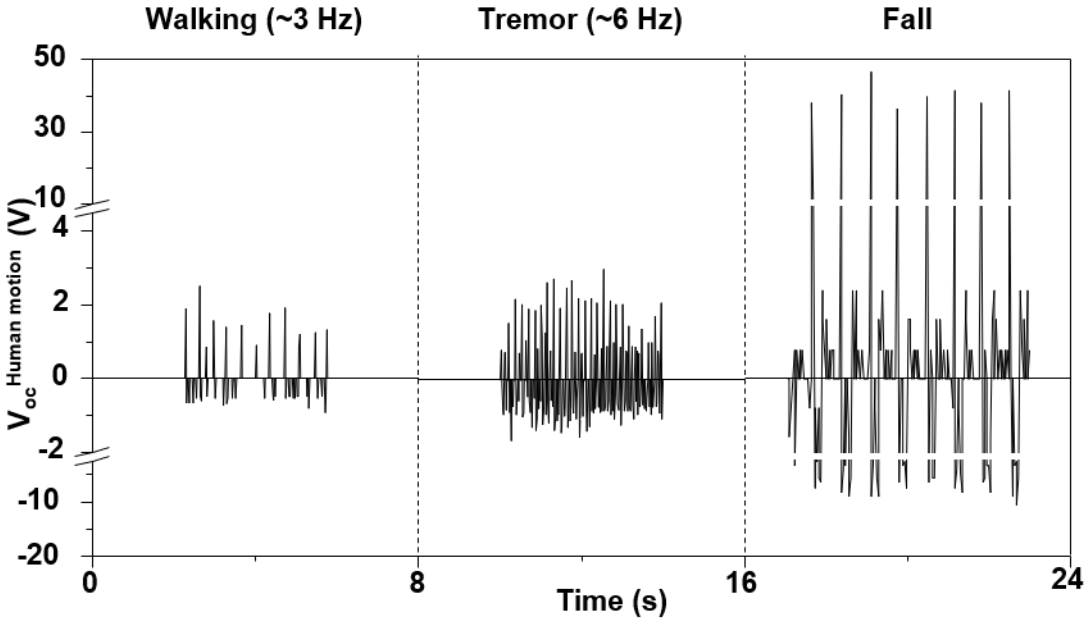

Figure 2.48. Open-circuit voltage from triboelectric sensor under three different measurement condition (walking, tremor and fall).

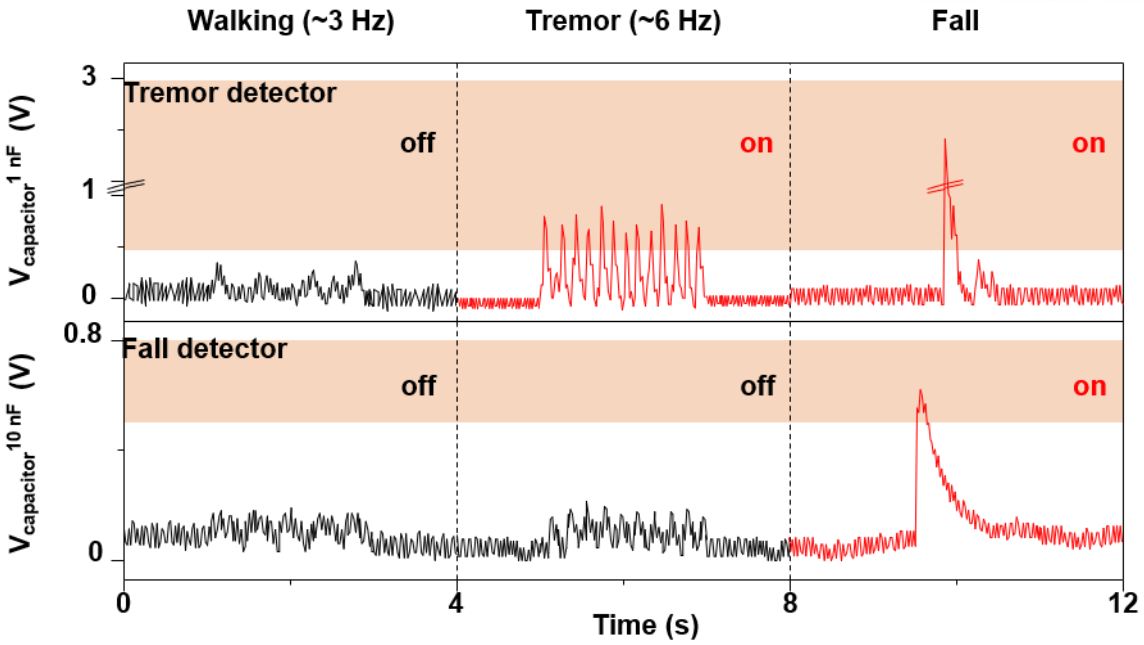

Figure 2.49. Charged voltage in capacitor (10 nF for fall, 1 nF for human motion) under three different measurement condition (walking, tremor and fall).

Table S2. The sensed frequency under walking and tremor of human motion.

Walking frequency (Hz)	Tremor frequency (Hz)	Reference
0.5 ~ 3	None	77
2 ~ 3	None	78
2 ~ 3	None	79
~ 1	None	80
None	6 ~ 12	81
None	4 ~ 6	82

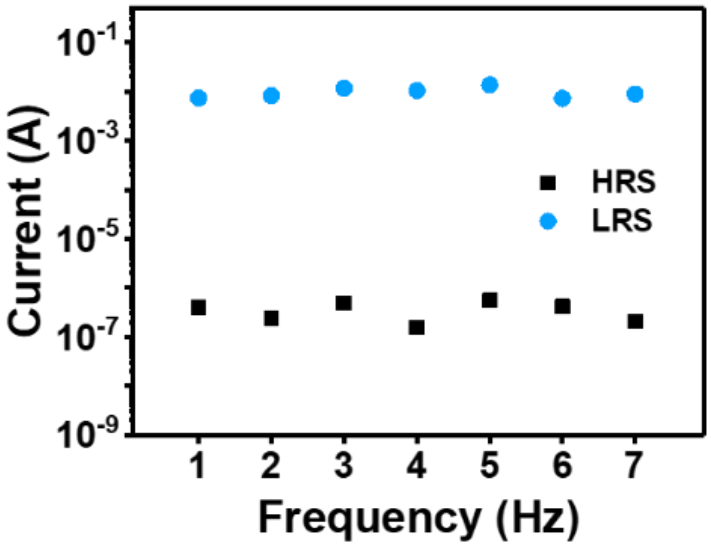

Figure 2.50. I_{on} and I_{off} of stretchable Ag_2S-based RRAM measured at different stretching frequencies.

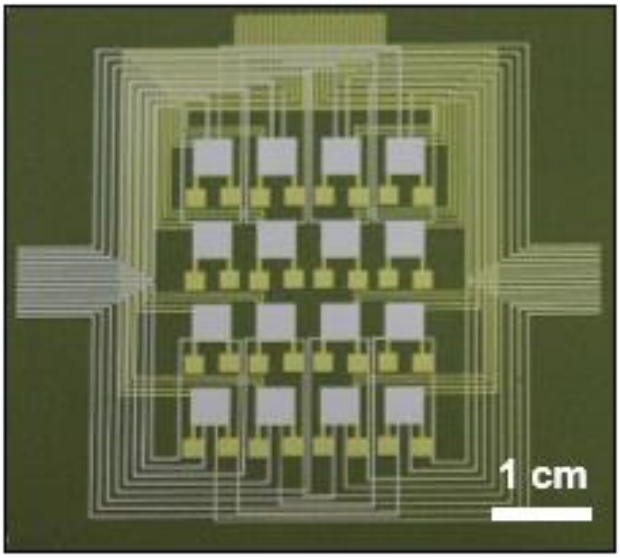

Figure 2.51. Photograph showing the self-powered Ag_2S RRAM system cell matrix with 4 × 4 pixels.

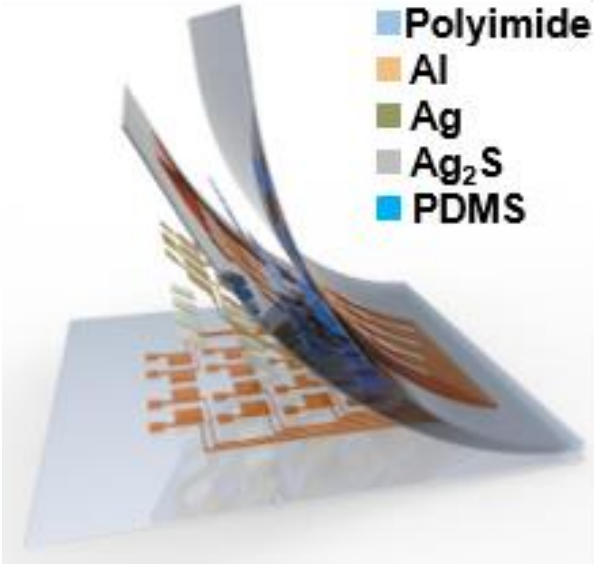

Figure 2.52. Schematic illustration showing the corresponding device composition of cell matrix.

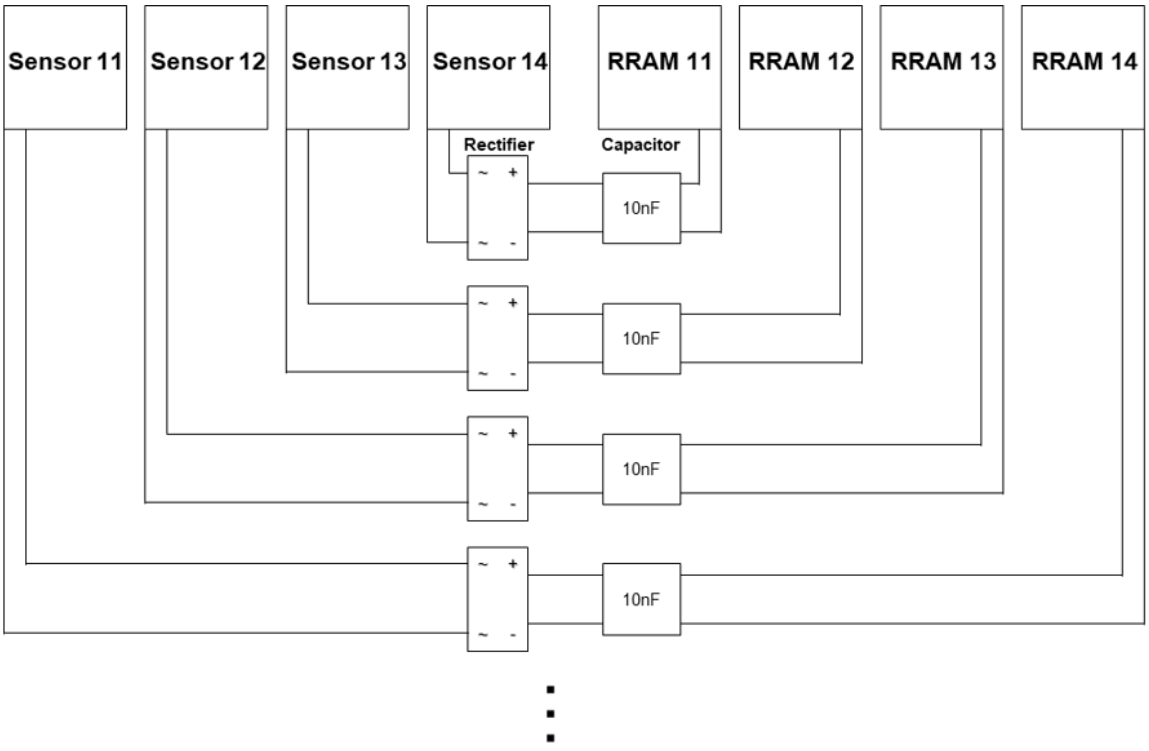

Figure 2.53. External circuit composed of rectifier and 10 nF capacitor for operating Ag_2S RRAM with touch sensor array.

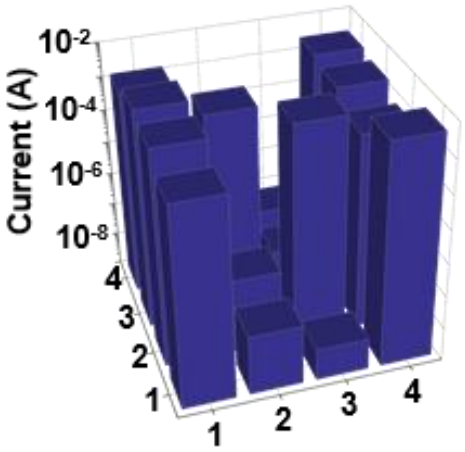

Figure 2.54. Relevant current mapping after applying mechanical pressure along path of letter "N".

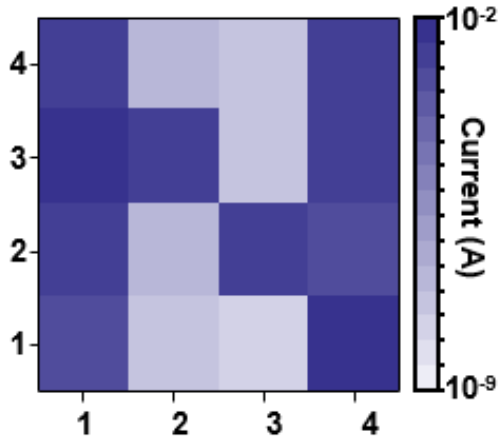

Figure 2.55. Illustration of the applying mechanical pressure paths of the letter of "N".

2.3 Conclusion

In summary, this study demonstrated the wafer-scale fabrication of stretchable Ag_2S-based devices by solution-processed synthesis of ductile semiconducting Ag_2S thin films. The most significant effect of the Ag_2S films' intrinsic ductility was shown to exhibit their stretchability up to 14.9%, enabling the fabrication of the wrinkled Ag_2S-based semiconductor memory device with the excellent mechanical stretchability of 52%. It was shown that the fabricated memory device fulfilled the favorable properties expected for standard RRAM, including an I_{on}/I_{off} ratio, operational endurance, and retention properties, as well as extraordinary durability to externally induced chemical and thermal stresses. Moreover, this stretchable memory was integrated with motion sensor to form a self-powered healthcare monitoring system, where I could readily distinguish patient's motions and store the data into the wearable memory without complex data processing circuits, validating the ubiquitous applicability of the current Ag_2S thin films. This approach has the potential for cost-effective manufacturing of high-performance, extremely durable, and stretchable semiconductor thin films, which will be easily extended to other functional electronic devices, shedding light on the stretchable electronics community.

2.4 Experimental section

2.4.1 *Materials*

Ethylenediamine (>99 %), 1,2-ethanedithiol (>98 %), silver sulfide (99.9 %), acetonitrile (anhydrous, 99.8 %), n-methyl formamide, (99 %), dimethyl sulfoxide (anhydrous, 99.9 %), poly(pyromellitic dianhydride-co-4,4′-oxydianiline), amic acid solution (80%/20% solvent ratio) were purchased from Sigma-Aldrich. Ethyl alcohol (>99.5 %), methyl alcohol (99.5 %), tetrahydrofuran (99.9 %), toluene (99.5 %), hexane (95 %), were purchased from Samchun chemical. N,N-Dimethylformamide (99 %) was purchased from Alfa Aesar.

2.4.2 *Synthesis of purified Ag_2S solution*

The initial Ag_2S solution was prepared by dissolving 0.045 g of Ag_2S powder in a alkahest solvent of 1 mL of ethylenediamine and 0.1 mL of ethanedithiol. The solution was stirred for over 3 hours at 50 °C to fully dissolve the powder and to prevent the crystallization of the co-solvent. Then, the solute was precipitated by adding 5 mL of acetonitrile to 1.1 mL of the Ag_2S solution followed by centrifugation at 7800 rpm for 5 min. The submerged solute was redispersed in 0.15 mL ethylenediamine and filtered through a 0.2 μm PTFE filter. All process was carried out in a nitrogen filled glove box.

2.4.3 *Deposition of Ag_2S thin films*

Glass and polyimide substrates were cleaned with methanol, acetone and isopropanol, followed by O_2 plasma treatment to hydrophilize the substrate. The purified Ag_2S solution was spin-coated onto substrates at 2000 rpm for 40 s. The Ag_2S thin film was dried at 85 °C for 15 min and subsequently annealed at 300 °C for 5 minutes on hot plate. The thin films were annealed with sulfur powder in a crucible. The second heat treatment was annealed at 350 °C for 30 minutes to evaporate the residual excess sulfur.

2.4.4 *Characterization of materials*

Microstructural characterization was carried out using scanning electron microscopy (Nova-NanoSEM230, FEI) operated at 10 kV and optical microscopy (BX53M, Olympus). Elemental analysis was conducted via energy dispersive X-ray spectroscopy (EDS) using Nova-NanoSEM230. The absorption spectra were acquired using a UV-Vis spectrophotometer (Shimadzu UV-2600). Thermogravimetric analysis (TGA) measurements were made using TA Instruments Q500 at a heating rate of 10 °C min-1 under a nitrogen flow rate of 100 mL min^{-1}. X-ray diffraction patterns were collected using a Rigaku D/MAX2500V/PC with a wavelength of 1.5418 Å (Cu Kα X-ray source). The I-V characteristics of the Ag_2S-based RRAM devices were obtained using a Keithley 2400. 3D surface

scanning of the stretchable RRAM devices was obtained using a Confocal laser scanning microscopy (OLS1300). Conductive atomic force microscopy (AFM) analyses were made using Veeco Instruments: Multimode V SPM, with using conductive AFM application module and Bruker scm-pic probe operating a normal atmospheric environment.

2.4.5 *The Ag_2S-based RRAM device fabrication*

An Al electrode was deposited on prepared glass and polyimide substrate. In case of the polyimide substrate, ~5 nm of Ti layer was deposited as an adhesion layer between polyimide substrate and Al layer. Then, Ag_2S thin film was spin coated onto Al electrode and subjected to annealing at 300 °C. After Ag_2S coating, a patterned silver electrode was deposited on Ag_2S thin film using patterned mask. All metal layers were deposited by thermal evaporator.

2.4.6 *Fabrication of the stretchable RRAM device*

A Si/SiO_2 wafer cut into 1 cm × 3 cm size was sonicated in 2-propanol and deionized water for 5 min each. After the wafer was dried, an oxygen plasma was conducted to hydrophilize the surface of the wafer. A polyimide solution was spin-coated at 3,000 rpm for 30 s, followed by annealing on the hot plate at 150 °C for 5 min in air, 150 °C for 5 min and 250 °C for 60 min in inert condition. Then, Ti was deposited as an adhesion layer (~5 nm) and ~70 nm of Al was deposited on titanium layer by thermal evaporator. Ag_2S thin film was spin coated on Al electrode at 2000 rpm for 40 s. To patterned the Ag_2S, a shadow mask was used. After Ag_2S coating, ~ 70 nm of Ag was deposited on Ag_2S as top electrode by thermal evaporator with patterned metal mask. Polyimide film was coated on top by spin coating process at 3000 rpm for 30 s and partially etched by oxygen plasma (150 W, 420 mTorr) for 385 s with patterned metal mask. Ag electrode was deposited once again to ~70 nm. And then, the device was peeled off by water soluble tape from wafer substrate, and transferred onto pre-stretched rubber substrate. After dropped deionized water for 60 s, water soluble tape was detached from the device and residual DI water was dried by air blowing. Pre-strained rubber substrate was released and stretchable memory device was formed (**Figure 2.56**).

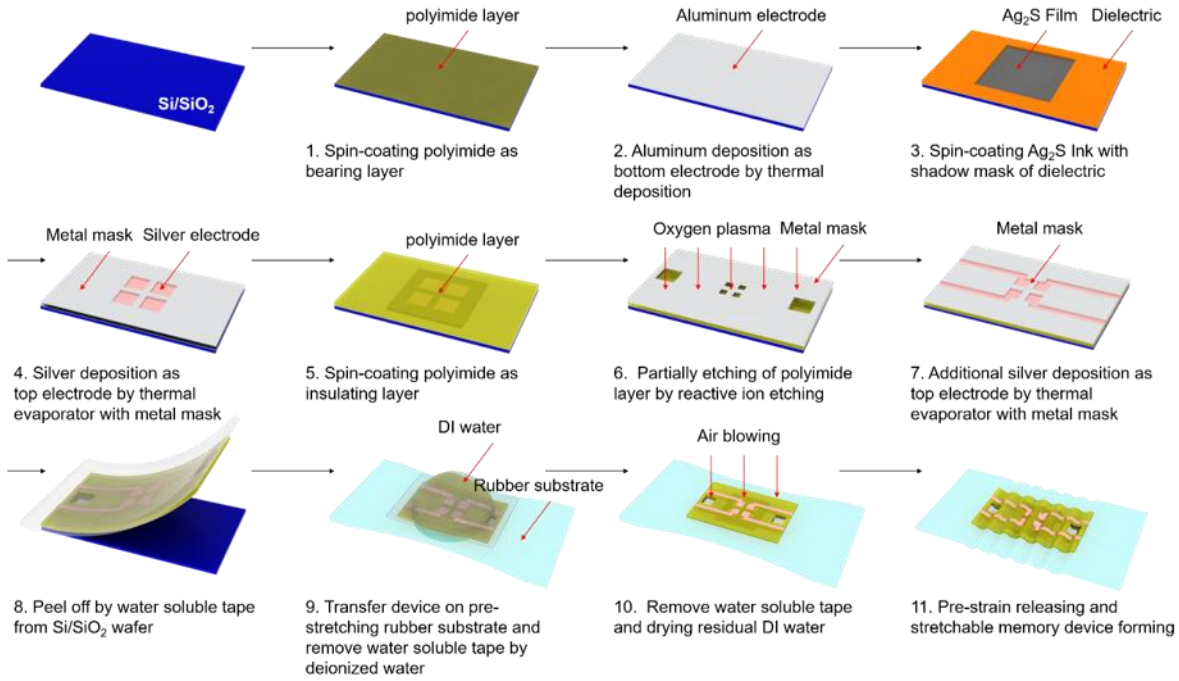

Figure 2.56. Schematic illustrations of the fabrication procedure of the stretchable Ag/Ag_2S/Al RRAM.

2.4.7 *Mechanical properties of Ag_2S thin film & FEA simulation*

Nanoindentations were conducted using Nanoindenter G200 instrument (KLA, Milpitas, CA, USA) with a three-sided pyramidal Berkovich indenter. The maximum indentation depth was 40 nm, which is about 1/10 of the sample thickness. Poisson's ratio of Ag_2S film was used as 0.35 for the analysis. For the nanoindentations, the loading rate was controlled as 0.05 and the thermal drift was maintained below 0.05 nm/s. Ten nanoindentations were performed to obtain reproducible data, and elastic modulus and hardness as a function of indentation depth were measured using continuous stiffness measurement (CSM). Uni-axial stretching test was conducted with customized uni-axial stretching tester. The strain rate was maintained for 10^{-3} s^{-1} of total length of deformable substrate. The surface of Ag_2S film was observed and recorded with visual-light microscope during stretching test. And the strain was measured with DIC (digital image correlation) process after experiments. 3D finite element analysis (FEA) simulations were conducted for simulating deformation behavior of wrinkled Ag_2S films by using a commercial software (ABAQUS, Dassult Systemes, France). The refine mesh was generated for saturated analysis results, and the element type was 8-node linear brick with full integration method (C3D8). In this analysis, the elastic modulus was set as 8.24 GPa which was measured by nanoindentations and the Poisson's ratio was set as 0.35.

2.4.8 *Fabrication of the wearable self-powered RRAM system*

A Si/SiO_2 wafer was sonicated in 2-propanol and deionized water for 5 min each. After the wafer was dried, an oxygen plasma was conducted to hydrophilize the surface of the wafer. A polyimide solution was spin-coated at 500 rpm for 30 s, followed by annealing on the hot plate at 150 °C for 5 min in air, 150 °C for 5 min and 250 °C for 30 min in inert condition. Before deposition Al electrode, photolithography was accomplished with patterned photomask. Ti was deposited as an adhesion layer (10 nm) and ~100 nm of Al was deposited on titanium layer by thermal evaporator. Ag_2S thin film was partially coated on Al electrode. After Ag_2S coating, photolithography was proceeded again and then, 200 nm of Ag was deposited on Ag_2S as top electrode by thermal evaporator. To form serpentine structure in wearable RRAM, polyimide substrate was etched by oxygen plasma (150 W, 420 mTorr) for 1000 s with photolithography pattern for encapsulation. Device was transferred on PDMS substrate using water soluble tape. And PDMS film was attached on the bottom electrode of sensor part as triboelectric layer. For top electrode of motion sensor, patterned Ti (10 nm)/Al (100 nm) electrode was deposited on the other polyimide film substrate using photolithography and etched for serpentine structure with the same condition and then transferred on PDMS (triboelectric layer) with water soluble tape. To convert triboelectric signal into DC signal, extra external circuit is necessary to operate self-powered RRAM system. For the electronic connection, each rectifier and capacitor were attached on the patterned Al line with solder paste (**Figure 2.57**).

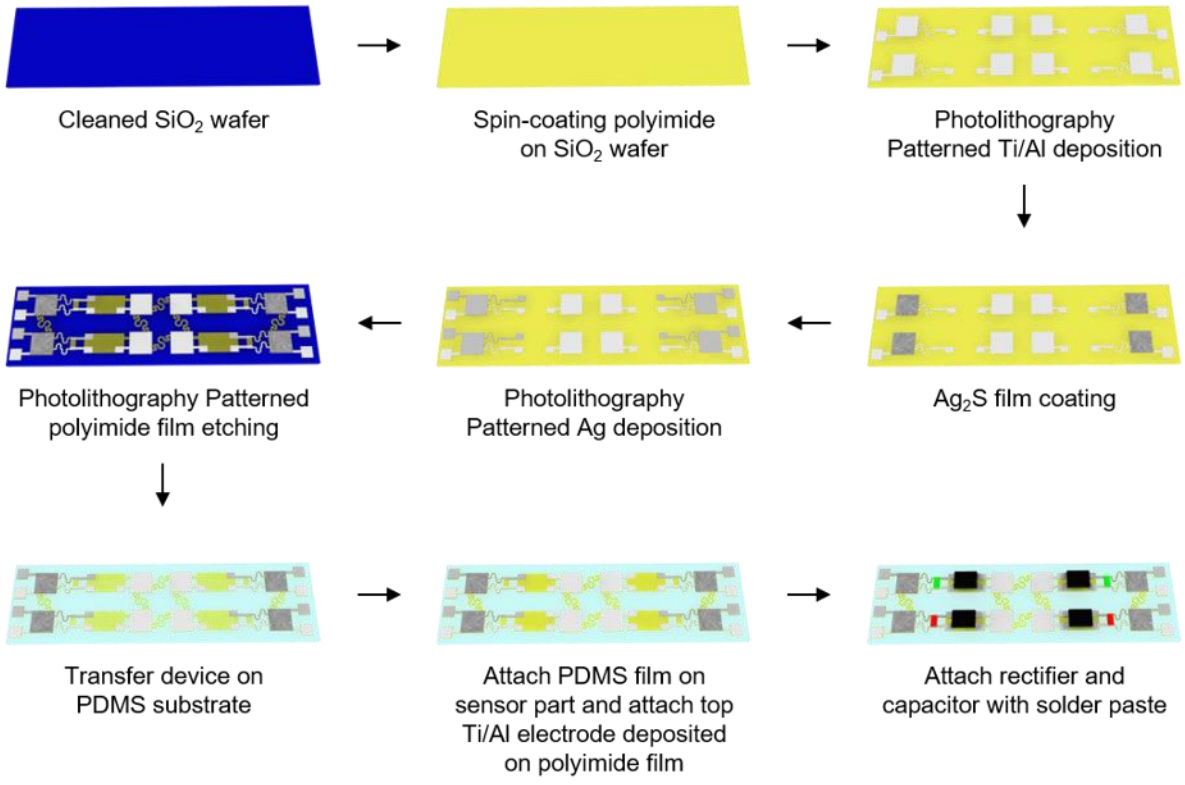

Figure 2.57. Schematic illustrations of the fabrication procedure of the stretchable self-powered RRAM.

2.4.9 *Fabrication of the self-powered RRAM matrix*

A Si/SiO_2 wafer was sonicated in 2-propanol and deionized water for 5 min each. After the wafer was dried, an oxygen plasma was conducted to hydrophilize the surface of the wafer. A polyimide solution was spin-coated at 500 rpm for 30 s, followed by annealing on the hot plate at 150 °C for 5 min in air, 150 °C for 5 min and 250 °C for 30 min in inert condition. Ti was deposited as an adhesion layer (10 nm) and ~100 nm of Al was deposited on titanium layer by thermal evaporator with patterned metal mask. Ag_2S film was coated on Al electrode, 200 nm of Ag electrode was deposited by thermal evaporator with patterned metal mask. To prevent electrical connection between touch sensor and RRAM, polyimide film was coated with 3000 rpm. 10 nm of Ti and 100 nm of Al, bottom electrode of motion sensor, was deposited with thermal evaporator. PDMS thin film was attached on bottom electrode of motion sensor as triboelectric layer. For top electrode of motion sensor, patterned Ti (10 nm)/Al (100 nm) electrode was deposited on the other polyimide film substrate using patterned metal mask (**Figure 2.58**).

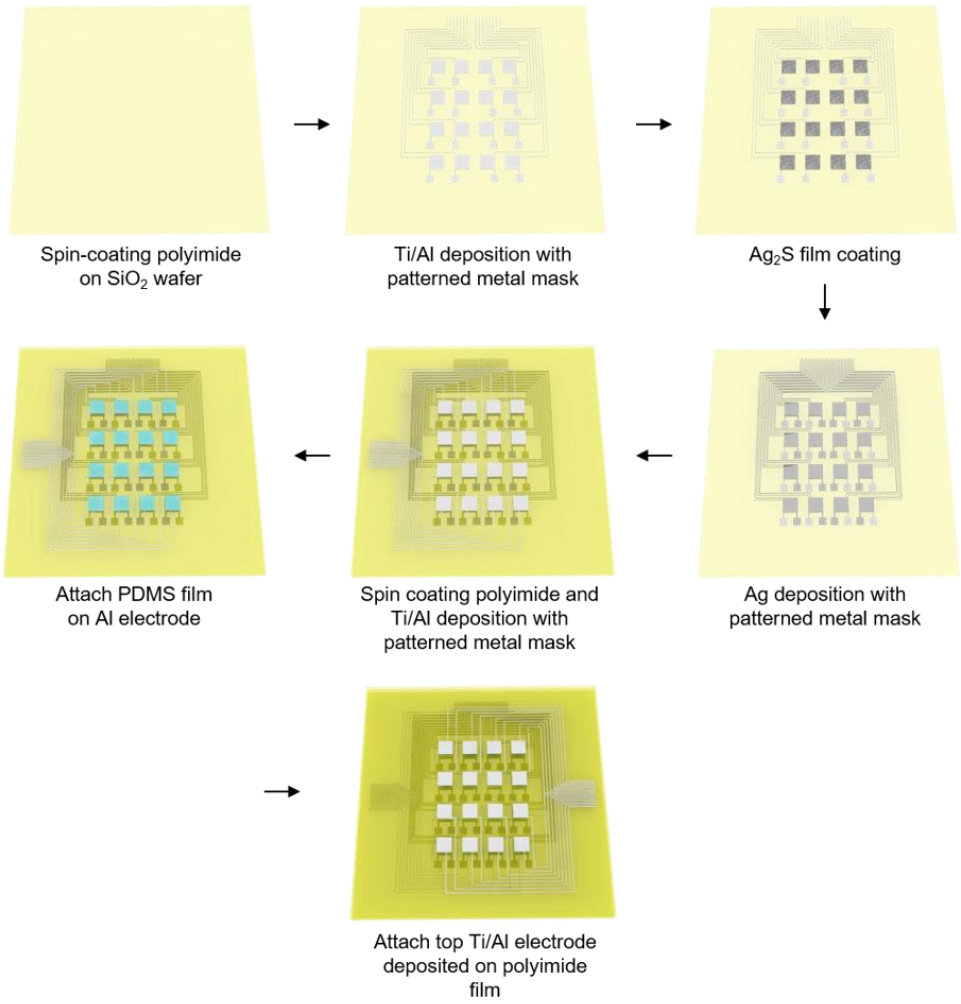

Figure 2.58. Schematic illustrations of the fabrication procedure of the large-scale RRAM matrix.

2.4.10 *The bending and stretching cycle tests*

The Ag_2S-based RRAM on polyimide substrate was attached on the home-made bending tester. The bending and stretching of the device was repeated for 1000 times. One bending cycle is to move from a flat to maximum bending or stretching state and to return to initial position. The I_{on} and I_{off} were measured after every 100 bending and stretching cycles.

2.4.11 *The chemical and thermal stability test*

For a thermal stability test, the Ag_2S-based RRAM fabricated on the glass substrate was heated on a hot plate for 10 min at the preset temperatures (50, 100, 150, 200, 250 and 300 °C). After cooled down to room temperature, I_{on} and I_{off} were measured at 0.03 V. Likewise, a chemical stability test was examined by measuring the I_{on} and I_{off} after dipping the Ag_2S-based RRAM in deionized water, ethanol, methanol, dimethylsulfoxide (DMSO), N-methlyformamide (NMF), dimethylforamide (DMF), hexane, toluene, tetrahydrofuran (THF) and phosphate buffer saline (PBS).

Reference

[1] Kim, D. H.; Lu, N.; Ma, R.; Kim, Y. S.; Kim, R. H.; Wang, S.; Wu, J.; Won, S. M.; Tao, H.; Islam, A.; Yu, K. J.; Kim, T. I.; Chowdhury, R.; Ying, M.; Xu, L.; Li, M.; Chung, H. J.; Keum, H.; McCormick, M.; Liu, P.; Zhang, Y. W.; Omenetto, F. G.; Huang, Y.; Coleman, T.; Rogers, J. A., Epidermal electronics. *Science* **2011,** *333* (6044), 838-43.

[2] Xu, J.; Wang, S.; Wang, G. N.; Zhu, C.; Luo, S.; Jin, L.; Gu, X.; Chen, S.; Feig, V. R.; To, J. W.; Rondeau-Gagne, S.; Park, J.; Schroeder, B. C.; Lu, C.; Oh, J. Y.; Wang, Y.; Kim, Y. H.; Yan, H.; Sinclair, R.; Zhou, D.; Xue, G.; M urmann, B.; Linder, C.; Cai, W.; Tok, J. B.; Chung, J. W.; Bao, Z., Highly stretch able polymer semiconductor films through the nanoconfinement effect. *Science* **2017,** *35 5* (6320), 59-64.

[3] Park, S.; Heo, S. W.; Lee, W.; Inoue, D.; Jiang, Z.; Yu, K.; Jinno, H.; Hashizume, D.; Sekino, M.; Yokota, T.; Fukuda, K.; Tajima, K.; Someya, T., Self-powered ultra-flexible electronics via nano-grating-patterned organic photovoltaics. *Nature* **2018,** *561* (7724), 516-521.

[4] Choi, C.; Choi, M. K.; Liu, S.; Kim, M. S.; Park, O. K.; Im, C.; Kim, J.; Qin, X.; Lee, G. J.; Cho, K. W.; Kim, M.; Joh, E.; Lee, J.; Son, D.; Kwon, S. H.; Jeon, N. L.; Song, Y. M.; Lu, N.; Kim, D. H., Human eye-inspired soft optoelectronic device using high-density MoS_2-graphene curved image sensor array. *Nat. Commun.* **2017,** *8* (1), 1664.

[5] Pan, L.; Wang, F.; Cheng, Y.; Leow, W. R.; Zhang, Y. W.; Wang, M.; Cai, P.; Ji, B.; Li, D.; Chen, X., A supertough electro-tendon based on spider silk composites. *Nat. Commun.* **2020,** *11* (1), 1332.

[6] Kim, Y.; Chortos, A.; Xu, W.; Liu, Y.; Oh, J. Y.; Son, D.; Kang, J.; Foudeh, A. M.; Zhu, C.; Lee, Y.; Niu, S.; Liu, J.; Pfattner, R.; Bao, Z.; Lee, T. W., A bioinspired flexible organic artificial afferent nerve. *Science* **2018,** *360* (6392), 998-1003.

[7] Choi, M. K.; Yang, J.; Kang, K.; Kim, D. C.; Choi, C.; Park, C.; Kim, S. J.; Chae, S. I.; Kim, T. H.; Kim, J. H.; Hyeon, T.; Kim, D. H., Wearable red-green-blue quantum dot light-emitting diode array using high-resolution intaglio transfer printing. *Nat. Commun.* **2015,** *6*, 7149.

[8] Liu, Y. F.; Liu, Q.; Long, J. F.; Yi, F. L.; Li, Y. Q.; Lei, X. H.; Huang, P.; Du, B.; Hu, N.; Fu, S. Y., Bioinspired Color-Changeable Organogel Tactile Sensor with Excellent Overall Performance. *ACS Appl. Mater. Interfaces* **2020,** *12* (44), 49866-49875.

[9] Liu, J.; Wang, J.; Zhang, Z.; Molina-Lopez, F.; Wang, G. N.; Schroeder, B. C.; Yan, X.; Zeng, Y.; Zhao, O.; Tran, H.; Lei, T.; Lu, Y.; Wang, Y. X.; Tok, J. B.;

Dauskardt, R.; Chung, J. W.; Yun, Y.; Bao, Z., Fully stretchable active-matrix organic light-emitting electrochemical cell array. *Nat. Commun.* **2020,** *11* (1), 3362.

[10] Yu, Z.; Niu, X.; Liu, Z.; Pei, Q., Intrinsically stretchable polymer light-emitting devices using carbon nanotube-polymer composite electrodes. *Adv. Mater.* **2011,** *23* (34), 3989-94.

[11] Sekitani, T.; Nakajima, H.; Maeda, H.; Fukushima, T.; Aida, T.; Hata, K.; Someya, T., Stretchable active-matrix organic light-emitting diode display using printable elastic conductors. *Nat. Mater.* **2009,** *8* (6), 494-9.

[12] Oh, J. Y.; Son, D.; Katsumata, T.; Lee, Y.; Kim, Y.; Lopez, J.; Wu, H. C.; Kang, J.; Park, J.; Gu, X.; Mun, J.; Wang, N. G.; Yin, Y.; Cai, W.; Yun, Y.; Tok, J. B.; Bao, Z., Stretchable self-healable semiconducting polymer film for active-matrix strain-sensing array. *Sci. Adv.* **2019,** *5* (11), eaav3097.

[13] Choi, S.; Han, S. I.; Jung, D.; Hwang, H. J.; Lim, C.; Bae, S.; Park, O. K.; Tschabrunn, C. M.; Lee, M.; Bae, S. Y.; Yu, J. W.; Ryu, J. H.; Lee, S. W.; Park, K.; Kang, P. M.; Lee, W. B.; Nezafat, R.; Hyeon, T.; Kim, D. H., Highly conductive, stretchable and biocompatible Ag-Au core-sheath nanowire composite for wearable and implantable bioelectronics. *Nat. Nanotechnol.* **2018,** *13* (11), 1048-1056.

[14] Wang, Y.; Zhu, C.; Pfattner, R.; Yan, H.; Jin, L.; Chen, S.; Molina-Lopez, F.; Lissel, F.; Liu, J.; Rabiah, N. I.; Chen, Z.; Chung, J. W.; Linder, C.; Toney, M. F.; Murmann, B.; Bao, Z., A highly stretchable, transparent, and conductive polymer. *Sci. Adv.* **2017,** *3* (3), e1602076.

[15] Wang, H.; Morozov, S. I.; Goddard, W. A.; An, Q., Light irradiation induced brittle-to-ductile and ductile-to-brittle transition in inorganic semiconductors. *Phys. Rev. B* **2019,** *99* (16).

[16] Matsunaga, K.; Hoshino, S.; Ukita, M.; Oshima, Y.; Yokoi, T.; Nakamura, A., Carrier-trapping induced reconstruction of partial-dislocation cores responsible for light-illumination controlled plasticity in an inorganic semiconductor. *Acta Mater.* **2020,** *195*, 645-653.

[17] Qian, Y.; Zhang, X.; Xie, L.; Qi, D.; Chandran, B. K.; Chen, X.; Huang, W., Stretchable Organic Semiconductor Devices. *Adv. Mater.* **2016,** *28* (42), 9243-9265.

[18] Okamoto, T.; Mitsui, C.; Yamagishi, M.; Nakahara, K.; Soeda, J.; Hirose, Y.; Miwa, K.; Sato, H.; Yamano, A.; Matsushita, T.; Uemura, T.; Takeya, J., V-shaped organic semiconductors with solution processability, high mobility, and high thermal durability. *Adv. Mater.* **2013,** *25* (44), 6392-7.

[19] Iino, H.; Usui, T.; Hanna, J., Liquid crystals for organic thin-film transistors. *Nat. Commun.* **2015,** *6*, 6828.

[20] Locklin, J.; Ling, M. M.; Sung, A.; Roberts, M. E.; Bao, Z., High-Performance Organic Semiconductors Based on Fluorene–Phenylene Oligomers with High Ionization Potentials. *Adv. Mater.* **2006,** *18* (22), 2989-2992.

[21] Kimura, Y.; Nagase, T.; Kobayashi, T.; Hamaguchi, A.; Ikeda, Y.; Shiro, T.; Takimiya, K.; Naito, H., Soluble organic semiconductor precursor with specific phase separation for high-performance printed organic transistors. *Adv. Mater.* **2015,** *27* (4), 727-32.

[22] Shi, X.; Chen, H.; Hao, F.; Liu, R.; Wang, T.; Qiu, P.; Burkhardt, U.; Grin, Y.; Chen, L., Room-temperature ductile inorganic semiconductor. *Nat. Mater.* **2018,** *17* (5), 421-426.

[23] Zhou, W. X.; Wu, D.; Xie, G.; Chen, K. Q.; Zhang, G., alpha-Ag2S: A Ductile Thermoelectric Material with High *ZT*. *ACS Omega* **2020,** *5* (11), 5796-5804.

[24] Li, G.; An, Q.; Morozov, S. I.; Duan, B.; Goddard, W. A.; Zhang, Q.; Zhai, P.; Snyder, G. J., Ductile deformation mechanism in semiconductor α-Ag_2S. *npj Comput. Mater.* **2018,** *4* (1).

[25] Liang, J.; Wang, T.; Qiu, P.; Yang, S.; Ming, C.; Chen, H.; Song, Q.; Zhao, K.; Wei, T.-R.; Ren, D.; Sun, Y.-Y.; Shi, X.; He, J.; Chen, L., Flexible thermoelectrics: from silver chalcogenides to full-inorganic devices. *Energy Environ. Sci.* **2019,** *12* (10), 2983-2990.

[26] Li, G.; An, Q.; Morozov, S. I.; Duan, B.; Goddard, W. A.; Zhang, Q.; Zhai, P.; Snyder, G. J., Ductile deformation mechanism in semiconductor α-Ag_2S. *npj Comput. Mater.* **2018,** *4* (1).

[27] Ehsan, M. A.; Khaledi, H.; Tahir, A. A.; Ming, H. N.; Wijayantha, K. G. U.; Mazhar, M., Synthesis and characterization of silver diethyldithiocarbamate cluster for the deposition of acanthite (Ag_2S) thin films for photoelectrochemical applications. *Thin Solid Films* **2013,** *536*, 124-129.

[28] Karashanova, D., Crystalline structure and phase composition of epitaxially grown Ag_2S thin films. *Solid State Ion.* **2004,** *171* (3-4), 269-275.

[29] Nozaki, H.; Onoda, M.; Yukino, K.; Kurashima, K.; Kosuda, K.; Maki, H.; Hishita, S., Epitaxial growth of Ag_2S films on MgO(001). *J. Solid State Chem.* **2004,** *177* (4-5), 1165-1172.

[30] Zahoor, F.; Azni Zulkifli, T. Z.; Khanday, F. A., Resistive Random Access Memory (RRAM): an Overview of Materials, Switching Mechanism, Performance, Multilevel Cell (mlc) Storage, Modeling, and Applications. *Nanoscale Res. Lett.* **2020,** *15* (1), 90.

[31] Pan, F.; Gao, S.; Chen, C.; Song, C.; Zeng, F., Recent progress in resistive random access memories: Materials, switching mechanisms, and performance. *Mater. Sci. R Rep.* **2014,** *83*, 1-59.

[32] Zidan, M. A.; Strachan, J. P.; Lu, W. D., The future of electronics based on memristive systems. *Nat. Electron.* **2018,** *1* (1), 22-29.

[33] Valov, I.; Waser, R.; Jameson, J. R.; Kozicki, M. N., Electrochemical metallization memories—fundamentals, applications, prospects. *Nanotechnology* **2011,** *22* (28).

[34] Waser, R.; Dittmann, R.; Staikov, G.; Szot, K., Redox-Based Resistive Switching Memories - Nanoionic Mechanisms, Prospects, and Challenges. *Adv. Mater.* **2009,** *21* (25-26), 2632-2663.

[35] Waser, R.; Aono, M., Nanoionics-based resistive switching memories. *Nat. Mater.* **2007,** *6* (11), 833-40.

[36] Morales-Masis, M.; van der Molen, S. J.; Fu, W. T.; Hesselberth, M. B.; van Ruitenbeek, J. M., Conductance switching in Ag_2S devices fabricated by in situ sulfurization. *Nanotechnology* **2009,** *20* (9), 095710.

[37] Liao, Z. M.; Hou, C.; Zhao, Q.; Wang, D. S.; Li, Y. D.; Yu, D. P., Resistive switching and metallic-filament formation in Ag_2S nanowire transistors. *Small* **2009,** *5* (21), 2377-81.

[38] Shin, J.; Kim, I.; Biju, K. P.; Jo, M.; Park, J.; Lee, J.; Jung, S.; Lee, W.; Kim, S.; Park, S.; Hwang, H., TiO2-based metal-insulator-metal selection device for bipolar resistive random access memory cross-point application. *J. Appl. Phys.* **2011,** *109* (3).

[39] Son, D.; Chae, S. I.; Kim, M.; Choi, M. K.; Yang, J.; Park, K.; Kale, V. S.; Koo, J. H.; Choi, C.; Lee, M.; Kim, J. H.; Hyeon, T.; Kim, D. H., Colloidal Synthesis of Uniform-Sized Molybdenum Disulfide Nanosheets for Wafer-Scale Flexible Nonvolatile Memory. *Adv. Mater.* **2016,** *28* (42), 9326-9332.

[40] Ji, Y.; Yang, Y.; Lee, S. K.; Ruan, G.; Kim, T. W.; Fei, H.; Lee, S. H.; Kim, D. Y.; Yoon, J.; Tour, J. M., Flexible Nanoporous WO_{3-x} Nonvolatile Memory Device. *ACS Nano* **2016,** *10* (8), 7598-603.

[41] Liu, P.-H.; Lin, C.-C.; Manekkathodi, A.; Chen, L.-J., Multilevel resistance switching of individual Cu_2S nanowires with inert electrodes. *Nano Energy* **2015,** *15*, 362-368.

[42] Jang, J.; Pan, F.; Braam, K.; Subramanian, V., Resistance switching characteristics of solid electrolyte chalcogenide Ag_2Se nanoparticles for flexible nonvolatile memory applications. *Adv. Mater.* **2012,** *24* (26), 3573-6.

[43] Cheng, C. H.; Yeh, F. S.; Chin, A., Low-power high-performance non-volatile memory on a flexible substrate with excellent endurance. *Adv. Mater.* **2011,** *23* (7), 902-5.

[44] Kim, S.; Jeong, H. Y.; Kim, S. K.; Choi, S. Y.; Lee, K. J., Flexible memristive memory array on plastic substrates. *Nano. Lett.* **2011,** *11* (12), 5438-42.

[45] Shi, Q.; Wang, J.; Aziz, I.; Lee, P. S., Stretchable and Wearable Resistive Switching Random-Access Memory. *Adv. Intell. Syst.* **2020**.

[46] Hung, C.-C.; Chiu, Y.-C.; Wu, H.-C.; Lu, C.; Bouilhac, C.; Otsuka, I.; Halila, S.; Borsali, R.; Tung, S.-H.; Chen, W.-C., Conception of Stretchable Resistive Memory Devices Based on Nanostructure-Controlled Carbohydrate-block-Polyisoprene Block Copolymers. *Adv. Funct. Mater.* **2017,** *27* (13).

[47] Gao, S.; Yi, X.; Shang, J.; Liu, G.; Li, R. W., Organic and hybrid resistive switching materials and devices. *Chem. Soc. Rev.* **2019,** *48* (6), 1531-1565.

[48] Wu, P. H.; Lin, Y. C.; Laysandra, L.; Lee, M. H.; Chiu, Y. C.; Isono, T.; Satoh, T.; Chen, W. C., Organic-Inorganic Nanocomposite Film for High-Performance Stretchable Resistive Memory Device. *Macromol. Rapid Commun.* **2020,** *41* (3), e1900542.

[49] Baek, I.-J.; Cho, W.-J., Resistive switching characteristics of solution-processed organic-inorganic blended films for flexible memory applications. *Solid-State Electron.* **2018,** *140*, 129-133.

[50] Wang, Z. Q.; Xu, H. Y.; Li, X. H.; Zhang, X. T.; Liu, Y. X.; Liu, Y. C., Flexible Resistive Switching Memory Device Based on Amorphous InGaZnO Film With Excellent Mechanical Endurance. *IEEE Electron Device Lett.* **2011,** *32* (10), 1442-1444.

[51] Jeong, H. Y.; Kim, J. Y.; Kim, J. W.; Hwang, J. O.; Kim, J. E.; Lee, J. Y.; Yoon, T. H.; Cho, B. J.; Kim, S. O.; Ruoff, R. S.; Choi, S. Y., Graphene oxide thin films for flexible nonvolatile memory applications. *Nano Lett.* **2010,** *10* (11), 4381-6.

[52] Pan, L.; Ji, Z.; Yi, X.; Zhu, X.; Chen, X.; Shang, J.; Liu, G.; Li, R.-W., Metal-Organic Framework Nanofilm for Mechanically Flexible Information Storage Applications. *Adv. Funct. Mater.* **2015,** *25* (18), 2677-2685.

[53] Webber, D. H.; Brutchey, R. L., Alkahest for V_2VI_3 chalcogenides: dissolution of nine bulk semiconductors in a diamine-dithiol solvent mixture. *J. Am. Chem. Soc.* **2013,** *135* (42), 15722-5.

[54] McCarthy, C. L.; Webber, D. H.; Schueller, E. C.; Brutchey, R. L., Solution-Phase Conversion of Bulk Metal Oxides to Metal Chalcogenides Using a Simple Thiol-Amine Solvent Mixture. *Angew. Chem. Int. Ed.* **2015,** *54* (29), 8378-81.

[55] Lin, Z.; He, Q.; Yin, A.; Xu, Y.; Wang, C.; Ding, M.; Cheng, H. C.; Papandrea, B.; Huang, Y.; Duan, X., Cosolvent approach for solution-processable electronic thin films. *ACS Nano* **2015,** *9* (4), 4398-405.

[56] Jo, S.; Park, S. H.; Shin, H.; Oh, I.; Heo, S. H.; Ban, H. W.; Jeong, H.; Kim, F.; Choo, S.; Gu, D. H.; Baek, S.; Cho, S.; Kim, J. S.; Kim, B.-S.; Lee, J. E.; Song, S.; Yoo, J.-W.; Song, J. Y.; Son, J. S., Soluble Telluride-Based Molecular Precursor for Solution-Processed High-Performance Thermoelectrics. *ACS Appl. Energy Mater.* **2019,** *2* (7), 4582-4589.

[57] Heo, S. H.; Jo, S.; Kim, H. S.; Choi, G.; Song, J. Y.; Kang, J. Y.; Park, N. J.; Ban, H. W.; Kim, F.; Jeong, H.; Jung, J.; Jang, J.; Lee, W. B.; Shin, H.; Son, J. S., Composition change-driven texturing and doping in solution-processed SnSe thermoelectric thin films. *Nat. Commun.* **2019,** *10* (1), 864.

[58] Jang, D.; Greer, J. R., Transition from a strong-yet-brittle to a stronger-and-ductile state by size reduction of metallic glasses. *Nat. Mater.* **2010,** *9* (3), 215-9.

[59] Hwang, B.; An, Y.; Lee, H.; Lee, E.; Becker, S.; Kim, Y. H.; Kim, H., Highly Flexible and Transparent Ag Nanowire Electrode Encapsulated with Ultra-Thin Al_2O_3: Thermal, Ambient, and Mechanical Stabilities. *Sci. Rep.* **2017,** *7*, 41336.

[60] Li, P.; Ma, J.; Xu, H.; Xue, X.; Liu, Y., Highly stable copper wire/alumina/polyimide composite films for stretchable and transparent heaters. *J. Mater. Chem. C* **2016,** *4* (16), 3581-3591.

[61] Dennler, G.; Lungenschmied, C.; Neugebauer, H.; Sariciftci, N. S.; Latrèche, M.; Czeremuszkin, G.; Wertheimer, M. R., A new encapsulation solution for flexible organic solar cells. *Thin Solid Films* **2006,** *511-512*, 349-353.

[62] Park, J.; Yoon, H. R.; Khan, M. A.; Cho, S.; Sung, M. M., Selective Infiltration in Polymer Hybrid Thin Films as a Gas-Encapsulation Layer for Stretchable Electronics. *ACS Appl. Mater. Interfaces* **2020,** *12* (7), 8817-8825.

[63] Shang, J.; Xue, W.; Ji, Z.; Liu, G.; Niu, X.; Yi, X.; Pan, L.; Zhan, Q.; Xu, X. H.; Li, R. W., Highly flexible resistive switching memory based on amorphous-nanocrystalline hafnium oxide films. *Nanoscale* **2017,** *9* (21), 7037-7046.

[64] Khurana, G.; Misra, P.; Kumar, N.; Katiyar, R. S., Tunable Power Switching in Nonvolatile Flexible Memory Devices Based on Graphene Oxide Embedded with ZnO Nanorods. *J. Phys. Chem. C* **2014,** *118* (37), 21357-21364.

[65] Gan, K. J.; Liu, P. T.; Chien, T. C.; Ruan, D. B.; Sze, S. M., Highly durable and flexible gallium-based oxide conductive-bridging random access memory. *Sci. Rep.* **2019,** *9* (1), 14141.

[66] Kim, S.; Jeong, H. Y.; Kim, S. K.; Choi, S. Y.; Lee, K. J., Flexible memristive memory array on plastic substrates. *Nano Lett.* **2011,** *11* (12), 5438-42.

[67] Ji, Y.; Yang, Y.; Lee, S. K.; Ruan, G.; Kim, T. W.; Fei, H.; Lee, S. H.; Kim, D. Y.; Yoon, J.; Tour, J. M., Flexible Nanoporous WO_{3-x} Nonvolatile Memory Device. *ACS Nano* **2016,** *10* (8), 7598-603.

[68] Wang, Z. Q.; Xu, H. Y.; Li, X. H.; Zhang, X. T.; Liu, Y. X.; Liu, Y. C., Flexible Resistive Switching Memory Device Based on Amorphous InGaZnO Film With Excellent Mechanical Endurance. *IEEE Electron Device Lett.* **2011,** *32* (10), 1442-1444.

[69] Jeong, H. Y.; Kim, J. Y.; Kim, J. W.; Hwang, J. O.; Kim, J. E.; Lee, J. Y.; Yoon, T. H.; Cho, B. J.; Kim, S. O.; Ruoff, R. S.; Choi, S. Y., Graphene oxide thin films for flexible nonvolatile memory applications. *Nano Lett.* **2010,** *10* (11), 4381-6.

[70] Cheng, C. H.; Yeh, F. S.; Chin, A., Low-power high-performance non-volatile memory on a flexible substrate with excellent endurance. *Adv. Mater.* **2011,** *23* (7), 902-5.

[71] Jang, J.; Pan, F.; Braam, K.; Subramanian, V., Resistance switching characteristics of solid electrolyte chalcogenide Ag_2Se nanoparticles for flexible nonvolatile memory applications. *Adv. Mater.* **2012,** *24* (26), 3573-6.

[72] Pan, L.; Ji, Z.; Yi, X.; Zhu, X.; Chen, X.; Shang, J.; Liu, G.; Li, R.-W., Metal-Organic Framework Nanofilm for Mechanically Flexible Information Storage Applications. *Adv. Funct. Mater.* **2015,** *25* (18), 2677-2685.

[73] Guan, X.; Hu, W.; Haque, M. A.; Wei, N.; Liu, Z.; Chen, A.; Wu, T., Light-Responsive Ion-Redistribution-Induced Resistive Switching in Hybrid Perovskite Schottky Junctions. *Adv. Funct. Mater.* **2018,** *28* (3).Adv. Funct. Mater. 2017, 28, 1704665.

[74] Yi, X.; Yu, Z.; Niu, X.; Shang, J.; Mao, G.; Yin, T.; Yang, H.; Xue, W.; Dhanapal, P.; Qu, S.; Liu, G.; Li, R.-W., Intrinsically Stretchable Resistive Switching Memory Enabled by Combining a Liquid Metal-Based Soft Electrode and a Metal-Organic Framework Insulator. *Adv. Electron. Mater.* **2019,** *5* (2).Adv. Eletron. Mater. 2019, 5, 1800655.

[75] Shang, J.; Xue, W.; Ji, Z.; Liu, G.; Niu, X.; Yi, X.; Pan, L.; Zhan, Q.; Xu, X. H.; Li, R. W., Highly flexible resistive switching memory based on amorphous-nanocrystalline hafnium oxide films. *Nanoscale* **2017,** *9* (21), 7037-7046.

[76] Liu, Y.; Liu, Z.; Zhu, B.; Yu, J.; He, K.; Leow, W. R.; Wang, M.; Chandran, B. K.; Qi, D.; Wang, H.; Chen, G.; Xu, C.; Chen, X., Stretchable Motion Memory Devices Based on Mechanical Hybrid Materials. *Adv. Mater.* **2017,** *29* (34).

[77] Zou, Y.; Raveendran, V.; Chen, J., Wearable triboelectric nanogenerators for biomechanical energy harvesting. *Nano Energy* **2020,**

[78] Lee, S.; Ko, W.; Oh, Y.; Lee, J.; Baek, G.; Lee, Y.; Sohn, J.; Cha, S.; Kim, J.; Park, J.; Hong, J., Triboelectric energy harvester based on wearable textile platforms employing various surface morphologies. *Nano Energy* **2015,** *12*, 410-418.

[79] Choi, A. Y.; Lee, C. J.; Park, J.; Kim, D.; Kim, Y. T., Corrugated Textile based Triboelectric Generator for Wearable Energy Harvesting. *Sci. Rep.* **2017,** *7*, 45583.

[80] Jin, L.; Xiao, X.; Deng, W.; Nashalian, A.; He, D.; Raveendran, V.; Yan, C.; Su, H.; Chu, X.; Yang, T.; Li, W.; Yang, W.; Chen, J., Manipulating Relative Permittivity for High-Performance Wearable Triboelectric Nanogenerators. *Nano Lett.* **2020,** *20* (9), 6404-6411.

[81] Shi, W. Y.; Chiao, J. C., Contactless hand tremor detector based on an inductive sensor. *Analog Integr. Circuits and Signal Process.* **2017,** *94* (3), 395-403.

[82] Yang, J.-L.; Chang, R.-S.; Chen, F.-P.; Chern, C.-M.; Chiu, J.-H., Detection of hand tremor in patients with Parkinson's disease using a non-invasive laser line triangulation measurement method. *Measurement* **2016,** *79*, 20-28.

[83] Sun, R.; Carreira, S. C.; Chen, Y.; Xiang, C.; Xu, L.; Zhang, B.; Chen, M.; Farrow, I.; Scarpa, F.; Rossiter, J., Stretchable Piezoelectric Sensing Systems for Self-Powered and Wireless Health Monitoring. *Adv. Mater. Tech.* **2019,** *4* (5).

[84] Wu, C.; Kim, T. W.; Park, J. H.; Koo, B.; Sung, S.; Shao, J.; Zhang, C.; Wang, Z. L., Self-Powered Tactile Sensor with Learning and Memory. *ACS Nano* **2020,** *14* (2), 1390-1398.

[85] Liu, R.; Kuang, X.; Deng, J.; Wang, Y. C.; Wang, A. C.; Ding, W.; Lai, Y. C.; Chen, J.; Wang, P.; Lin, Z.; Qi, H. J.; Sun, B.; Wang, Z. L., Shape Memory Polymers for Body Motion Energy Harvesting and Self-Powered Mechanosensing. *Adv. Mater.* **2018,** *30* (8).

[86] Lin, L.; Hu, Y.; Xu, C.; Zhang, Y.; Zhang, R.; Wen, X.; Lin Wang, Z., Transparent flexible nanogenerator as self-powered sensor for transportation monitoring. *Nano Energy* **2013,** *2* (1), 75-81.

[87] Lee, Y.; Oh, J. Y.; Xu, W.; Kim, O.; Kim, T. R.; Kang, J.; Kim, Y.; Son, D.; Tok, J. B.; Park, M. J.; Bao, Z.; Lee, T. W., Stretchable organic optoelectronic sensorimotor synapse. *Sci. Adv.* **2018,** *4* (11), eaat7387.

[88] Sun, Y.; Zheng, X.; Yan, X.; Liao, Q.; Liu, S.; Zhang, G.; Li, Y.; Zhang, Y., Bioinspired Tribotronic Resistive Switching Memory for Self-Powered Memorizing Mechanical Stimuli. *ACS Appl. Mater. Interfaces.* **2017,** *9* (50), 43822-43829.

[89] Lee, T. H.; Hwang, H. G.; Jang, S.; Wang, G.; Han, S.; Kim, D. H.; Kang, C. Y.; Nahm, S., Low-Temperature-Grown $KNbO_3$ Thin Films and Their Application to Piezoelectric Nanogenerators and Self-Powered ReRAM Device. *ACS Appl. Mater. Interfaces.* **2017,** *9* (49), 43220-43229.

Acknowledgement

2018 년 5 월, 떨리는 마음으로 랩에 첫 출근 했을 때가 기억에 생생한데 벌써 졸업을 한다는게 아직도 실감이 나지를 않습니다. 많은 분들의 도움으로 3 년 동안 정말 많은 것을 배우면서 성장한 것 같아 뿌듯합니다. 짧지만 길었던 연구실 생활은 앞으로 살아가는데 있어서 큰 도움이 될 것 같습니다.

우선, 제가 진심으로 존경하는 손재성 교수님께 깊은 감사의 말씀을 전하고 싶습니다. 좋은 연구를 할 수 있는 기회를 주시고, 부족했던 부분을 채울 수 있도록 도와주셨기에 학위기간 동안 아주 큰 상을 받을 수 있었던 것 같습니다. 연구 뿐만 아니라 앞으로 살아감에 있어서 진심어린 조언과 격려의 말씀은 평생 잊지 않고 마음속에 새기겠습니다. 항상 감사한 마음을 가지며 열심히 노력하며 살아가겠습니다.

귀중한 시간 내주시어 저의 학위 논문 심사를 맡아주신 최문기 교수님, 김주영 교수님께 다시한번 감사의 인사를 전합니다. 디펜스 때 주신 귀중한 조언과, 분에 넘치는 칭찬과 격려의 말씀 주셔서 진심으로 감사합니다. 훌륭하신 교수님들의 큰 도움으로 더 멋진 연구를 마무리 할 수 있었던 것 같습니다. 멋진 논문을 쓰는데 큰 도움을 주신 양우정 연구원님, 김시훈 박사님, 황경석 연구원님께도 진심으로 감사의 말씀 드립니다.

NSE 실험실 구성원 들에게도 감사의 인사를 전합니다. 우선 승기오빠께 진심으로 감사의 말씀을 전하고 싶습니다. 처음부터 하나하나 잘 알려주시고 가르쳐주신 덕분에 멋진 연구를 잘 마무리 할 수 있었던 것 같습니다. 형우오빠, 항상 친절하게 뭐든 알려주시고 도와주시는 다휘오빠, XRD 담당 또 다시 맡게 된 추맨 승준이오빠, 같은 팀에서 많은 도움 주신 허선생님, 겉은 차갑지만 마음은 따뜻한 우용이오빠, 키크고 귀도큰 수리수리 정수리오빠, 생일똑같은 친구 양양, 동기 윤캠이 오빠, 같은 팀 정민이언니, 건국이에게 감사의 인사와 응원을 보냅니다. NSE 에 와서 적응 잘 할 수 있게 도와주시고, 항상 무슨일이던 잘 도와주신 성헌이 오빠께 감사의 말씀 드립니다. 앞으로 멋진 앞날이 펼쳐지길 바랍니다. 랩에 처음 온날부터 잘 챙겨주신 민주언니! 하시는 연구 다 잘 되길

진심으로 응원합니다. 앞으로도 오래오래 봐요~! 옆에서 응원해주시고 큰 힘이 되어주신 대한미국인 프레드릭 킴, 민석이 오빠에게도 진심으로 감사합니다.

마지막으로 사랑하는 우리 가족에게 감사의 말을 전하고 싶습니다. 하고 싶은거 다 할 수 있도록 믿어주시고 든든하게 지원해 주신 엄마, 아빠 진심으로 감사하고 사랑합니다.♡ 멋지고 씩씩한 내동생 정운이, 귀여운 고양이 방울이도 사랑합니다. 할머니, 큰삼촌, 큰숙모, 작은삼촌, 작은숙모, 사촌동생 준석, 예원, 효석, 연주에게도 감사와 사랑의 말씀을 전합니다. 앞으로는 받은 사랑 많이 나누며 열심히 살아가겠습니다.